Strongly non-linear magnetization dynamics in nano-structures

Perturbations, multi-mode generation, and topological droplets

Strongly non-linear magnetization dynamics in nano-structures

Perturbations, multi-mode generation, and topological droplets

Ezio Iacocca

UNIVERSITY OF GOTHENBURG

Doctoral Dissertation in Physics
Department of Physics
University of Gothenburg
June 5^{th}, 2014

Printed by Ale Tryckteam, Gothenburg 2014
ISBN: 978-91-628-8981-4
Internet-id: http://hdl.handle.net/2077/35260

Abstract

Spin torque oscillators (STOs) are magnetic nano-devices in which strongly non-linear magnetodynamic phenomena can be excited by current. In this thesis, we study some of these phenomena by means of micromagnetic simulations, analytical calculations, and electrical characterization. Three main subjects are discussed:

1. **External perturbations**, which can induce synchronization and modulation. In the former case, STOs are shown to exhibit an under-damped or non-Adlerian behavior, defining a minimum synchronization time. For the latter, slow external sources can induce the so-called non-linear frequency and amplitude modulation, from which the modulation bandwidth is defined. Both perturbations can be combined for the technologically relevant case of synchronized and modulated STOs. It is shown that regimes of resonant and non-resonant unlocking exist.

2. **Multi-mode generation** of STOs is described by a novel analytical framework. In particular, the generation linewidth is calculated, and it is shown to be intrinsically related to the coupling between multiple modes. Mode coexistence is found to be analytically possible and, further, observed experimentally and numerically. Electrical characterization of in-house fabricated devices confirms the analytical predictions and suggests the possibility of fine-tuning and controlling spin wave propagation at the nanoscale.

3. **Topological droplets** are numerically shown to exist when the STOs are patterned into nanowires. The following droplet modes have been found: a non-topological edge mode that is attracted by the physical boundaries and increases its footprint to satisfy the damping / spin torque balance, and a topological (chiral) quasi-one-dimensional droplet that can be considered as the dynamical counterpart of breathing soliton-soliton pairs.

Contents

List of Figures

List of Symbols and Acronyms

Symbol	Description	Units
$\mathbf{1}$	Identity matrix	
$\delta(t)$	Dirac delta function	
$\delta_K(x)$	Kronecker delta function	
δ_o	Functional operator	
$\mathcal{F}_s$	Series feedback function	rad/s
$\mathcal{H}$	Hamiltonian	J
$\mathcal{H}_{ex}$	Heisenberg exchange Hamiltonian	J
$\mathcal{H}_Z$	Zeeman effective Hamiltonian	J
$\mathcal{J}$	Exchange constant	J
$\mathcal{K}$	Autocorrelation function	
$\mathcal{M}$	Magnetization operator	
$\mathcal{N}$	Skyrmion number	
∇	Vector differential operator	
∇^2	Laplace operator	
∂	Partial derivative	
$\boldsymbol{\alpha_D}$	Dirac's spin 4×4 matrix	
α_G	Gilbert damping coefficient	
β	Phase delay	deg
$\boldsymbol{\beta_D}$	Dirac's particle 4×4 matrix	
β_n	Harmonic-dependent modulation index	
γ_G	Gaussian linewidth component	$1/s^2$
γ_L	Lorentzian linewidth component	1/s
γ_o	Free / fixed layer relative angle	deg
Γ_+	Positive damping term	rad/s
Γ_-	Negative damping term	rad/s
Γ_G	Gilbert damping term	rad/s
Γ_p	Total restoration rate	rad/s
Γ_τ	Phase-modified restoration rate	rad/s
Δ_B	Bloch wall width	m
Δ_N	Néel wall width	m
$\Delta\psi$	Phase deviation	deg
$\Delta\omega$	Frequency mismatch	rad/s
$\Delta\omega_o$	Phase-locking bandwidth	rad/s
$\Delta\omega_l$	Linear linewidth	rad/s

Symbol	Description	Units
ΔE	Energy barrier	J
Δf	Peak frequency deviation	Hz
Δp	Power difference	
δp	Power fluctuation	
ϵ	STT asymmetry factor	
$\epsilon_{x',y'}$	Totally antisymmetric tensor	
Θ	Droplet profile	
θ	Modal energy distribution	rad
θ_c	Critical angle	rad
θ_F	Field angle	deg
θ_L	Field for localization	deg
θ_{NC}	Ellipse tilt	deg
$\langle\theta_o\rangle$	Average modal energy	rad
θ_S	Polar angle	rad
Λ	Spin-diffusion length	m
λ	Spin torque asymmetry	
λ_c	Characteristic exponent	rad/s
λ_{ex}	Exchange length	m
λ_P	Mode-hopping rate	Hz
μ_ϕ	Electro-chemical potential	J
$\mu_{\uparrow,\downarrow}$	Spin-dependent potential	J
μ_{inj}	Injection locking strength	
μ_M	Magnetic moment	J/T
μ_m	Modulation strength	
μ'_m	Maximum modulation strength	
ν	Dimensionless nonlinearity coefficient	
ξ	Supercriticality parameter	
ξ_{so}	Spin-orbit coupling	J
ρ_C	Radius of a unit cylinder	
ρ_S	Radius of a unit sphere	
$\sigma(I)$	Minimum sustaining current	A
σ	Conductivity	S/m
σ_o	Spin torque coefficient	A/m
$\boldsymbol{\sigma}$	Pauli matrices	
τ	Torque in CRMT	J/m^2
τ_l	Time difference	s
τ_s	Minimum synchronization time	s
ϕ	STO instantaneous phase	rad
ϕ_c	Coupling phase	rad
ϕ_S	Azimuthal angle	rad
ϕ_E	Scalar potential	V
ϕ_i	Oscillator phase	rad
$\lvert\Psi\rangle$	Quantum mechanical wavefunction	
ψ	Phase difference	rad
Ω	Ringing frequency	rad/s
Ω_Σ	Average frequency of two STOs	rad/s
ω	STO generation frequency	rad/s

Symbol	Description	Units
ω_e	External frequency	rad/s
ω_M	Magnetization frequency	rad/s
ω_{max}	Resonant frequency	rad/s
ω_o	Ferromagnetic resonance frequency	rad/s
$\boldsymbol{A}$	Vector potential	N/A
A	Exchange stiffness	J/m
A_n	n-th harmonic Fourier coefficient	
a_s	Lattice constant	m
$\vec{B}$	Magnetic flux	T
B_n	n-th harmonic Fourier coefficient	
C	Capacitance	F
c	Complex amplitude	
c_t	Total amplitude	
D_1	Demagnetizing factor	
D_2	Demagnetizing factor	
D_x	Demagnetizing factor	
D_y	Demagnetizing factor	
D_z	Demagnetizing factor	
d	Diameter	m
d_m	Ellipse minor axis	m
E	Energy	J
$\vec{E}$	Electric field	V/m
E_F	Fermi energy	J
F	Coupling factor	rad/s
f	Normalized injection power	rad/s
$\tilde{f}$	Thermal fluctuations	rad/s
f_{ring}	Power for non-Adlerian dynamics	
f_s	Carrier frequency shift	Hz
g	Landé g-factor	
$H_{\parallel}$	In-plane field component	A/m
$\vec{H}$	Magnetic field	A/m
$\vec{H}_a$	Applied external field	A/m
$\vec{H}_d$	Demagnetizing field	A/m
$\vec{H}_{\text{eff}}$	Effective magnetic field	A/m
$\vec{H}_{ex}$	Exchange field	A/m
$\vec{H}_K$	Anisotropy field	A/m
H_R	Relative normalized field	
$\vec{h}$	Normalized field	
$\vec{h}_T(t)$	Time-dependent thermal field	A/m
I	Current	A
I_{dc}	dc bias current	A
$\vec{I}_s$	Spin current in CRMT	J
I_{th}	Threshold current	A
$\vec{J}_s$	Spin current density	J/m^2
$\vec{j}$	Current density	A/m^2

Symbol	Description	Units
K	Coupling strength	rad/s
$K_1 - K_6$	Coefficients	rad/s
K_U	Magnetic anisotropy	J/m^3
$\boldsymbol{k}$	Wave vector	1/m
L	Inductance	H
m	Particle's mass	Kg
$\hat{m}$	Normalized magnetization	
$\vec{M}$	Magnetization vector	A/m
M_s	Saturation magnetization	A/m
N	Nonlinearity factor	rad/s
N_h	Number of Fourier harmonics	
N_o	Number of oscillators in an ensemble	
$\hat{n}$	Normal vector	
$\boldsymbol{P}$	4-component wave in CRMT	J
P	Spin polarization	
$\bar{P}$	General STT term	
P_R	Relative normalized polarizer	
$\vec{p}$	Momentum vector	mKg/s
$\hat{p}$	Normalized magnetization of polarizer	
p_o	Free-running normalized power	
Q	Non-linear damping factor	rad/s
$\bar{Q}$	General damping factor	
R	Resistance	Ω
R_0	Parallel resistance	Ω
R_π	Antiparallel resistance	Ω
R_c	Nanocontact radius	m
$\vec{r}$	Radius	m
$\hat{S}$	Scattering matrix	
s	Determinant	
T	Temperature	K
t	Time	s
T_C	Curie temperature	K
V_s	Unit volume	m^3
X_n	Complex variable	

Constants	Description	Value and Unit
γ	Gyromagnetic ratio	28 GHz/T
μ_o	Vacuum permeability	$4\pi \times 10^{-7}$ N/A^2
μ_B	Bohr's magneton	9.27×10^{-24} J/T
c_l	Speed of light	3×10^8 m/s
e	Electron's charge	-1.6×10^{-19} C
$\hbar$	Planck's constant	6.626×10^{-34} Js
k_B	Boltzmann constant	$1.3806488 \times 10^{-23}$ J/K
		8.6173324×10^{-5} eV/K
$\mathcal{R}_{Sh}$	Sharvin resistance	0.5 fΩ·m^2

Acronym	Description
μBLS	Micro-focused Brillouin Light Scattering
ac	Alternating Current
AM	Amplitude Modulation
AMR	Anisotropic Magnetoresistance
CPP	Current Perpendicular to Plane
dc	Direct Current
DOS	Density Of States
CRMT	Continuous Random Matrix Theory
GMR	Giant Magnetoresistance
GPU	Graphic Processing Unit
FD	Finite Difference
FE	Finite Elements
FFT	Fast Fourier Transform
FMg	Ferromagnet
FM	Frequency Modulation
FMR	Ferromagnetic Resonance
LL	Landau-Lifshitz equation
LLG	Landau-Lifshitz-Gilbert equation
LLGS	Landau-Lifshitz-Gilbert-Slonczewski equation
MR	Magnetoresistance
MTJ	Magnetic Tunnel Junction
NC	Nanocontact
NC-STO	Nanocontact Spin Torque Oscillator
NFAM	Non-linear Frequency and Amplitude Modulation
NM	Non-Magnet
ODE	Ordinary Differential Equation
OP	Operating Point
PSD	Power Spectral Density
RF	Radio Frequency
RHS	Right-Hand Side
RKKY	Ruderman-Kittel-Kasuya-Yosida interaction
RLC	Resistance-Inductor-Capacitor circuit
rms	Root Mean Square
SA	Spectrum Analyzer
SDE	Stochastic Differential Equation
SEM	Scanning Electron Microscopy
SHNO	Spin-Hall Nano-Oscillator
STO	Spin Torque Oscillator
STT	Spin Transfer Torque

Publications

List of papers included in this thesis:

I **E. Iacocca**, R.K. Dumas, L. Bookman, S.M. Mohseni, S. Chung, M. Hoefer, and J. Åkerman, *Confined dissipative droplet solitons in spin-valve nanowires with perpendicular magnetic anisotropy*, Phys. Rev. Lett. **112** (2014), 047201.

II **E. Iacocca**, O. Heinonen, P.K. Muduli, and J. Åkerman, *Generation linewidth of mode-hopping spin torque oscillators*, Phys. Rev. B **89** (2014), 054402.

III R.K. Dumas, **E. Iacocca**, S. Bonetti, S.R. Sani, S.M. Mohseni, A. Eklund, J. Persson, O. Heinonen, and J. Åkerman, *Spin-wave-mode coexistence on the nano-scale: A consequence of the Oersted-field-induced asymmetric energy landscape*, Phys. Rev. Lett. **110** (2013), 257292.

IV **E. Iacocca** and J. Åkerman, *Resonant excitation of injection-locked spin-torque oscillators*, Phys. Rev. B **87** (2013), 214428.

V **E. Iacocca** and J. Åkerman, *Analytical investigation of modulated spin-torque oscillators in the framework of coupled differential equations with variable coefficients*. Phys. Rev. B **85** (2012), 184420.

VI **E. Iacocca** and J. Åkerman, *Destabilization of serially connected spin-torque oscillators via non-Adlerian dynamics*, J. Appl. Phys. **110** (2011), 103910 [Selected for publication in the Virtual Journal of Nanoscale Science & Technology, December 12, 2011].

List of papers related to, but not included in this thesis:

1. A. Eklund, S. Bonetti, S.R. Sani, S.M. Mohseni, J. Persson, S. Chung, A. Banuazizi, **E. Iacocca**, M. Östling, J. Åkerman, and G. Malm, *Dependence of the colored frequency noise in spin torque oscillators on current and magnetic field*, Appl. Phys. Lett. **104** (2014), 092405.

2. P. Dürrenfeld, **E. Iacocca**, J. Åkerman, and P.K. Muduli, *Parametric excitation in a magnetic tunnel junction-based spin torque oscillator*, App. Phys. Lett. **104** (2014), 052410.

3. S.M. Mohseni, S.R. Sani, R.K. Dumas, J. Persson, T.N. Anh Nguyen, S Chung, Ye. Pogoryelov, P.K. Muduli, **E. Iacocca**, A. Eklund, and J. Åkerman, *Magnetic droplet solitons in orthogonal nano-contact spin torque oscillators*, Physica B **435** (2014), 84.

4. S.M. Mohseni, S.R. Sani, J. Persson, T.N. Ahn Nguyen, S. Chung, Ye. Pogoryelov, P.K. Muduli, **E. Iacocca**, A. Eklund, R.K. Dumas, S. Bonetti, A. Deac, M.A. Hoefer, and J. Åkerman, *Spin torque-generated magnetic droplet solitons*, Science **339** (2013), 1295.

5. Y. Zhou, V. Tiberkevich, G. Consolo, **E. Iacocca**, B. Azzerboni, A. Slavin, and J. Åkerman, *Oscillatory transient regime in the forced dynamics of a nonlinear auto oscillator*, Phys. Rev. B **82** (2010), 012408.

6. Ye. Pogoryelov, P.K. Muduli, S. Bonetti, **E. Iacocca**, F. Mancoff, and J. Åkerman, *Frequency modulation of spin torque oscillator pairs*, Appl. Phys. Lett. **98** (2010), 19250.

List of review and invited papers related to this thesis:

1. R.K. Dumas, S.R. Sani, S.M. Mohseni, **E. Iacocca**, Ye. Pogoryelov, P.K. Muduli, S. Chung, P. Dürrenfeld, and J. Åkerman, *Recent advances in nano-contact spin torque oscillators*, IEEE. Trans. Magn. (2014), *in press.*

2. S. Chung, S.M. Mohseni, S.R. Sani, **E. Iacocca**, R.K. Dumas, T.N. Anh Nguyen, Ye. Pogoryelov, P.K. Muduli, A. Eklund, M. Hoefer, and J. Åkerman, *Spin transfer torque generated magnetic droplet solitons*, J. Appl. Phys. **115** (2014), 172612.

3. O. Heinonen, P.K. Muduli, **E. Iacocca**, and J. Åkerman, *Decoherence, mode hopping, and mode coupling in spin torque oscillators*, IEEE Trans. Magn. **49** (2013), 4398.

List of related manuscripts in preparation:

1. **E. Iacocca**, P. Dürrenfeld, R.K. Dumas, and J. Åkerman, *Energy landscape fine-tuning of localized spin wave modes in elliptical nano-contact spin torque oscillators*, (2014).

2. Y. Zhou, **E. Iacocca**, R.K. Dumas, F.C. Zhang, and J. Åkerman, *Magnetic droplet skyrmions*, **arXiv:1404.3281** (2014).

3. R. Sharma, P. Dürrenfeld, **E. Iacocca**, J. Åkerman, and P.K. Muduli, *Frequency noise in a magnetic tunnel junction-based spin torque oscillator*, (2014).

Acknowledgments

So this is it. After seven years in touch with the world of magnetism and spintronics, I have completed a path that took me from being an aspiring engineer in robotics to a full-fledged physicist. This path has opened many new roads, some more rocky than others, and possibilities that I had never considered before.

None of these achievements could have been possible without the support and the encouragement of Prof. Johan Åkerman ever since I was an undergrad student. When I look back at those moments, I can appreciate how much Johan's mentoring and continual discussions have been valuable in every aspect of my professional life. Johan, I am truly thankful for everything you have taught me and all those new roads that you have opened in my path.

Through all these years, people has come and gone from the group. I am particularly thankful to two individuals from whom I have learned many things and, in some ways, they have been role models to me: Dr. Stefano Bonetti and Dr. Randy K. Dumas. I believe I have been very lucky to share time and even research projects with them. As a student, being able to witness their work is priceless. Stefano, *grazie mille e ti auguro tanta fortuna nei tuoi prossimi progetti. In bocca al lupo!* Randy, thank you very much for everything, I really appreciate it, and the very best luck achieving your goals.

My sincere thanks to Dr. Olle Heinonen and Prof. Mark Hoefer with whom I have shared good times and exciting research projects. Working with you has been an enriching experience that has broadened my perception and insight into subjects I did not think I would ever approach.

Big thanks to the people in the group and NanOsc with whom I have had the chance to share time and work with: Fredrik Magnusson, Johan Persson, Yan Zhou, Sohrab Sani, Yeyu Fang, Pranaba Muduli, Yevgen Pogoryelov, Valentina Bonanni, Anders Eklund, Majid Mohseni, Nadjib Benatmane, Sunjae Chung, Ahn Nguyen, Tuan Le, Philipp Dürrenfeld, Mojtaba Ranjbar, Fatjon Qejvanaj, Afshin Houshang, Masoumeh Fazlali, Michael Balinskiy, Mohammad Haidar, Ahmad Awad, Martina Ahlberg, and Yuli Yin.

Special thanks to my examiner Prof. Robert Shekhter and co-supervisor Prof. Bernhard Mehlig. I also extend my gratitude to the administrative staff that patiently have helped us to navigate through the paperwork maze: Bea Augustsson, Johanna Gustavsson, and Ann-Christin Räätäri; and to the Head of the Department, Mattias Goksör.

Many thanks to all the people I have met at conferences and with whom I had the opportunity to share very interesting scientific discussions, great dinners, the traditional conference *bierstube*, American style all-you-can-eat,

and 30 dollars Gran Marnier shots: Andrei Slavin, Joo-Von Kim, Thomas Silva, Giovanni Carlotti, Xavier Waintal, Stavros Komineas, Aurelien Manchon, Vito Puliafito, Paolo Bortolotti, Christoforos Moutafis, Silvia Tacchi, Federico Montoncello, Massimiliano d'Aquino, Giovanni Finocchio, Giancarlo Consolo, Marco Battiato, Marco Madami, Gianluca Gubbiotti, David Luc, Joseph Davies, Peter Greene, and Hatem ElBidweihy.

Finally, I would like to thank my family which has been always there to support me in so many ways, Diodoro, Antonietta, Carmen, and Marlon, my new family José, Argelys, Christopher, and Laura, and of course my beloved wife Krisel. To the youngsters, Fabrizio, Alessia, and Javier, I wish you the best and I hope this thesis can serve you in the future as a remainder to never give up, follow your dreams and opportunities, and put all your effort in everything you do.

Calm and still
Is the forceful mind
Firmly guided by
Heart and will

Kiuas

1
Introduction

The phenomenon of magnetism has been at the heart of mankind's technological development and physical understanding since magnetite was found thousands of years ago. Although it is difficult to attribute its discovery to a specific population, the term "magnetism" derives from the name of the Greek region of Magnesia, which had abundant quantities of magnetite. Since then, magnetic materials have been part of human life. However, a major leap towards a modern world was taken when the magnetic compass was introduced, revolutionizing sailing and improving trade and cultural exchange.

From a physical point of view, the understanding of magnetism began in 1820, when Hans Christian Oersted observed the motion of a magnetic needle close to a conducting wire. The main message behind Oersted's studies was that both the electric and the magnetic fields were related to the particles' charge. This fact lead to the development of electromagnetism, summarized in the celebrated Maxwell's equations, and the understanding of physics from a new perspective.

The physical understanding of magnetism ever since has been intimately related to some of the most exciting technological developments in the last century. In the interest of this thesis, we primarily find magnetic materials used in data storage as we know it today, starting from the 1024 bits magnetic-core memory introduced in 1950, up to the discovery of the giant magnetoresistance effect, which marked the beginning of the so-called field of Spintronics [1, 25] and allowed a dramatic miniaturization of hard drives around 1997. In addition, magnetism finds many more applications, from electric motors in toys to hydroelectric generators, from magnetic strips in fridge stickers to credit card security.

The richness of magnetic applications and the relatively recent understanding of magnetism is promising for new and exciting developments in the near future. One of the approaches that has attracted the interest of the scientific community in the last two decades is the nanoscopic excitation of magnetization *dynamics*. In contrast to the well-established logic devices based on two magnetization states, magnetization dynamics offer a continuum of states characterized by frequency and phase.

The onset of magnetization dynamics at the nanoscale is possible by the spin transfer torque (STT) effect predicted by Slonczewski [122] and Berger [6]

in 1996. The STT effect reveals that the spin of electrons can transfer momentum to the magnetization of a magnetic material and thus, at high enough current densities, induce magnetization dynamics.

The STT effect and the excited dynamics are strongly non-linear. Such nonlinearities have led to the observation of markedly different dynamical modes depending on the materials used, nano-patterning geometries, magnitude and direction of external fields, and current magnitude and polarization. This extensive range of magnetodynamics is observed in devices referred to as spin torque oscillators (STOs).

Generally, steady magnetization dynamics spanning several orders of magnitude can be excited in STOs. For instance, magnetic vortex-based STOs usually generate in the range of 100 MHz to 1 GHz, magnetic tunnel junctions from 1 GHz to $\sim$ 10 GHz, and metallic STOs from 10 GHz up to 60 GHz. Due to this wide selection of frequencies, STOs have usually been envisioned as devices useful for communication applications and as signal generators, where high frequencies are desired without compromising the miniaturization process, and, more recently, as magnonic and neuromorphic building blocks [11, 78]. However, STOs generally suffer from a very low output power (approximately three orders of magnitude below the minimum μWatts requirements) and a very large linewidth. In order to improve these characteristics, a significant amount of research has been devoted to understand the origin and properties of the excited dynamics.

The STO dynamical characteristics can be improved, for instance, by refining the nano-fabrication process and carefully choosing the materials and structure for the STO. In this thesis, however, we focus on a more fundamental approach relying on the STO's interactions and the understanding and control of strongly non-linear dynamics.

The original work performed in this thesis can be divided into three main topics:

1. **External perturbations:** The interaction between the STO and external perturbation leads to technologically relevant effects. Injection locking and synchronization are features of auto-oscillatory systems that can potentially lead to both linewidth reduction and power enhancement and are currently some of the proposed solutions to make STOs technologically feasible. Modulation is of fundamental importance in communication applications and STOs can potentially reduce the footprint of transceivers and microwave circuitry. The focus here is on the effect of strong nonlinearities on these concepts leading to the identification of figures of merit and limitations, which have been determined using numerical and analytical methods.

2. **Multi-mode generation:** The strong nonlinearity of STOs sets them apart from linear electronic oscillators particularly due to their multi-mode generation. Although STOs have been considered single-mode oscillators, we show here that this is generally not the case. Indeed, multi-mode generation is responsible for the recently observed mode coexistence. By means of simulations, analytical calculations, and experiments

we have achieved a good understanding of the underlying dynamics, which allows us to control their characteristics at the nanoscale.

3. **Topological droplets:** These structures have attracted the attention of scientists in recent years due to the experimental observation of magnetic dissipative droplets and Skyrmions. In the spirit of nanoscopic applications, here we study the effect of physical confinement on dissipative droplets from a numerical and analytical perspective, leading to the description of novel topological modes that potentially have applications in the fields of applied and fundamental physics.

2

Magnetism

2.1 Free electron magnetism

Since the discovery of the phenomenon of magnetism, its origin has been explained by several arguments, usually involving the physical understanding of the time. The current understanding of magnetism can be linked to quantum mechanical principles. From this perspective, new effects can be explained, as in the case of the spin transfer torque effect, which is of fundamental importance in this thesis. This section offers an overview of the origin of the relevant magnetic properties covered in this thesis.

2.1.1 The relativistic Hamiltonian

In a quantum mechanical framework, particles are represented by wavefunctions, $|\Psi\rangle$, obeying Schrödinger's equation. In the relativistic limit, when the particles approach the speed of light, Dirac proposed a four-component equation with a Hamiltonian expressed as

$$\mathcal{H} = c_l \boldsymbol{\alpha_D} \vec{p} + \boldsymbol{\beta_D} m c_l^2, \tag{2.1}$$

where c_l is the speed of light, $\vec{p}$ and m are, respectively, the momentum and mass of the particle, and $\boldsymbol{\alpha_D}$ and $\boldsymbol{\beta_D}$ are 4×4 matrices satisfying the identity matrix relation $\boldsymbol{\alpha_D}^2 + \boldsymbol{\beta_D}^2 = \mathbf{1}$. This Hamiltonian introduced the concept of a novel particle with negative energy, the positron. Although ground-breaking for fundamental physics, in this thesis we are interested in the effect of an electromagnetic field on such particles. Unfortunately, the Dirac Hamiltonian couples both positive and negative energy particles making a transition to a non-relativistic limit impossible. A solution to this problem was formulated by Foldy and Wouthuysen [47], showing that a canonical transformation could both decouple and represent the Dirac particles with new, average, operators that are directly equivalent to non-relativistic operators. In particular, they introduced the concept of *mean position* and *mean velocity*, both following the classical interpretation.

In order to introduce the effect of an electromagnetic field on an electron of charge e, the Dirac Hamiltonian is expanded with the vector and scalar

potentials, respectively, $\boldsymbol{A}$ and ϕ_E, reading

$$\mathcal{H} = c_l \boldsymbol{\alpha_D} \left(\vec{p} - |e|\boldsymbol{A}\right) + \boldsymbol{\beta_D} m c_l^2 - |e|\phi_E. \tag{2.2}$$

The introduction of the electromagnetic field precludes the use of the canonical transformation introduced by Foldy and Wouthuysen. However, the same authors proposed an expansion series of canonical transformations approaching the exact solution to an order of $1/m$. For relatively weak fields (of the order studied in this thesis) an expansion up to the second order yields the positive-energy Hamiltonian

$$\begin{aligned} \mathcal{H} &= mc_l^2 - |e|\phi_E + \frac{1}{2m}\left(\vec{p} - |e|\boldsymbol{A}\right)^2 - \frac{\mu_o |e|}{2m}\boldsymbol{\sigma}\cdot\vec{H} \\ &\quad - \frac{|e|}{4m^2 c_l^2}\boldsymbol{\sigma}\cdot\vec{E}\left(\vec{p} - |e|\boldsymbol{A}\right) + \frac{|e|\hbar^2}{8m^2 c_l^2}\nabla\cdot\vec{E}, \end{aligned} \tag{2.3}$$

where we have used the definitions of the electric field $\vec{E} = -|e|\nabla\phi_E - \partial\boldsymbol{A}/\partial t$, the magnetic flux $\vec{B} = \mu_o\vec{H} = \nabla\times\boldsymbol{A}$ satisfying Maxwell's equations, and the Pauli matrices $\boldsymbol{\sigma}$ originating from the Dirac matrix $\boldsymbol{\alpha_D}$. The Hamiltonian of Eq. (2.3) contains the main ingredients to describe the magnetic phenomena on a free electron. In the following we discuss each term of the right-hand side (RHS) of Eq. (2.3), neglecting the static contribution of the relativistic and potential energies, respectively, mc_l^2 and $|e|\phi_E$, which are considered to be reference levels.

- The third term provides important information on the action of a magnetic field on the electron. Under the assumption of a uniform external field and Coulomb gauge, $\nabla\cdot\boldsymbol{A} = 0$, this term can be expanded as

$$\frac{1}{2m}\left(\vec{p} - |e|\boldsymbol{A}\right)^2 = \frac{\vec{p}^2}{2m} + \frac{\mu_o|e|}{2m}\vec{H}\cdot\boldsymbol{l} + \frac{\mu_o^2|e|^2}{8m}\left(\vec{H}\times\vec{r}\right)^2, \tag{2.4}$$

  where we have used $\boldsymbol{A} = \mu_o(\vec{H}\times\vec{r})/2$ and $\vec{r}\times\vec{p} = \boldsymbol{l}$ describing the orbital moment of the electron, where $\vec{r}$ is the radial distance from the nucleus. This expansion leads to three terms representing, respectively, the kinetic energy, the *paramagnetic* interaction between a field $\vec{H}$ and the orbital momentum, and the generally weak *diamagnetic* term.
- The fourth term directly describes the interaction between the field $\vec{H}$ and the spin of the electron. This term will eventually lead to one of the strongest contributions in magnetism, the Zeeman energy.
- The fifth term is more complicated. We assume a stationary field so that $\nabla\times\vec{E} = 0$ by virtue of Maxwell's equations and that the vector potential has spherical symmetry, as expected from a point charge. It is then possible to express this term as

$$\frac{|e|}{4m^2c^2}\boldsymbol{\sigma}\cdot\vec{E}\left(\vec{p} - |e|\boldsymbol{A}\right) = -\frac{|e|}{4m^2c^2}\frac{1}{r}\frac{\partial V}{\partial r}\boldsymbol{\sigma}\cdot\vec{r}\times\vec{p} = -\xi_{so}\boldsymbol{\sigma}\cdot\boldsymbol{l} \tag{2.5}$$

  The simple final expression indicates the interaction between the electron's spin and orbital momentum, known as the spin-orbit coupling.

In other words, the spin of the electron is affected by its own motion. This effect is fundamental in the description of the magnetocrystalline anisotropy and energy dissipation, as discussed later.

- Lastly, the sixth term is known as the Darwin term and represents the fluctuation of the electron's position in the Dirac representation, or *zitterbewegung*. This is caused by the odd operators and hence coupling to negative energy particles that do not allow an arbitrary precision of the position operator. The exact canonical transformation proposed by Foldy and Wouthuysen eliminates this problem by defining the new *mean position* operator, where the *zitterbewegung* is averaged out. In the following discussion, this term will be neglected.

The above terms can be rewritten in the Hamiltonian of Eq. (2.3) in order to emphasize the effect of an electromagnetic field on a free electrons as

$$\mathcal{H} = \frac{\vec{p}^2}{2m} - \frac{\mu_B}{\hbar}\left(\boldsymbol{l} + \boldsymbol{\sigma}\right) \cdot \mu_o \vec{H} + \xi_{so}\boldsymbol{\sigma} \cdot \boldsymbol{l} + \frac{\mu_0^2 e^2}{8m}\left(\vec{H} \times \vec{r}\right)^2, \tag{2.6}$$

where we use the Bohr's magneton $\mu_B = |e|\hbar/(2m)$.

2.1.2 Magnetic moment operator

In order to probe the free electron properties derived in the previous section, an appropriate operator must be defined as is customary in the quantum mechanical framework. By use of Maxwell-Faraday's equation, it can be shown e.g. Ref. [138], that the work functional is related to the magnetic moment as $\delta_o W = \partial E = -\vec{\mu}_M \partial \vec{H}$ leading to the relation

$$\vec{\mu}_M = V_s \vec{M} = -\frac{\partial E}{\partial \vec{H}}, \tag{2.7}$$

where E is energy and we define the magnetization $\vec{M}$ as the magnetic moment per unit volume V_s. In order to relate Eq. (2.7) to a quantum mechanical framework, it is possible to differentiate Schrödinger's equation with respect to field

$$\left(\frac{\partial \mathcal{H}}{\partial \vec{H}} - \frac{\partial E}{\partial \vec{H}}\right)|\Psi\rangle + \left(\mathcal{H} - E\right)|\frac{\partial \Psi}{\partial \vec{H}}\rangle = 0 \tag{2.8}$$

Performing the average by adding the bra $\langle\Psi|$ and rearranging Eq. (2.8), we obtain

$$\langle\Psi|\frac{\partial \mathcal{H}}{\partial \vec{H}}|\Psi\rangle - \langle\Psi|\frac{\partial E}{\partial \vec{H}}|\Psi\rangle = -\langle\Psi|\left(\mathcal{H} - E\right)|\frac{\partial \Psi}{\partial \vec{H}}\rangle \tag{2.9}$$

At this point we note that the energy is not an operator so that $\langle\Psi|\boldsymbol{f}E|\Psi\rangle = \boldsymbol{f}E$, where $\boldsymbol{f}$ is any operator on E. Moreover, due to the fact the the Hamiltonian is Hermitian, we can write

$$\langle\Psi|\frac{\partial \mathcal{H}}{\partial \vec{H}}|\Psi\rangle - \frac{\partial E}{\partial \vec{H}} = -\left(\langle\frac{\partial \Psi}{\partial \vec{H}}|\left(\mathcal{H} - E\right)|\Psi\rangle\right)^* \tag{2.10}$$

The second term on the left-hand-side of Eq. (2.10) is $-V_s\vec{M}$ from Eq. (2.7). The right-hand side term is simply zero since $(\mathcal{H} - E)|\Psi\rangle = 0$ by definition. Consequently, we are left with the equality

$$V_s\vec{M} = -\langle\Psi|\frac{\partial\mathcal{H}}{\partial\vec{H}}|\Psi\rangle = -\langle\Psi|\mathcal{M}|\Psi\rangle. \tag{2.11}$$

The magnetic moment operator closes the gap between the quantum mechanical observable and the macroscopic magnetization obtained from Maxwell's equations. Furthermore, it relates the Hamiltonian Eq. (2.6) to a macroscopic observable suggesting that the spin and angular momenta as well as the spin-orbit coupling are manifest in a classical framework.

2.2 Magnetism in transition metals

In the previous section, the interaction between a free electron and an electromagnetic field was derived from the Dirac's relativistic Hamiltonian. Furthermore, it became apparent that the same Hamiltonian could be mapped into a macroscopic variable, the magnetization vector $\vec{M}$, by an operator acting on the wavefunctions in a unit volume. However, a macroscopic unit volume is composed by a large number of atoms, each of them composed of multiple electrons. Such is the case of the 3d transition metals of interest in this work: Fe, Ni, and Co. In the following sections we review the magnetic consequences of such a complex system both from an atomic and a macroscopic perspective, which allows us to define an approximate model for the magnetic Hamiltonian. A complete review on this complex subject can be found in Ref. [127].

2.2.1 Electronic localization

The $3d$ transition metals have an electronic configuration where shells are filled up to the $4s$ shell while the $3d$ shell is half-filled. By virtue of Pauli's exclusion principle, such half-full $3d$ shell possesses a net magnetic moment, as the electrons have the same spin and different orbitals in order to reduce the energy by antisymmetrization of their wavefunctions. Remarkably, the $3d$ electrons are subjected to an attractive Coulomb potential and a repulsive kinetic potential leading to a well-defined charge density in the atom, as shown in Fig. 2.1. In other words, the $3d$ electrons are *localized* at a given distance from the nucleus. A similar situation is found in the rare-earths in which the $4f$ shell is strongly localized.

2.2.2 Band structure

In a macroscopic solid, the electron structure described above is further perturbed by the presence of other atoms. A powerful tool to study the consequences of such inter-atomic interactions is the band theory of solids. In band theory, the core electrons –the Ar structure for $3d$ transition metals– are assumed fixed, while the valence electrons are free to move in momentum

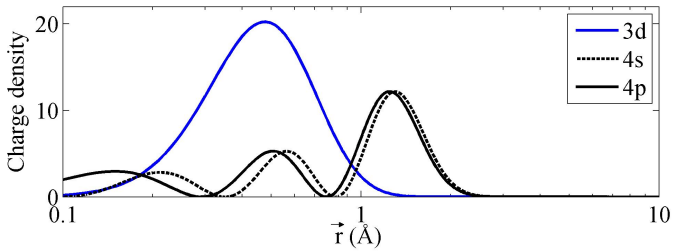

Figure 2.1: Charge density of the $3d$, $4s$, and excited $4p$ electrons in a transition metal atom similar to Fe as a function of the distance from the nucleus $\vec{r}$. The $3d$ electrons are most likely to be found close the nucleus due to energy balance between the Coulomb and kinetic potentials (Adapted from Ref. [127]).

and energy space, i.e., to physically move around the solid or be excited to a higher energy orbital. Metals are solids which happen to have a continuous band structure in contrast to semi-conductors and insulators whose valence band lies a few eV below the so-called conduction band, thus defining an energy band-gap [4, 36]. The continuous band structure of metals precludes a distinction between valence and conduction band and instead, electrons fill the available bands up to the Fermi energy, E_F. The number of electrons at any particular energy is visualized and measured as a density of states (DOS).

When the magnetic moment of the atom is taken into account, the DOS of the $3d$ transition metals exhibit an energy splitting between the two available spins, as shown in Fig. 2.2 for Fe, Co, and Ni. This can be attributed to the atomic bonding for a given lattice structure, as in the case of calculated band structures based on density functional theory [127]. In $3d$ transition metals, such a splitting occurs about E_F, so that the band with lower energy, or majority band (blue), is more populated than the higher energy, or minority, band (gray). The majority band hence defines a preferential spin orientation in the material leading to a *ferromagnetic* ordering, which is the basis of the Stoner model [126]. It is noteworthy that the magnetization orientation is *anti-parallel* to the majority band by definition, as inferred from Eq. 2.11. Additionally, $3d$ electron states in transition metals are not fully occupied at the Fermi energy, suggesting that these electrons posses a de-localized or *itinerant* character in contrast to the localization discussed in the previous section. For this reason, $3d$ transition metals are a complex system to study, where both localized and itinerant electrons must be taken into account in different scenarios and approximations.

2.2.3 Exchange coupling

The two models described above, atomic and band structure, represent markedly different limits of the $3d$ electrons behavior, namely localized or itinerant. As a common feature, both models describe the ground state of the system, i.e., at a temperature of 0 K. For a physically relevant picture, tem-

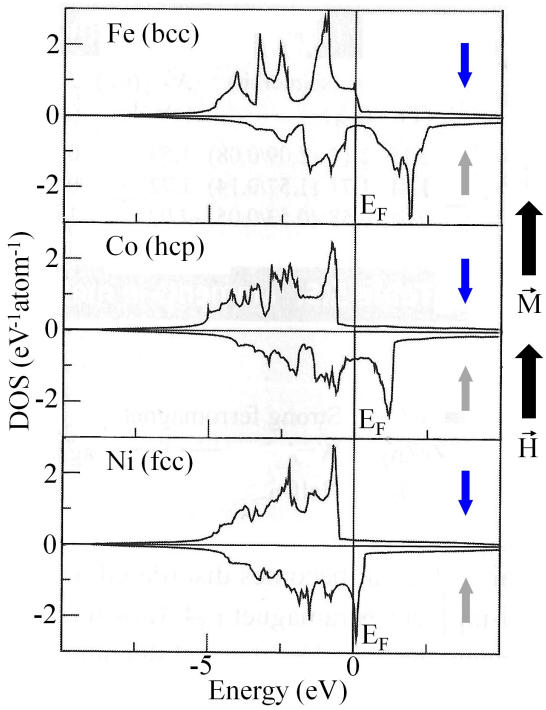

Figure 2.2: Spin-dependent density of states (DOS) for Fe, Co, and Ni. An uneven number of electrons are found up to the Fermi energy, E_F, defining a majority (blue) and minority (gray) band, and consequently the magnetization $\vec{M}$ (black arrow). Note that the magnetization is anti-parallel to the majority band spin orientation due to Eq. 2.11. The $4s$ and $4p$ bands are equally populated above E_F, demonstrating that the spin-splitting is due to the $3d$ electrons. The band structure also shows that the $3d$ electrons are itinerant (Adapted from Ref. [27]).

perature must be taken into account and the magnetic model must correlate with the experimental observations. The inclusion of temperature in a quantum mechanical picture means that the system has enough additional energy to allocate electronic excited states. The excitation and decay of such states together with the fact that electrons are indistinguishable from one another, leads to an additional term in the Hamiltonian known as *exchange*. In other words, such a Hamiltonian denotes the energy needed to exchange an electron in a quantum mechanical state by another electron in a different quantum mechanical state. A noteworthy point is that the spin is only taken into account as an antisymmetrization argument for the electron's wavefunction, and thus exchange is only related to Coulomb forces.

In the itinerant picture of magnetism, the exchange energy promotes an electron into an excited state. There are two possibilities: either a change in the orbital quantum number or a change in the spin quantum number. This

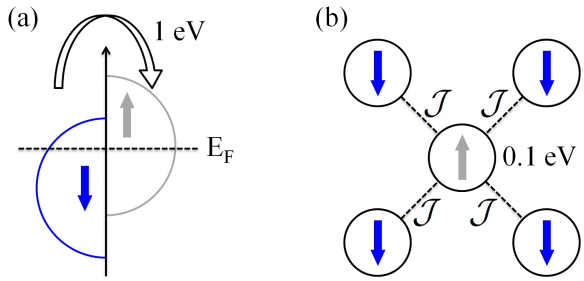

Figure 2.3: Electronic exchange in: (a) the Stoner model of ferromagnetism where an electron in the majority band is exchanged to the minority band; (b) the Heisenberg model where the valence electrons are exchanged into the minority band.

kind of exchange is extremely energy consuming, on the order of 1 eV, as it involves a single electron of the majority band switching to the minority band [Fig. 2.3(a)]. This description leads to the conclusion that magnetic ordering is lost at a temperature $T_C = 1$ eV$/k_B \approx 10,000$ K, known as the Curie temperature. However, the Curie temperature estimated in this way is an order of magnitude above the experimental values for the $3d$ transition metals.

The problem with the Stoner-type exchange lies in the fact that the $3d$ transition metals are not purely itinerant, and the $3d$ electrons are mostly localized close to the atomic nuclei as discussed above. A theory that takes into account both localized and itinerant electrons has not yet been developed [127], and an approximate picture is generally used. The localization of the $3d$ electrons leads to the definition of spatially localized atomic moments that interact with each other via Coulomb forces. From this picture, the exchange energy describes an atom switching its spin momentum with respect to the majority band [Fig. 2.3(b)]. This energy turns out to be on the order of 0.1 eV, which is consistent with the experimentally observed T_C. This kind of exchange can be represented with a Heisenberg Hamiltonian of the form

$$\mathcal{H}_{ex} = -2\mathcal{J}\sum \boldsymbol{s}_i \cdot \boldsymbol{s}_j, \tag{2.12}$$

where $\mathcal{J}$ is the exchange constant and $\boldsymbol{s}$ are atomic spins of neighboring atoms. Due to the localized character of this picture, only the closest neighbors are taken into account. The Hamiltonian of Eq. (2.12) is widely used to numerically study magnetization dynamics, as discussed later, and uncovers the existence of low temperature (with respect to T_C) collective excitations known as spin waves and discussed in the next section.

In summary, the origin of ferromagnetism in $3d$ transition metals can be understood from the Stoner model of itinerant electrons and spin-split valence bands while the exchange has a more localized origin, and can be represented in terms of the Heisenberg Hamiltonian of Eq. (2.12). There are other exchange mechanism such as superexchange in $3d$ transition metal oxides, double exchange in materials with differently charged ions e.g. magnetite where

both Fe^{+2} and Fe^{+3} ions are present, and the Ruderman-Kittel-Kasuya-Yosida (RKKY) interaction taking place between localized yet distant moments e.g. multilayers or rare-earth doped semiconductors. None of the latter exchange coupling mechanisms are directly relevant for the materials and effects studied in this thesis and they will be neglected in the following discussions.

2.2.4 Spin waves

The exchange coupling between neighboring atoms given by Eq. (2.12) promotes parallel (anti-parallel) spin orientations if $\mathcal{J}$ is positive (negative). In other words, the exchange coupling acts as a restoring force between the atomic spins. If we now suppose that one atomic spin is suddenly tilted by means of temperature, for instance, the neighboring atomic spins will compensate such motion by tilting in the opposite direction. Such motion can propagate in the solid similarly to the way atomic vibrations i.e., phonons do [36]. This collective atomic spin motion is known as spin waves.

As for phonons, it is possible to treat spin waves in a quasi-particle fashion by making use of second quantization formalism i.e., using creation and annihilation operators for a given ground state [138]. The resulting quasi-particle is known as *magnon* and obeys Bose-Einstein's statistics i.e., it has an integer spin which releases it from the Pauli exclusion principle. The interaction of magnons of different $\boldsymbol{k}$ vectors leads to 2-, 3-, and 4-component scattering processes that re-distribute the energy in the ensemble and to the lattice (and thus phonons) by virtue of the spin-orbit coupling [128, 65]. This picture is similar to the Caldeira-Legget model [22] which converts a purely conservative system into a Langevin equation with the only assumption of random events, in agreement with the fluctuation - dissipation theorem [109, 134]. Consequently, the existence and interactions of magnons is fundamental to understand the low-temperature dynamics of magnetic materials and validates the Heisenberg exchange Hamiltonian.

2.2.5 Perpendicular magnetic anisotropy

Until this point, the discussion of magnetism has taken into account macroscopic materials in the sense that their dimensions are infinite with respect to quantum mechanical length scales. Consequently, magnetism from this perspective is completely isotropic. However, it was mentioned earlier that the spin-orbit coupling obtained from the expansion of the Dirac Hamiltonian, Eq. (2.1), could induce magnetic anisotropy. In solids, the atomic lattice provides the spatial basis for the orbital moments of electrons due to atomic bonding [127]. Thus, for each electron, the spin-orbit coupling defines a preferential spin orientation according to the atomic lattice, referred to as magnetocrystalline anisotropy. It is instructive to study the case of a purely two-dimensional lattice, or monolayer [Fig. 2.4(a)]. From ligand theory [127], the neighboring atoms' ligand electrons create a Coulomb potential landscape in the monolayer plane. Consequently, the electron orbit is weakly perturbed in the out-of-plane direction (blue) and so the spin tends to be oriented along

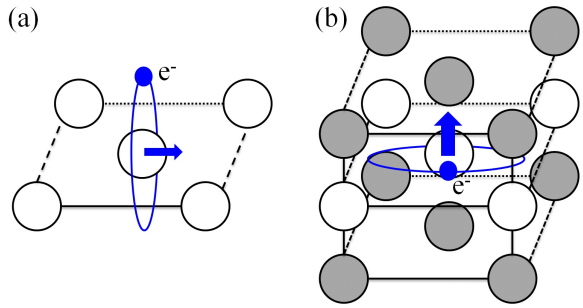

Figure 2.4: (a) Ferromagnetic monolayer where the electron orbit (blue) is less perturbed in the $\hat{z}$ direction and thus an in-plane anisotropy is preferred. (b) When the monolayer is sandwiched between heavier metals (gray), the electron orbit is less perturbed in the monolayer's plane, usually leading to a large perpendicular anisotropy.

the lattice. This effect is very weak and usually neglected for the materials of interest here. However, magnetocrystalline anisotropy is measurable and, in agreement with ligand theory, its strength depends on the atomic lattice [51].

The same mechanism described above can be used to model, in a very simplified way, the behavior of a monolayer sandwiched between metallic layers. If heavier metals are used (gray) the electron's orbit becomes less perturbed in the monolayer's plane [Fig. 2.4(b)] thus promoting an out-of-plane magnetic moment, as shown for Co/Pd multilayers [23] and Au/Co/Au trilayers [20]. Furthermore, Daalderop *et al.* [32] predicted a similar effect in $3d$ transition metal multilayers based on the induced magnetic polarization of non-magnetic metals. These materials are of interest in the present thesis, particularly Co/Ni multilayers as studied in Ref. [32].

2.3 Electronic transport in magnetic materials

The electronic transport in magnetic materials is of fundamental importance for technological applications and the results presented in this thesis. As discussed above, $3d$ transition metals have an itinerant character as the $3d$, $4s$, and $4p$ electrons are available at the Fermi energy according to the band structure and are responsible for the transport properties. The fact that the material is magnetic leads to fundamental differences compared to the transport of non-magnetic metals and to the existence of the spin transfer torque effect discussed below.

2.3.1 Two-current model

Transport in metals can be described in terms of the displacement of the Fermi surface due to an external voltage [Fig. 2.5(a)]. The displacement of

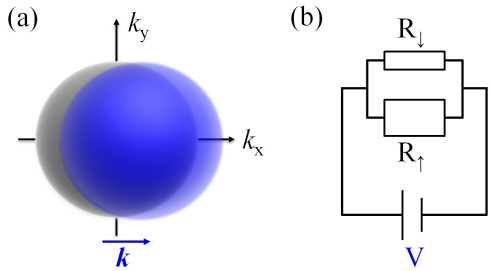

Figure 2.5: (a) Schematic representation of a Fermi surface (gray) and its non-equilibrium distribution (blue) when a voltage is applied. The finite displacement of the Fermi surface leads to a $\boldsymbol{k}$ vector or motion of the electrons. (b) Two-current model for electronic conduction in magnetic materials, with resistances for the majority ($R_\downarrow$) and minority ($R_\uparrow$) bands satisfying $R_\downarrow > R_\uparrow$.

the Fermi surface (gray) leads to a non-equilibrium distribution of electronic states (blue) eventually developing a $\boldsymbol{k}$ vector and hence flow through the metal. The displacement of electrons have been commonly understood from two equivalent schools of thought: the diffusive and the ballistic models. In the diffusive model, the non-equilibrium dynamics of the electron are represented by a Boltzmann equation under the customary approximation of long equilibration time, leading to the Drude model of conductivity. Alternatively, the ballistic model assumes an electron that is only perturbed by elastic scattering giving rise to reflection and transmission probabilities in the Landauer-Büttiker formalism [21]. Both understandings of electron transport in metals are equivalent, by virtue of Einstein's relation.

For $3d$ transition metals, electronic transport acquires a new degree of freedom due to the $3d$ band splitting at the Fermi energy. As discussed before, the $3d$ band splitting defines majority and minority electrons and thus a preferential magnetic moment. It follows that the majority band has less available states than the minority band just above the Fermi energy [Fig. 2.2]. Assuming that transport can be understood as in non-magnetic metals, the electrons will acquire a $\boldsymbol{k}$ vector when a voltage is applied. However, the fact that the bands are unevenly filled leads to a different $\boldsymbol{k}$ vector depending on the spin orientation. Consequently, the electronic transport can be assumed to take place independently in each band. Such an assumption is valid since the probability of a scattering event between the majority and minority bands, or spin-flip, is very low [127] although necessary to satisfy thermodynamic equilibrium on a much longer time scale. This is the so-called two-current model of transport in metallic ferromagnets.

One immediate consequence of the two-current model is that the conductivity σ, and hence resistivity, depends on the electron's spin. In particular, for $3d$ transition metals, the $3d$ and $4s$ electrons close to the Fermi energy E_F are responsible for the conduction [see Fig. 2.1]. However, from their band structure, the $4s$ electrons have generally a lower effective mass than the $3d$ electrons. Consequently, the conductivity of each spin channel is limited by

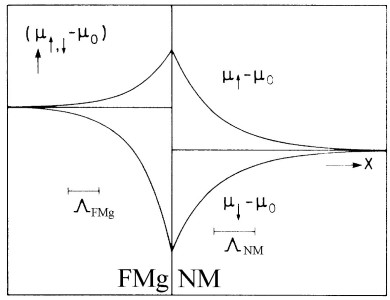

Figure 2.6: Variation of the chemical potential close to the transition between a FMg and a NM metal from Ref. [135]. The exponential transition is characterized by the spin-diffusion length in the FMg and NM metal.

the scattering events between the fast $4s$ electrons and the slow $3d$ electrons. It follows that the scattering is higher for the minority band as many more states are available at E_F and, by virtue of Matthiessen's rule [4], the total conductivity of $3d$ transition metal will be dictated by the majority band. The two-current model is thus equivalent to a circuit of two spin-dependent resistors in parallel [Fig. 2.5(b)]. Considering spin-orbit coupling, this model is the basis for the anisotropic magnetoresistance (AMR) effect where the resistance of the material is dependent on the relative direction of the metal's magnetization with respect to the current path.

2.3.2 Spin accumulation

The two-current model treats the magnetic metal as a stand-alone material. However, in any realistic application, it is possible to apply a potential by contacting the magnetic metal. By virtue of their high conductivity, the materials of choice for electric conduction are usually Cu and Au. Consequently, it is interesting to study the effect of an interface between a ferromagnetic (FMg) and a non-magnetic (NM) metal.

Clearly, such an interface presents the problem of different conduction channels at the (new) Fermi energy resulting in a discontinuity i.e. the conduction in NM metal, where the spins are randomly distributed, and the FMg metal where a preferential spin orientation is established. A solution is found by invoking a smooth transition or continuity relations.

By casting the spin-dependent transport equations in the diffusive approximation [135], it is possible to obtain such a smooth transition. The resulting effect is known as *spin-accumulation* and describes the splitting of the spin-dependent electro-chemical potential, $\mu_{\uparrow,\downarrow}$ satisfying $\nabla\mu_{\uparrow,\downarrow} = -|e|\vec{j}/\sigma$, as a function of distance from the interface [Fig. 2.6]. Qualitatively, the spin-accumulation effect predicts:

- The electrons have a definite spin or are spin-polarized in the NM metal close to the interface.
- There is a potential drop at the interface due to the generally different

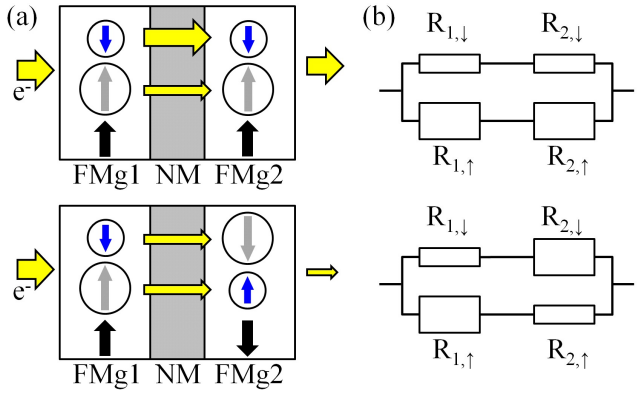

Figure 2.7: (a) Spin valves consisting of two FMg metals separated by a NM spacer. The conduction is schematically shown as electrons scatter into majority (blue) and minority (gray) available states for the case when the magnetization (black arrows) are parallel (top panel) and anti-parallel (bottom panel). The corresponding two-current model circuits are shown in (b).

average electro-chemical potentials in the NM metal (μ_0) and the FMg metal.

- The intrinsic electro-chemical potentials of the NM and FMg metals are exponentially approached from the interface by a characteristic length Λ, or *spin-diffusion length*.

2.3.3 Spin valves and giant magnetoresistance effect

The two-current model and the effect of spin-accumulation can be combined in a more complex structure of technological importance. A spin valve is a trilayered structure consisting of two FMg metals separated by a NM metal or spacer [Fig. 2.7(a)]. In the relevant case where current flows perpendicular to the structure plane, or CPP (yellow arrows), the NM metal has to be sufficiently thick in order to decouple the magnetic moments of the FMg metals, but thin enough to conserve spin-polarization i.e., its thickness is limited by Λ.

The electronic transport in a spin valve is then fully determined by the two-current model in each FMg metal. One of the FMg metals, say FMg1, spin-polarizes the incoming electrons due to the band spin splitting. From this perspective, a FMg metal acts as a *spin filter*. In this process, the scattering events in the majority (blue) and minority (gray) bands determines the conductivity in FMg1. After flowing through the spacer without losing their spin-polarization, the electrons face scattering from the second FMg metal, FMg2. If the magnetizations of both FMg1 and FMg2 are parallel [top panel in Fig. 2.7(a)], the majority and minority spins experience a similar scattering as in the FMg1 so that the majority spins conductivity is maximal. On the contrary, if the FMg metals have an anti-parallel magnetization [bottom

panel in Fig. 2.7(a)], the incoming majority (minority) spins experience a higher (lower) scattering leading to a low conductivity. This effect is known as giant magnetoresistance (GMR) [3] used for read-heads in modern hard drives and for which Albert Fert and Peter Grünberg received the Nobel prize in physics in 2007. The word giant is included in the name because GMR is approximately an order of magnitude higher than the AMR. As in the two-current model, one can visualize GMR in terms of an equivalent passive circuit where the total resistance is strongly biased by the lower resistance conduction channel [Fig. 2.7(b)] by Kirchoff Laws.

2.3.4 Spin transfer torque

In a spin valve, spin-polarized electrons impinge on a FMg metal and their scattering determines the magnetoresistance (MR) of the structure. In the case where the relative direction of the ferromagnets' magnetization is non-collinear, one has to consider the scattering effect of the perpendicular component of the spin. Such a scattering effect can be represented, in a oversimplified manner, as a spin-dependent electron wavefunction crossing a potential, as schematically shown in Fig. 2.8(a). Such a quantum mechanical problem leads to reflection and transmission probabilities, even if the energy of the electron is well above the potential [54]. Taking into account the spin degree of freedom, a non-collinear electron is scattered according to the spinor transformation. By imposing momentum conservation, it becomes apparent that the perpendicular component of the incident wavefunction is not conserved but absorbed by the FMg metal. This effect was described by Slonczewski [122] and Berger [6] in 1996, and it is known as the *spin transfer torque* (STT) effect.

The description of STT, as in the case of electronic transport, can be approached in a rigorous way from different perspectives [125, 104, 56]. However, a consensus has not yet been established and each approach currently has advantages and disadvantages. A detailed theoretical study of the STT effect is outside the scope of this thesis but the understanding of its main features is of fundamental importance. Consequently, and for the sake of clarity, we will briefly discuss the continuous random matrix theory (CRMT) approach [137, 16, 96].

The CRMT approach is largely based on the ballistic conduction of electrons in a Landauer-Büttiker formalism [21] and is particularly useful to describe spin valves where multiple reflection processes take place in the NM spacer. Furthermore, it has been recently shown [96] that CRMT is a generalization, upon appropriate limits, of the diffusive Valet-Fert transport theory [133] and the generalized circuit theory [5].

The basic idea of CRMT is to extend the Landauer-Büttiker formalism to include spin-dependent transport. This is done by defining 4×4 reflection and transmission matrices that incorporate charge and spin transport as well as spin-flip events. This matrix then enters in a generalized scattering matrix $\hat{S}$ describing a ballistic electron in a vanishingly thin FMg metal. It can be shown that $\hat{S}$ can be generalized for a FMg metal of arbitrary thickness [16]. As for

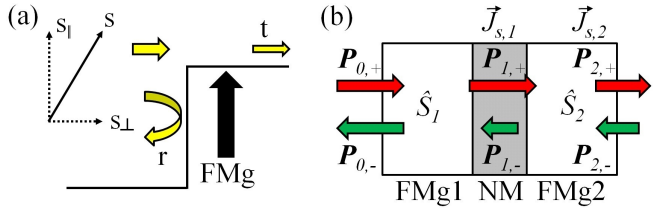

Figure 2.8: (a) Simplified schematic of an electron impinging on a non-collinear FMg metal. As is also the case in quantum mechanics, there is a finite probability for transmitted (t) and reflected (r) wave components. In particular, the perpendicular spin component can be either reflected or absorbed, and it is this component that provides SST. (b) Spin valve as envisioned by the CRMT for spin torque, where the FMg metals are scatterers. The spin currents $\vec{J}_{s,1}$ and $\vec{J}_{s,1}$, define the strength and direction of the torque.

microwave circuits [99], the scattering matrix completely describes the two-terminal problem, i.e., incident and outgoing electrons from the FMg metal are fully described by $\hat{S}$. It is then natural to describe a spin valve in a similar fashion, where a 4 component wave $\boldsymbol{P}$ describes the electrons' charge and spin. The relevant observables can be expressed in terms of the electro-chemical potential (not shown here) and the spin current density (in units of energy per unit area) as

$$\vec{J}_s = \frac{2\hbar\vec{I}_s}{e^2\mathcal{R}_{Sh}}, \tag{2.13}$$

where $\vec{I}_s = \boldsymbol{P}_+ - \boldsymbol{P}_-$ is the spin current using the sign convention of Fig. 2.8(b) and $\mathcal{R}_{Sh} \approx 0.5$ f$\Omega\cdot$m^2 is the Sharvin resistance for unit surface. Following the CRMT formalism, the torque arising in a spin valve is simply defined by the absorbed spin current i.e., the difference between the spin currents impinging on and transmitted through one layer

$$\vec{\tau} = \vec{J}_{s,1} - \vec{J}_{s,2}, \tag{2.14}$$

where the torque here must be understood as the amount of spins deposited on the FMg metal per unit area. This definition, although far from trivial, provides a simple picture of the STT effect as the FMg metal absorbs spin momentum from the non-collinear incoming electrons. Due to the fact that magnetism itself originates from the itinerant electrons close to E_F, such an absorption of momentum can lead to a macroscopic change in the FMg metal magnetization. Furthermore, from Fig. 2.8(b), it can be inferred that the STT is mutual in spin valves i.e., both FMg metals are subjected to STT due to the finite probability of electron reflection. Remarkably, the torque from reflected electrons acquires a negative sign by virtue of the convention of Eq. (2.14). This fact is of fundamental importance for the experimental results discussed in this thesis. Other torque components also arise from CRMT [96], however only the so-called in-plane torque discussed above achieves a relevant magnitude in purely metallic spin valves.

2.4 Semi-classical magnetization dynamics

The previous sections described the origin of ferromagnetism and electronic transport from quantum mechanical principles and microscopic approximations. However, magnetism is a macroscopic phenomenon and as such, a semi-classical description is desired. A first step towards this goal was outlined in section 2.1.2, where the magnetic moment operator could be linked to the macroscopic magnetization per unit volume. In this section, we make use of this relation to obtain a semi-classical expression for the magnetization dynamics.

2.4.1 Landau-Lifshitz equation

The dynamics of the magnetization can be obtained directly from the definition of magnetization in terms of the quantum mechanical magnetic moment operator, Eq. (2.11). The time-dependent expression of the magnetic moment operator in a Heisenberg representation is obtained by Ehrenfest's relation

$$\frac{d}{dt}\langle \mathcal{M} \rangle = \frac{1}{i\hbar}\langle [\mathcal{M}, \mathcal{H}] \rangle + \langle \frac{\partial \mathcal{M}}{\partial t} \rangle. \tag{2.15}$$

To proceed, we shall assume that the average magnetic moment operator is static, so that the last term in Eq. (2.15) vanishes. A static magnetic moment operator means that the magnetization per unit volume is constant, which is a good approximation only at low temperatures with respect to T_C. Furthermore, we also assume that the Hamiltonian can be represented *only* by a Zeeman term of the form

$$\mathcal{H}_Z = -\frac{\mu_B g}{\hbar}\,(\boldsymbol{l} + \boldsymbol{\sigma}) \cdot \mu_o \vec{H}_{\text{eff}} = -\mathcal{M} \cdot \mu_o \vec{H}_{\text{eff}}, \tag{2.16}$$

where the effective magnetic field, $\vec{H}_{\text{eff}}$, includes all the energy contributions of Eq. (2.1) and the exchange coupling of Eq. (2.12), and we have included the g-factor to take into account the total angular momentum of a transition metal which is dependent on the $3d$ band population at the Fermi energy. This representation is extremely useful for an analytical and numerical treatment, as discussed below.

The remaining task is to evaluate the commutator of Eq. (2.15). Using the Zeeman Hamiltonian Eq. (2.16) and recalling the commutator relations of the total angular momentum, we obtain

$$\langle [\mathcal{M}, \mathcal{H}_Z] \rangle = -\Big\langle \Big[\mathcal{M}, \mathcal{M} \cdot \mu_o \vec{H}_{\text{eff}}\Big] \Big\rangle = -i\hbar\gamma \langle \mathcal{M} \times \mu_o \vec{H}_{\text{eff}} \rangle, \tag{2.17}$$

where we define the gyromagnetic ratio $\gamma = \mu_B g/\hbar$. Finally, by simple averaging over a unit volume, we use the relation of Eq. (2.11) to obtain the Landau-Lifshitz (LL) equation

$$\frac{d\vec{M}}{dt} = -\gamma \vec{M} \times \mu_o \vec{H}_{\text{eff}}. \tag{2.18}$$

The LL equation, as a semi-classical approximation, can be obtained by simpler means by considering the electron as a spinning top. However, the inclusion of all relevant terms in an effective field hides the underlying physics behind phenomenological parameters. A prime example is that the LL equation is purely conservative, eliminating the possibility of magnon scattering and thus thermodynamical convergence to a ground state.

2.4.2 Landau-Lifshitz-Gilbert equation

The Landau-Lifshitz equation as derived in the previous section is completely conservative, i.e., it is described by a Hamiltonian which preserves energy by definition. However, realistic materials dissipate energy by processes only described by non-conservative terms. Such processes involve direct energy loss due to lattice vibrations (phonons) and conduction electrons, and indirect energy loss via magnon scattering that eventually transmits energy to the lattice by means of spin-orbit coupling [128]. In order to include these effects while maintaining a semi-classical approach, a phenomenological term was proposed by Gilbert [52] as an additional viscous force. The so-called Landau-Lifshitz-Gilbert (LLG) equation takes the form

$$\frac{d\vec{M}}{dt} = -\gamma \vec{M} \times \mu_o \vec{H}_{\text{eff}} + \alpha_G \vec{M} \times \frac{d\vec{M}}{dt}, \tag{2.19}$$

where α_G is the Gilbert damping dimensionless coefficient. Consequently, when $\vec{M} \times \mu_o \vec{H} \neq 0$, Eq. (2.19) predicts that $\vec{M}$ converges to $\vec{H}$ in a spiraling motion i.e., the magnetization eventually relaxes to a direction parallel to the field.

A numerically useful form of the LLG equation is the *normalized* version, where the magnetization is expressed in terms of a unit vector $\hat{m}$. The normalization is achieved by dividing the LLG equation by the modulus of the magnetization vector, or saturation magnetization $M_s = |\vec{M}|$. An additional simplification is found by cross multiplying Eq. (2.19) by $\vec{M}$. By cross products properties and $\hat{m} \times \hat{m} \times d\hat{m}/dt = -d\hat{m}/dt$, one can cast the normalized LLG equation as

$$\frac{d\hat{m}}{dt} = -\frac{1}{1+\alpha_G^2}\gamma \hat{m} \times \mu_o \vec{H}_{\text{eff}} + \frac{\alpha_G}{1+\alpha_G^2}\hat{m} \times \hat{m} \times \mu_o \vec{H}_{\text{eff}}, \tag{2.20}$$

This form of the LLG equation is a simple ordinary differential equation (ODE) that can be easily solved by many numerical algorithms.

The Gilbert approach has been very successful in describing the effective damping of magnetic materials and it is a standard characterization procedure performed e.g. in FMR measurements. For this reason, we will assume it is a valid model for the materials used in this thesis.

2.4.3 The effective field

In the derivation of the LL equation, Eq. (2.18), it was assumed that the different contributions to the Dirac Hamiltonian Eq. (2.1) could be mapped

as magnetic fields. Here, we describe each of the relevant terms in such an effective field:

- **Zeeman**: The true Zeeman component is only due to an external field. We shall denote such a field as $\vec{H}_a$.
- **Shape anisotropy**: This contribution is important for real samples with physical boundaries and thus depends on the actual shape of the material. Such boundaries must obey Maxwell's equations, in particular $\nabla \cdot \vec{B} = \nabla \cdot (\vec{H}_{\text{eff}} + \vec{M}) = 0$. In this context, the net flux at the magnet's boundary must be zero precluding the existence of monopoles. In this thesis, the relevant geometry is the thin film approximation, where the lateral boundaries can be assumed to be infinitely far. Consequently, we shall use the equivalent demagnetizing field

$$\vec{H}_d = -\vec{M} \cdot \hat{z}, \tag{2.21}$$

  following the convention that the $\hat{z}$ coordinate is the out-of-plane direction.
- **Magnetocrystalline anisotropy**: As discussed before, this effect is closely related to the spin-orbit coupling between the magnetic system and the crystal lattice. In this thesis, we will be interested only in the uniaxial anisotropy [51, 124] expressed as

$$\vec{H}_K = \frac{2K_U}{M_s}, \tag{2.22}$$

  where K_U is the magnetic anisotropy energy per unit volume. This term is uniaxial in the sense that the direction of $\vec{H}_K$ defines a preferential or easy axis for the magnetization orientation. This term is particularly important in materials with high PMA, in which case $\vec{H}_K \parallel \hat{z}$, as discussed before.
- **Exchange**: The Heisenberg exchange Hamiltonian can be mapped into an effective field by considering the interaction to take place between nearest neighbors, by virtue of the localization of the $3d$ electrons. For non-collinear neighboring moments, it can be written as a function of the Laplacian operator ∇^2 [117, 124]

$$\vec{H}_{ex} = \lambda_{ex}^2 \nabla^2 \vec{M}, \tag{2.23}$$

  where $\lambda_{ex} = \sqrt{2A/\mu_o M_s^2}$ is the so-called exchange length as a function of the exchange stiffness $A = 2\mathcal{J}s^2/a_s$ expressed as a function of the Heisenberg Hamiltonian exchange constant $\mathcal{J}$, the relative direction of the neighboring spins s, and the atomic lattice spacing a_s.
- **Thermal field**: Temperature plays a fundamental role in the excitation of magnetic dynamics. One can understand the action of temperature as to randomly tilt a magnetic moment which eventually propagates as a spin wave due to exchange coupling, as discussed in section 2.2.4. These *thermal magnons* are intrinsically related to the ferromagnetic ordering loss as a function of temperature. As discussed later, thermal magnons also contain energy needed to excite STT-induced magnetic solitonic

modes. In the semi-classical approximation, temperature is included as a Gaussian random field in the three spatial coordinates by appropriately scaling its magnitude to satisfy the fluctuation - dissipation theorem [19]. The magnitude of such a time-dependent random field can be expressed by its second moment [139, 35]

$$\langle \vec{h}_T(t)\vec{h}_T(t')\rangle = \frac{2\alpha_G k_B T}{\gamma\mu_o^2 M_s V_s}\delta(t-t'), \tag{2.24}$$

where $\delta(t)$ is the Dirac delta function.

2.4.4 Magnetic domains and domain walls

The ground state of a macroscopic magnetic material is found from the balance between the components of the effective field when $\vec{H}_a = 0$. As is the case for any ground state, energy minimization dictates its convergence. For a magnetic system, the energy is given by Eq. (2.7) and it is thus limited by M_s which was assumed constant in the LL approximation (section 2.4.1). However, the exchange term in the effective field suggests that a macroscopic material must be interpreted as a set of LLG equations smoothly coupled by the Laplacian. Minimization of such a system leads to the formation of ferromagnetic regions, or magnetic domains, whose directions *average* to zero.

The existence of magnetic domains is a direct consequence of the competition between anisotropies and exchange fields. Qualitatively, the anisotropy fields promote moments to be aligned with an axis or plane so that a vanishing magnetization is obtained by anti-parallel (or anti-ferromagnetic) ordering. In contrast, the exchange field aims to keep neighboring moments ferromagnetically ordered and so the transition between anti-parallel moments is favorable at an infinite length. From energy minimization, a balance between these competing energies is established and magnetic domains are separated by transition regions known as *domain walls*. For the materials of interest here, the domain wall size is on the order of 100 nm. An important consequence is that magnetic particles smaller than the domain wall size exhibit a single domain and the dynamics are largely coherent, as discussed by the macrospin model in section 3.1.

The type of domain walls established in the magnetic sample depends on its magnetic properties and physical dimension and shape [17]. Two relevant types of domain walls in this thesis are those separating anti-parallel domains in thin films [51]. Materials with low perpendicular anisotropy ($\vec{H}_K < \vec{H}_d$) tend to exhibit *Néel* walls, where the spins rotate in the (easy) plane [Fig. 2.9(a)]. On the other hand, materials with strong perpendicular anisotropy favor *Bloch* walls, where the spins rotate in the out-of-plane direction [Fig. 2.9(b)]. The size of these domain walls can be estimated by asymptotic methods. The Bloch wall width is given by $\Delta_B \approx \pi\sqrt{A/K_U}$ and it is generally smaller than the Néel wall whose width is given by $\Delta_N \approx \pi\sqrt{2A/K_U}$.

Additionally to the aforementioned domain walls, there is a magnetic texture in thin films shaped as disks for a given range of aspect ratios. Such a texture is known as a *vortex* [100, 42]. The vortex minimizes energy in thin films

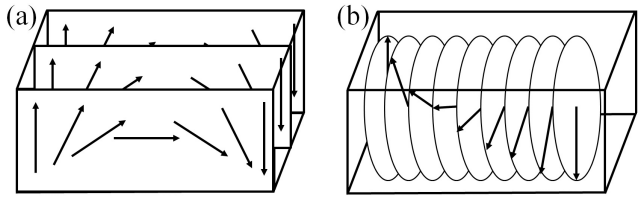

Figure 2.9: Schematic of (a) Néel and (b) Bloch domain walls emphasizing the rotation planes (Adapted from Ref. [51]).

with weak PMA by curling the in-plane magnetization around a nanoscopic, out-of-plane vortex core. This structure can be classified as a half-Skyrmion (discussed in section 2.6) and it is a remarkably stable ground state. In this thesis we will find vortex configurations only as an undesired ground state in micromagnetic simulations, discussed in chapter 3.

2.4.5 Ferromagnetic resonance

As discussed in section 2.4.2, the LLG equation predicts that the magnetization becomes parallel to the effective field after a finite time. For ferromagnetic thin films, the Zeeman and anisotropic contributions dominate the effective field and it is possible to *magnetize* the ferromagnet. In other words, the magnetic domains are destroyed and a macroscopic ferromagnetic ordering is achieved. The magnetized state represents the macroscopic manifestation of the ideal homogeneous ferromagnetic ordering expected from the band model of magnetism. As such, it provides a means to study the collective dynamics of spin waves.

The controlled excitation of spin waves is usually achieved experimentally by magnetizing the ferromagnet and subsequently applying a small alternating field. The relative orientations of these fields with respect to the sample shape excites different types of spin waves [124] whose details are beyond the scope of this thesis. However, it is important to understand the small amplitude collective excitation or ferromagnetic resonance (FMR).

Consider a thin film magnetized out-of-plane, so that the effective field can be approximated by $\vec{H}_{\text{eff}} = (\vec{H}_a - \vec{H}_d) \cdot \hat{z}$. Assuming that $\vec{M}$ is non-collinear with $\vec{H}_{\text{eff}}$, the LL equation predicts an oscillatory motion at a specific or eigen-frequency ω_o. Such an eigen-frequency thus represents the FMR frequency, that is, the collective and homogeneous (wave vector $\boldsymbol{k} = 0$) motion of exchange-coupled spins. Qualitatively, the FMR frequency indicates the cut-off for propagating spin waves with higher wave vector, similar to electromagnetic waves in waveguides. In other words, any excitation below the FMR frequency will have an evanescent character, experiencing a strong damping. On the other hand, excitations above the FMR frequency are allowed to propagate distances on the order of microns, limited by the spin wave dispersion of the material [79, 124]. Additionally, dipolar fields can dominate the spin wave dispersion at very short wave vectors leading to frequencies below FMR in

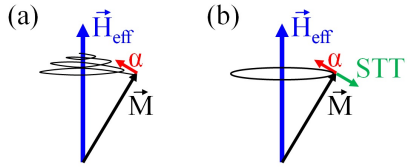

Figure 2.10: Schematic of the magnetization dynamics expected from the (a) LLG equation and (b) the LLGS equation with a suitable current polarity so that the STT opposes the damping.

such a regime [40, 64]. Such lower frequencies can be linked to the excitation of solitonic waves in magnetic materials.

2.4.6 Semi-classical spin transfer torque

The STT effect can be included in the semi-classical approximation as an additional term of the form given in Ref. [122]. In the case of a spin valve, where the electrons are polarized by a ferromagnetic layer, or polarizer, with normalized magnetization $\hat{p}$, the in-plane torque incident on $\hat{m}$ can be written as

$$\vec{\tau} = -\gamma\mu_o\sigma_o\epsilon\hat{m} \times \hat{m} \times \hat{p}, \tag{2.25}$$

where $\sigma_o = \hbar IP/\mu_o M_s|e|V_s$ is the spin torque coefficient, I is a charge current, P is the spin polarization, and $\epsilon = \lambda/[\lambda + 1 + (\lambda - 1)\hat{m} \cdot \hat{p}]$ is the spin torque asymmetry factor as a function of the spin asymmetry λ.

The torque of Eq. (2.25) can be argued to be a crude approximation of the more detailed theory described in section 2.3.4. However, it correctly describes the effect of the in-pane torque deposited in the ferromagnet, which can either oppose or enhance the Gilbert damping as a function of the current polarity. The action of the STT and damping is schematically shown in Fig. 2.10(a-b). In particular, the dynamics expected from the LLG equation follow a spiral trajectory until the magnetization aligns with the effective field [Fig. 2.10(a)]. On the other hand, STT can balance the damping and, in principle, the dynamics are given by the conservative LL equation. The simplicity of Eq. (2.25) makes it extremely useful for numerical and analytical studies. In the following, we will refer to the LLG equation expanded with the Slonczewski in-plane torque as the LLGS equation.

2.4.7 Single-mode Hamiltonian formalism

The LLGS equation can be directly used numerically in order to obtain a highly accurate description of experimental observations. However, a tractable analytical description is not generally achieved even in the simple case of a single LLGS equation, or a macrospin approximation discussed in chapter 3. A solution to this limitation was found in the Hamiltonian formalism proposed by Slavin and Tiberkevich [119, 117, 118]. The general idea of this

approach is to treat the Gilbert damping, STT, and external sources as perturbations while mapping the LL equation into a Hamilton equation of motion. By performing a Holstein-Primakoff transformation and further diagonalization following a Bogoliubov canonical transformation, the LLGS equation is approximately mapped into the non-linear auto-oscillator equation

$$\frac{dc}{dt} + i\omega(|c|^2)c + \left(\Gamma_+(|c|^2) - \Gamma_-(|c|^2)\right) c = 0, \tag{2.26}$$

where c is a complex amplitude describing the small-amplitude magnetization dynamics. Equation (2.26) has the simple interpretation that auto-oscillations are achieved above a threshold current, I_{th}, when the real terms cancel each other. In more detail, the terms of the auto-oscillator equations are:

- $\omega(|c|^2) = \omega_o + N|c|^2$ is the non-linear generation frequency, where ω_o is the FMR frequency, $N = 2\omega_M$ is a nonlinearity factor that couples frequency and power, and $\omega_M = \gamma\mu_o M_s$. This term explicitly shows that the generation frequency of a STO is coupled to its generated power $p = |c|^2$.
- $\Gamma_+ = \Gamma_G(1 + Q|c|^2)$ is the positive damping term, where $\Gamma_G = \alpha\omega_o$ is the Gilbert damping term and $Q = (\xi - 1)/(1 + |c|^2)$ is a non-linear proportionality factor related to the supercriticality $\xi = I_{dc}/I_{th}$ and I_{dc} is the applied dc bias current.
- $\Gamma_- = \xi\Gamma_G(1 - |c|^2)$ is the negative damping or STT term.

The advantage of the auto-oscillator equation lies in its relative simplicity while still capturing the strong nonlinearities of perturbed magnetic systems. Although simplistic, the auto-oscillator equation has been successful in the prediction of a wide variety of experimental observations including field angle and current dependencies [121, 50, 31, 13], modulation [101, 90, 30], injection locking [107, 103, 34], mutual locking [63, 55, 130], and generation linewidth [67, 69, 68]. We will mainly rely on the auto-oscillator framework to perform the analytical calculations in this thesis.

In the following chapters, it will be also customary to study strongly nonlinear dynamics by linearizing Eq. (2.26) about an operating point. In general terms, the complex amplitude is expanded as

$$c = \sqrt{p_o + 2\delta p} \cdot e^{-i\phi} \tag{2.27}$$

where $p_o = (\xi - 1)/(\xi + Q)$ is the free-running normalized power, $\delta p \ll p_o$ is a power perturbation, and ϕ is the instantaneous phase. In such linearized equations (derived for each case in the relevant section below), the dynamics are intimately related to the total restoration rate $\Gamma_p = \alpha_G\omega_o(\xi - 1)$ and the dimensionless nonlinearity coefficient $\nu = p_o N/\Gamma_p$.

2.5 Non-linear magnetization dynamics

The LLGS equation of motion and its mapping into the auto-oscillator equation admits a wealth of dynamical solutions depending on external factors and

intrinsic properties of the ferromagnet. In this section, we will review the relevant spin valve geometries explored in this thesis and the dynamical modes excited in them. From here on, the term non-linear will be exclusively used to denote the coupling between phase (or frequency) and power, in light of the non-linear parameter N of the auto-oscillator framework.

2.5.1 Spin torque oscillators

Magnetization dynamics induced by STT can only be achieved with relatively high current densities, on the order of $10^{12}\mathrm{A/m^2}$. A practical solution is to confine the electron flow through the spin valve in a nanoscopic region. To date, two main geometries have been proposed to this end:

- **Nanopillars**: the spin valve is physically etched down to a generally elliptical area [71], where the axes are on the order of 100 nm [Fig. 2.11(a)]. This kind of geometry ensures the flow of electrons through the structure (current perpendicular to plane or CPP) and maximizes the STT effect. However, the confinement introduces several modes that can either transition or mode-hop [70, 113, 74, 143, 88]. Nowadays, this geometry is mainly used for magnetic tunnel junctions (MTJs) [142, 37] where the current must be forced through an insulating spacer and the electronic transport gives rise to the so-called tunneling magnetoresistance [62].

- **Nanocontact (NC)**: the high current densities are achieved by patterning a metallic, nanosized contact of radius R_c on top of a physically extended spin valve [Fig. 2.11(b)]. In this case, the current is confined in the top of the structure but then spreads as it flows through the stack. In order to ensure an almost ideal CPP flow [95], a relatively thick bottom Cu layer is usually deposited on top of a very thick oxide buffer. However, it must be acknowledged that some of the electrons are spread in the Cu spacer due to its reduced resistance. These devices offer additional freedom for the generated dynamics and will be the main subject of study in this thesis. The relevant dynamics will be described in the following sections. We will refer to this geometry with the acronym NC-STO.

As illustrated in Fig. 2.11, we shall consider pseudo spin valves in this thesis. It is customary to denote the thinner layer as the "free" layer since it is primarily subjected to STT, whereas the thicker layer primarily spin-polarizes the electrons and is referred to as the "fixed" layer. Notably, both layers exert STT on each other as discussed in section 2.3.4. However, the large volume and M_s of the fixed layer makes it largely insensitive to STT and it is generally a good approximation to consider it truly static.

A novel geometry providing STT has been recently developed based on the spin Hall effect. Such devices are known as spin-Hall nano-oscillators (SHNOs) [39, 38, 76, 131] where the electron flow through a heavy metal e.g. Pt, generates a perpendicular spin current due to spin-orbit coupling. As described by the CRMT in section 2.3.4, spin currents are responsible for the STT effect. In order to achieve a significant spin current, the current is

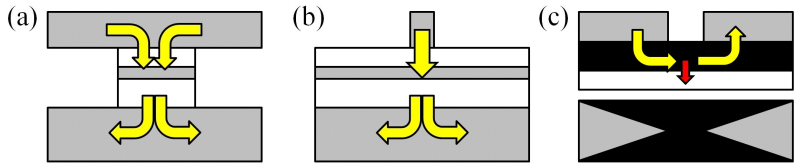

Figure 2.11: Schematic structure of (a) nanopillar and (b) nanocontact spin torque oscillator geometries based on pseudo spin valves. The magnetic (non-magnetic) layers are shown in white (gray) The yellow arrows describe the electron path through each structure. The alternative spin-Hall geometry is shown schematically in (c), both in a side and top view. The current flowing through the non-magnet (black) establishes a pure spin current (red arrow) due to spin-orbit coupling.

confined in SHNO by patterning Au "needles" on top of the Pt layer. Figure 2.11(c) shows both the lateral and top view schematics, where the spin current is represented by a red arrow and the Pt layer is colored in black. The main advantage of these devices is to provide optical access to the magnetic layer and thus determine the dynamics experimentally [39]. However, as mentioned before, in this thesis we will only study the magnetodynamics generated in pseudo spin valve based geometries.

2.5.2 Spin-wave propagating mode

The first mode derived for NC-STOs was predicted by Slonczewski [123] shortly after the STT effect was described. In this case, it is assumed that a soft free layer e.g., NiFe, is perpendicularly magnetized by a strong external field. At currents above threshold, magnetization dynamics are established below the NC. A first important observation is that such magnetization dynamics have a larger cone angle than FMR. Consequently, the internal field is higher in magnitude, leading to a generation frequency *above* FMR. It is noteworthy that the auto-oscillator framework predicts this effect from the positive value of the nonlinearity coefficient N [118].

A second key observation follows from the fact that the free layer is extended, and so the magnetization dynamics are coupled to the surrounding spins via exchange. Slonczewski [123] showed that the STT generated dynamics follow a Bessel function whereas they propagate radially away from the NC as a Hankel function [Fig. 2.12(a)]. This behavior was later observed experimentally [79] by means of an optical technique called micro-focused Brillouin light scattering (μ-BLS) where the photon - magnon interaction also provides information about the amplitude of the $\boldsymbol{k}$ vector of the propagating wave.

2.5.3 Solitonic bullet mode

In the previous section, we briefly mentioned that the auto-oscillator theory correctly predicted the generation frequency of the propagating mode due to the sign of the nonlinearity coefficient. However, when the external field is

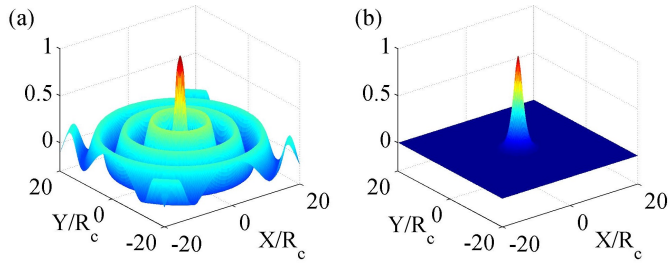

Figure 2.12: Spatial profiles for the (a) propagating and (b) solitonic bullet spin-wave modes. The spatial coordinates are normalized to R_c.

directed in-plane, the nonlinearity coefficient is negative. Slavin and Tiberkevich [121] studied this regime in detail. A negative nonlinearity coefficient leads to a generation frequency *below* FMR indicating the spatial localization of the mode. Indeed, the auto-oscillator equation can be cast in this case as a non-linear Schrödinger equation, which admits known solitonic solutions. Such dynamics have been recently observed with μ-BLS [40, 39] in modified NC-STO geometries.

The solitonic bullet mode can be visualized as an envelope for the magnetization dynamics [Fig. 2.12(b)] and comes about as the available energy of the system reaches a minimum. For this reason, the bullet mode has a lower current threshold than the propagating mode for the same conditions. Invoking the stabilization of the mode with minimal current density i.e., single mode generation [119, 106], this mode is expected to be dominant for an external field applied in-plane. However, numerical simulations failed to reproduce the bullet mode until it was acknowledged the importance of perturbations in the magnetic system. Indeed, Consolo *et al.* [31] showed that the bullet mode could be only reproduced by reducing the current from an already excited propagating mode. The numerical inclusion of temperature also facilitates this process by the creation of thermal magnons [28], although longer simulations are required.

2.5.4 Magnetic dissipative droplets

Magnon drops are localized modes that were theoretically predicted in conservative (dissipationless) materials exhibiting PMA. The magnons excited in such materials experience an attractive force that leads to a condensate [73, 72]. As discussed before, magnons are bosons so that Bose-Einstein statistics permit the formation of such a condensate. The magnon density eventually reaches a maximum where it becomes energetically favorable to reverse the magnetization, forming a family of solitonic objects called magnon drops [Fig. 2.13(a)].

In a real material with dissipation, STT offers a possibility to compensate the damping and hence attract thermal magnons. Such a mechanism was theoretically proposed by Hoefer *et al.* [58], where STT causes a modulational

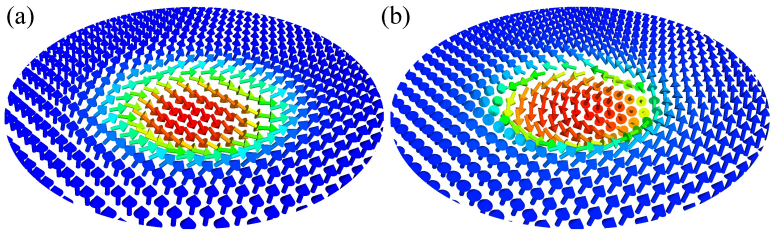

Figure 2.13: Profile of the (a) magnetic dissipative droplet and (b) Skyrmion. The arrow representation emphasizes on the different in-plane orientation (yellow shades) of the magnetization at the boundary between the perpendicular domains (red and blue).

instability i.e., the magnon density increases exponentially. The formation of such a solitonic object receives the general term of magnetic dissipative droplet. In the following, we will refer to them simply as droplets. The STT - damping balance ensures that a particular droplet solution is stabilized from the available family of magnon drops, thus defining its profile, frequency, and spatial extent. The detailed derivation of the parameter interdependence can be found in Ref. [58].

Droplets were first observed experimentally by Mohseni *et al.* [84] in NC-STOs as a sharp frequency drop in the current and field dependent spectra, accompanied by a dramatic increase of resistance. The experimental evidence supported the theoretical predictions in which:

- The increase of resistance indicates the magnetization reversal below the nanocontact and thus the nucleation of a droplet.
- The current tunability is negligible as the critical magnon density is already reached.
- The dramatic increase of the RF power indicates that the dynamics occur at the boundary of the droplet. Such large amplitude magnetization dynamics maximizes the GMR in the current-probed region.
- Self-modulation was observed as a consequence of the combined action of drift instability [58] caused by the in-plane component of the external field, and the restoring force of the STT on the droplet [15].

The experimental observation of droplets opened up the possibility of studying magnon condensation and large-amplitude dynamics and corroborate some of the theoretically and numerically predicted effects such as field controlled motion [59], modulation [15], and interactions [80]. Notably, the nucleation mechanism of the droplets preclude its analytical treatment from the LLGS equation, except for the modulational instability conditions. For this reason, the auto-oscillator framework is not directly applicable to study droplets and instead numerical simulations are required.

2.6 Topology and Skyrmions

The magnetic states described in this chapter can be mathematically classified within the concept of topology [18]. By means of topology, one is able to distinguish different magnetization states and group them according to certain properties. An important prediction is that a threshold energy is required to transition between magnetic states belonging to different topological groups. In simple terms, a topological group is established by any continuous deformation of the magnetization texture. For example, local Zeeman energy can create spin waves as a continuous deformation of an homogeneously magnetized thin nanowire and thus conserve the topological group. However, a larger Zeeman energy can change the topological group by forming a domain wall and preclude the relaxation to a homogeneous state. Following the same logic, only a large Zeeman energy will be able to destroy the domain wall and recover the homogeneous state.

Topology can be described quantitatively by a number or topological invariant. In recent years, it has become customary in magnetism to use the Skyrmion number [86, 18], $\mathcal{N}$, as a topological invariant for two-dimensional thin films. It is defined as

$$\mathcal{N} = \frac{1}{4\pi} \int \int \mathrm{d}x\mathrm{d}y (\partial_y \hat{m} \times \partial_x \hat{m}) \cdot \hat{m}, \tag{2.28}$$

where both partial derivatives and the integration are performed in the plane. Qualitatively, Eq. (2.28) counts how many times the unit sphere is completely filled by the total magnetization. From this point of view, a homogeneously magnetized state corresponds to the group where $\mathcal{N} = 0$ and it is referred to as the topologically trivial group. The magnetization dynamics described in section 2.5 belong to this group implying that, as observed experimentally, the magnetization relaxes to its original state when it is not excited by STT.

Recently, it has been possible to numerically [46, 111] and experimentally [87, 141, 110] create magnetization states belonging to the $\mathcal{N} = 1$ group, or Skyrmions. These structures e.g., Fig. 2.13(b), can be excited in materials with helical ordering or when the so-called Dzyaloshinskii-Moriya Interaction (DMI) [45, 85] becomes relevant. To date, such materials are usually thin non-centrosymmetric magnets [91, 141, 140] and ultra-thin ferromagnetic layers grown on top of materials with very high spin-orbit coupling, usually heavy metals [110, 111]. In this thesis we shall not consider such materials and interactions, however the concept of topology is important in order to understand the nature of the studied magnetic dynamics, particularly in chapter 6.

3

Methods

3.1 Macrospin simulations

The so-called macrospin approximation is based on a nanostructure whose size is below the minimum magnetic domain wall size. In such a scenario, it is not energetically favorable to create domains and thus the nanostructure behaves as a single macroscopic magnet or macrospin. Consequently, this approximation is strictly valid only for nanopillar STOs of diameter below 100 nm [9]. However, as the auto-oscillator framework is a mapping of the LLGS equation, macrospin simulations can also be used, in some cases, as relatively simple numerical tests for such a framework.

Numerically, a macrospin simulation consists of solving a single LLGS equation, neglecting exchange. The simplest way to solve the LLGS equation is to map it into spherical coordinates $(\rho_S, \phi_S, \theta_S)$, where $\rho_S = |\hat{m}| = 1$. Consequently, the LLGS equation is decomposed into a system of two coupled equations [139, 145, 61]

$$\begin{aligned}
\frac{d\theta_S}{dt}\frac{1+\alpha_G^2}{\gamma} &= |\vec{h}|\left(\alpha_G\frac{dH_R}{d\theta_S}+\frac{1}{\sin\theta_S}\frac{dH_R}{d\phi_S}\right) \\
&\quad -\alpha_J\left(\frac{dP_R}{d\theta_S}-\frac{\alpha_G}{\sin\theta_S}\frac{dP_R}{d\phi_S}\right) \\
&\quad -(\alpha_G D_1+D_2)\sin\theta_S, \qquad (3.1a)\\
\frac{d\phi_S}{dt}\frac{1+\alpha_G^2}{\gamma} &= \frac{|\vec{h}|}{\sin\theta_S}\left(\frac{dH_R}{d\theta_S}-\alpha_G\frac{1}{\sin\theta_S}\frac{dH_R}{d\phi_S}\right) \\
&\quad -\frac{\alpha_J}{\sin\theta_S}\left(\alpha_G\frac{dP_R}{d\theta_S}+\frac{1}{\sin\theta_S}\frac{dP_R}{d\phi_S}\right) \\
&\quad +D_1-\alpha_G D_2. \qquad (3.1b)
\end{aligned}$$

where $H_R = \hat{m}\cdot\vec{h}$, $P_R = \hat{m}\cdot\hat{p}$, $\vec{h} = \vec{H}_a/M_s$, $D_1 = D_x\cos\theta_S\cos^2\phi_S + D_y\cos\theta_S\sin^2\phi_S - D_z\cos\theta_S$, $D_2 = \cos\phi_S\sin\phi_S(D_y - D_z)$, and D_x, D_y and D_z are the normalized demagnetizing fields calculated for elliptically shaped nanopillar cross sections [92]. A noteworthy point is that for a circular pillar, such elliptical integrals diverge and the thin film approximation for $\vec{H}_d$ is

a good approximation. Furthermore, the thermal field can be also included, converting the problem into a stochastic differential equation (SDE) [35].

In order to solve such coupled SDEs, a high order integration method is required. In this thesis, we use the approach by Milshtein [82] that extends the first order Euler algorithm to account for a random field. A critical benefit of this approach, is that the same algorithm reduces to a simple Euler integration method when temperature is not included. However, the choice of the time step is also critical for a correct description of the dynamics.

3.2 Micromagnetic simulations

The micromagnetic approximation is one of the best numerical methods to study the dynamics of magnetic materials. In contrast to macrospin, the micromagnetic approximation aims to solve a set of LLGS equations coupled by the exchange interaction. Consequently, this technique can be illustrated as a coupled array of macrospins or cells [Fig. 3.1], whose individual size is below the exchange length, λ_{ex}. Furthermore, micromagnetic simulations are ideal to study spin waves and magnetic domains, as discussed in Ref. [60].

In the micromagnetic approximation, every cell has a well-defined spatial location corresponding to the real structure. These kind of problems can be approached either by finite difference (FD) or finite elements (FE). In FD, the cells are usually cubic so that every cell is equidistant, as in Fig. 3.1. In FE, however, the cells are tetrahedra with generally different distances from one another. In this work, we will mainly use FD approach, particularly the open-source code Mumax2 [136]. The shape limitations imposed by the cubic cells are overcome by the massive parallelization of graphic processing units (GPUs) that allows one to solve very large problems in a short time. The simulation results presented in this thesis were performed on NVIDIA's GTX 580 (512 cores) and GTX 690 (2 x 1536 cores) architectures.

Micromagnetic simulations are of fundamental importance in the NC-STO modeling. However, the simulation of a realistic device is not possible since its size limits the maximum allocatable cells in commercial GPUs or makes the simulation time extremely long. For this reason, NC-STO simulations are performed by approximating the extended free layer by a disk with a diameter of 1 to 1.5 μm, well below the physical dimension of the samples but large enough to capture the relevant magnetodynamics. There are two detrimental

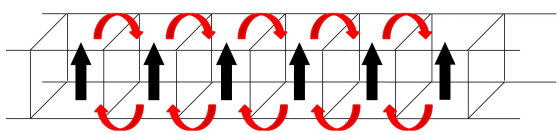

Figure 3.1: Schematic of the micromagnetic simulations, where a large array of macrospin cells (cubes) with a well-defined magnetization (black arrow) are coupled by exchange (red arrows). The size of the cells must not exceed λ_{ex} for each coordinate.

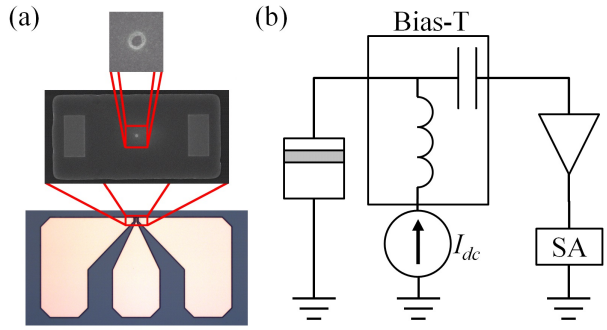

Figure 3.2: (a) Scanning electron microscopy (SEM) pictures of the fabricated NC-STOs showing, from top to bottom, a $\sim$ 100 nm NC, the NC-STO layout with two ground contacts at the sides, and the collinear waveguide pads [SEM pictures courtesy of P. Dürrenfeld] (b) The STOs are characterized electrically by a dc current and subsequent amplification and spectral measurement of the generated ac signal. A bias-T is regularly used to filter the dc and ac components relevant for each section of the circuit.

consequences of this approximated geometry that must be taken into account in order to obtain physically realistic results:

- The aspect ratio of the disk promotes a vortex as the magnetic ground state due to its shape anisotropy [51]. To prevent the formation of a vortex state, the magnetization is always initialized along its hard direction and then relaxed to equilibrium in the presence of an external magnetic field and an artificially large Gilbert damping to improve convergence.

- Creation and reflection of spin waves is possible at the boundaries of the simulation area after the relaxation has been achieved i.e., when the Gilbert damping term is restored to a physically realistic value. A known solution has been the use of absorbing boundary conditions [8, 29] where the artificially large Gilbert damping is conserved close to the simulation boundary. In this thesis, we implement a linear increase of the damping up to a factor $100\alpha_G \approx 1$.

3.3 Electrical characterization

The NC-STOs are electrically characterized in order to probe the magnetization dynamics. This approach is based on the assumption that the fixed layer is mostly static, and the precession of the free layer can be simply probed by GMR. The NC-STO devices used here have the structure Co(8 nm)/Cu(8 nm)/NiFe(4.5 nm), where the NiFe is the free layer. The spin valve is patterned into a rectangular mesa that is 8 μm $\times$ 16 μm in size. Cu NCs of different sizes and two ground contacts are lithographically patterned on top of the free layer of each device. The whole structure is then contacted by gold

pads shaped as coplanar waveguides [Fig. 3.1(a)] in order to provide means to probe the generated ac voltage.

The devices are characterized in a probe station, utilizing a non-magnetic probe. An external field is set by rotatable Halbach arrays of permanent magnets creating fixed fields of 0.9 T and 0.965 T. In order to characterize the dynamics, the RF circuit of Fig. 3.2(b) is used. The dc current source is a Kethley 6221 dc and ac current source while the voltage is sensed by a Kethley 2182A nanovoltmeter. The STO-generated ac wave is then separated utilizing a bias-T of bandwidth 500 MHz to 40 GHz, and studied in the frequency domain by a R&S FSV40 spectrum analyzer (SA).

This characterization technique suffers from impedance mismatch between the RF environment (50 Ω) and the NC-STO ($\sim$ 10 Ω). Consequently, the dc current is not fully delivered to the STO leading to markedly different current tunabilities due to the impedance sample-to-sample variation. As mentioned in chapter 1, the power generated by STOs is low and microwave amplifiers are used to observe signals on the order of 10 to 20 dBm above the SA noise floor. From the measured spectra, one strives to obtain a good estimate of the frequency of the excited dynamics and its linewidth. Throughout this thesis, linewidth will refer to the full width at half maximum, which is generally in the order of MHz for STOs. In order to quantify these parameters from the experimental spectrum, a fitting procedure was developed in MATLAB including multiple Lorentzian fits, minimum-error procedures to find the best fit, subsequent removal of bad fits, and similarity-based grouping.

4

External perturbations

The STT-induced dynamics in STOs can be subjected to perturbations from the environment. Of particular technological interest are pure tones which, depending on their frequency, can induce synchronization or modulation. Owing to their strong nonlinearity, STOs exhibit novel responses to these perturbations, leading to fundamental considerations to be taken in the design of any realistic device. In this chapter, we study the synchronization and modulation phenomena analytically, by means of the auto-oscillator framework, and numerically utilizing the simplified macrospin approximation.

4.1 Synchronization

One of the most remarkable features of auto-oscillators is their ability to adjust to an external source of a similar frequency, or *synchronize*. It is possible to discern between two cases of synchronization:

- Injection locking occurs when the oscillator is subjected to or *entrained* by an external perturbation i.e., the coupling is unidirectional. A classical example is the use of low-linewidth quartz oscillators to synchronize more powerful but broad-linewidth positive-feedback circuits [114].

- Mutual synchronization occurs when both the oscillator and the external perturbation influence each other i.e., the coupling is bidirectional. An example is the synchronization of an ensemble of oscillators such as fireflies [97].

Injection locking [107, 49, 75, 132, 44, 103] has been experimentally observed in various STO geometries including nanopillars, MTJs, and NC-STOs. In contrast, mutual synchronization [63, 81, 102, 112] has been only observed in NC-STOs where the perturbation or coupling mechanism is provided by the propagating spin wave mode [102]. In both cases, the technological impact of the synchronization phenomena is the increase of the STO's generated power, approaching the minimum requirements of state-of-the-art electronic circuitry.

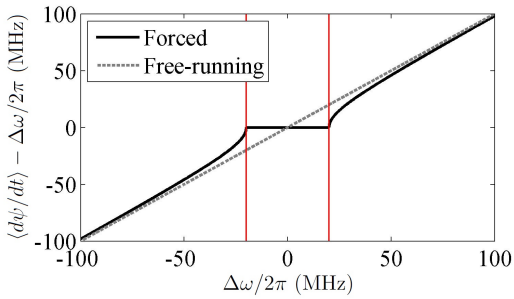

Figure 4.1: Relative oscillation frequency according to Adler's equation as a function of frequency mismatch. As the frequency mismatch approaches the value of F (red lines), the frequency converges towards the external frequency. In the range $\Delta\omega < |F|$ the oscillator is phase-locked and its relative frequency is identical to the external source.

4.1.1 Adlerian synchronization

The analytical formulation for synchronization was first introduced by Adler [2] for linear electronic oscillators. By solving the general resonant RLC circuit with an energy source, it is possible to obtain the ODE

$$\frac{d\psi}{dt} = -\Delta\omega - F\sin\psi, \tag{4.1}$$

where ψ and $\Delta\omega$ are, respectively, the phase difference and frequency mismatch between the oscillator and the source, while F is a coupling factor related to the oscillator's quality factor. Equation (4.1) is linear from the point of view that the only variable is the phase difference ψ. Adler's equation predicts synchronization when a steady state is obtained. This is possible if $F > \Delta\omega$ in which case the so-called phase-locked regime is established [Fig. 4.1]. Furthermore, Adler's equation predicts a monotonic approach to the phase-locked regime whose synchronization time is inversely proportional to F i.e., it is a purely over-damped system.

This approach was used to explain initial experimental observations [107, 49, 132] as well as to provide analytical insight into the STO synchronization [120, 117]. In particular, it was analytically [117] and numerically [94, 146] predicted that the strong nonlinearity of STOs would lead to an enhanced synchronization range, or phase locking bandwidth $\Delta\omega_o$, and a hysteretic injection locking behavior [115, 14]. However, there was a clear discrepancy between the predictions and the experiments. In particular, the pioneering simulations [55, 130] and predictions [48] of mutual synchronization of nanopillar STOs by means of a feedback circuits were never accomplished experimentally.

4.1.2 Non-Adlerian injection locking

The analysis of the transient dynamics in the synchronization process [147, 33, 34] uncovered that the STO would approach the phase-locked state in an

underdamped or non-Adlerian fashion. Such a behavior is possible in STOs due to the strong power and phase coupling that leads to an effective second order ODE. In terms of the auto-oscillator framework, an underdamped response implies the following:

1. Both the power and the phase difference transients are described by the same slow-time dynamics.

2. There is a minimum synchronization time parameterized by the time constant $\tau_s = \Gamma_p^{-1}$ originating from the real part of the transient response.

3. An intrinsic "ringing" frequency $\Omega = \Gamma_p\sqrt{F/F_{cr} - 1}$ is excited, where F_{cr} is a critical coupling factor required for non-Adlerian dynamics. This frequency originates from the imaginary part of the transient response.

4.1.3 Non-Adlerian mutual synchronization

The non-Adlerian dynamics of STOs provides new insights to study the mutual synchronization of electrically connected nanopillars as well as to understand its limitations. In particular, in this section we study serially connected STOs whose coupling signal comes from a passive, yet resonant, inductor (L) and capacitor (C) feedback circuit [Fig. 4.2]. Similarly to Ref. [130], the resonant (bandpass) feedback circuit provides both a self-consistent ac coupling signal or mean field in the Kuramoto limit [97] and an additional phase that can be tuned to lag or delay the coupling signal. In the auto-oscillator framework, section 2.4.7, the general equation can be written as

$$\frac{dc}{dt} + i\omega(|c|^2)c + \Gamma_+(|c|^2)c - \Gamma_-(|c|^2)c = \mathcal{F}_f(t, \sum c_i), \tag{4.2}$$

where $\mathcal{F}_f$ is a feedback function of time and the sum of each STO complex amplitude. As briefly mentioned earlier, the feedback circuit is resonant and thus adds a phase β to the coupling signal. Notably, due to Kirchoff Laws [114], such a simple feedback circuit has a $\beta = 180$ deg delay at resonance, $\omega(|c|^2) = 1/\sqrt{LC}$. Consequently, even in the simple case of a resistive feedback [55], the STOs will be subjected to a mean field that is delayed by 180 deg. We shall discuss which are the implications of the delay β. In the simplified case of two STOs connected in series we can write

$$\mathcal{F}_f(t, \sum c_i) = f\left(|c_2|e^{-i\phi_2(t)} + |c_1|e^{-i\phi_1(t)}\right)e^{i\beta}, \tag{4.3}$$

where f is the normalized coupling strength and we explicitly write the complex amplitude in its phasor form. The coupling strength for an electrically perturbed STO was derived in Ref. [118] and here we extend it to the general case of N_o serially connected STOs

$$f \cdot c_t = \frac{\xi\alpha_G\omega_o \tan\gamma_o}{2\sqrt{2}}\frac{\mu_{inj}}{N_o}. \tag{4.4}$$

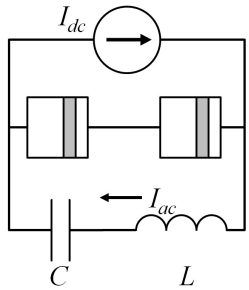

Figure 4.2: Resonant feedback circuit where an ac, I_{ac}, is established by the impedance of the capacitor (C) and inductor (L). From this definition, the injection current on the STOs has a delay $\beta = 180$ deg at perfect resonance.

where $c_t = |c_1| + |c_2|$, γ_o is the relative phase between the free and fixed layer, and $\mu_{inj} = I_{ac}/I_{dc}$ is the injection locking strength providing a dimensionless measure of the ac perturbation with respect to the dc bias. Equation (4.4) bounds the magnitude of f as $N_o \to \infty$ so that the total coupling vanishes at the thermodynamical limit.

As discussed in section 2.4.7, we study the perturbed dynamics of the auto-oscillator equation. Assuming similar STOs, $|c_1| \approx |c_2|$, we obtain the power and phase equations

$$\frac{d\psi}{dt} = \Delta\omega + 2\nu\Gamma_p\Delta p - 2f\cos\beta\sin\psi, \tag{4.5a}$$

$$\frac{d\Delta p}{dt} = -2\Gamma_p\Delta p - 2f\sin\beta\sin\psi, \tag{4.5b}$$

where $\psi = \phi_2 - \phi_1$ and $\Delta p = \delta p_2 - \delta p_1$. It can be verified that a linear oscillator, $\nu = 0$, reduces Eq. (4.5a) to an Adlerian ODE. However, when $\nu \neq 0$, the system of Eq. (4.5) contains trigonometric functions so that an exact solution cannot be obtained. Consequently, we linearize the equations about the steady phase and power differences

$$\psi_o = \arcsin\frac{\Delta\omega}{\Delta\omega_o}, \tag{4.6a}$$

$$\Delta p_o = \frac{f\sin\beta}{\Gamma_p}\frac{\Delta\omega}{\Delta\omega_o}, \tag{4.6b}$$

obtained directly from Eq. (4.5), where $\Delta\omega_o = 2\tilde{f}|\cos(\beta - \arctan\nu)|$ and $\tilde{f} = f\sqrt{1+\nu^2}$. The linearized system of equations reads

$$\frac{d\psi}{dt} = 2\nu\Gamma_p\Delta p - 2f\cos\beta\cos\psi_o\psi, \tag{4.7a}$$

$$\frac{d\Delta p}{dt} = -2\Gamma_p\Delta p - 2f\sin\beta\cos\psi_o\psi, \tag{4.7b}$$

which can be easily solved by linear algebra, leading to the characteristic

exponent

$$\lambda_c = -\left(\Gamma_\tau\right) \pm \sqrt{\left(\Gamma_\tau\right)^2 - 4\Gamma_p \tilde{f} \cos\psi_o \cos(\beta - \arctan(\nu))}, \tag{4.8}$$

where $\Gamma_\tau = \Gamma_p + f\cos\beta\cos\psi_o$.

Equation (4.8) reveals that serially connected STOs can also exhibit an underdamped response when λ_c becomes imaginary. Interestingly, and in contrast to the non-Adlerian injection locking, this system can also exhibit instability if Γ_τ becomes negative. Both features can be expressed as

$$f_{\text{ring}} \geq \frac{\sqrt{\Gamma_p^2 + 4\Delta\omega^2}}{4\nu\cos(\beta - \arctan\nu)}, \tag{4.9a}$$

$$\tau_s^{-1} = \Gamma_p + f\cos\beta\cos\psi_o. \tag{4.9b}$$

From the conditions of Eq. (4.9), it is possible to uncover important qualitative information that is lost in a steady state analysis:

1. Satisfying the condition of Eq. (4.9a) leads to a non-Adlerian approach to synchronization and hence establishes the minimum time constant of Eq. (4.9b). In contrast to injection locking, β has a critical influence on τ_s. Indeed, the time constant is reduced by keeping the phase delay in the range $\beta \leq |90|$ deg and its minimum value occurs at $\beta = 0$ deg.

2. In the range $\beta > |90|$ deg, the transient becomes slower and even unstable if the sign of τ_s changes, i.e., if the ratio $\Gamma_p / f\cos\beta\cos\psi_o < 1$. Noticing from Eq. (4.4) that f is proportional to $\xi/c_t \propto \xi/\sqrt{\xi - 1}$ and thus a decreasing function of ξ, the instability can be avoided by strongly biasing the STO at the price of losing coupling strength.

3. The condition for non-Adlerian solutions [Eq. (4.9a)] has a minimum value at $\beta = \arctan\nu \approx 90$ deg whereas it tends to infinity at $\beta = 0$ deg. In the serial circuit considered here, the operation regime lies in the range $\beta > |90|$ deg so that the optimal operation point to both reduce the time constant and avoid instability is found at $\beta \to 90$ deg.

4.1.4 Unstable dynamics

The analytical predictions of the previous section can be numerically tested by means of macrospin simulations. We assume a circular nanopillar with parameters for the free layer $\mu_0 M_s = 0.8$ T, $V_s \approx 3.7 \times 10^3$ nm^3, $P = 0.35$, and $\lambda = 1$. A high field $\mu_o \vec{H}_a = 1.5$ T is applied out-of-plane leading to the fixed layer tilt angle $\gamma_o \approx 60$ deg from the surface normal. Under these conditions, auto-oscillations are found above $I_{th} = 2.82$ mA.

The magnitude and phase of the coupling current are obtained from Kirchoff Laws. To proceed, we assume that the STOs have parallel and antiparallel resistances $R_0 = 10\ \Omega$ and $R_\pi = 11\ \Omega$, respectively, and the angular dependence is defined as $R = ((R_0 + R_\pi) - (R_\pi - R_0)\hat{m}\cdot\hat{p})/2$. The resonator is then

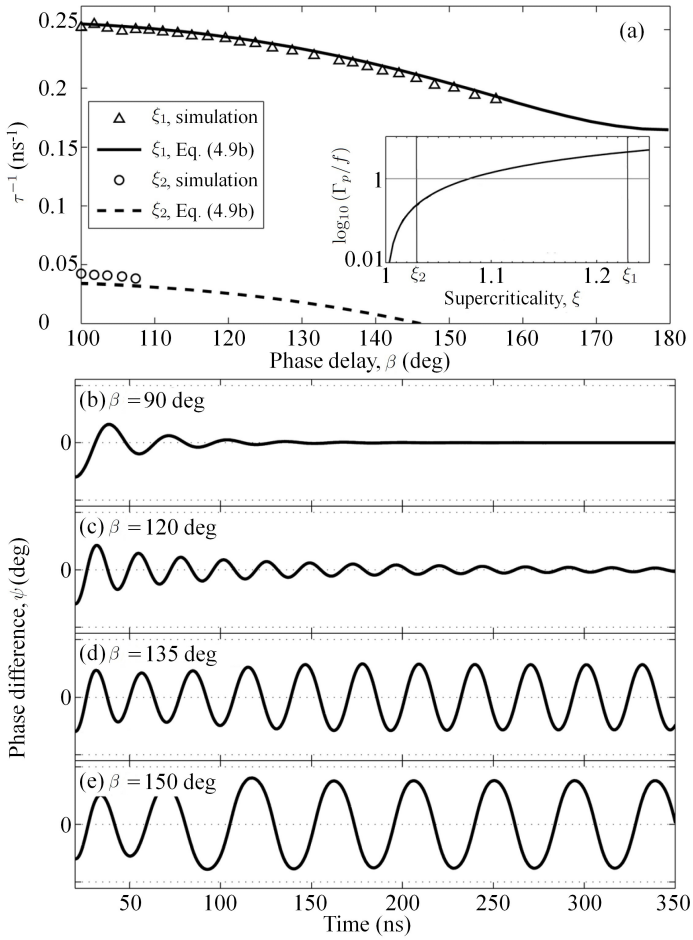

Figure 4.3: (a) Inverse minimum synchronization time, τ^{-1}, as a function of β determined from macrospin simulations. The synchronization dynamics are stable for ξ_1 (triangles) while instability is possible for ξ_2 (circles). The analytical estimates for both cases are shown by solid and dashed lines. Inset: ratio Γ_p/f as a function of ξ in common logarithmic scale when $\mu_o\vec{H}_a = 1.5$ T. Time trace of ψ as it evolves from stable (b-c) to unstable (d-e) dynamics. The dashed lines mark $\psi = \pm 180$ deg.

tuned about the STO oscillation frequency, so that $L \approx 1$ nH and $C \approx 2$ pF. The exact values depend on the operation point and desired phase delay.

From the above parameters, it is possible to analytically estimate the limit for stable dynamics as a function of ξ. As shown in the inset of Fig. 4.3(a), the ratio $\Gamma_p/f = 1$ is achieved when $\xi \approx 1.08$. Consequently, we perform simulations at two representative supercriticalities for stable ($\xi_1 = 1.23$) and unstable ($\xi_2 = 1.03$) dynamics.

The transient responses of the phase difference ψ as a function of the delay

$100 < \beta \leq 180$ degrees are fitted with an exponentially decaying sinusoidal function from which τ_s can be obtained. An excellent agreement is shown in Fig. 4.3(a) between the simulated results, represented by symbols, and the analytical predictions, represented by solid lines, indicating that Eq. (4.9) correctly estimates the onset of phase instability.

It is important to notice that instability in this context predicts an exponential increase of ψ in the linearized system of Eq. (4.7). However, the nonlinearities of the full system bound the phase difference. It is instructive to observe such transitions directly in the time domain. Figure 4.3(b-e) shows the phase difference for selected values of β when the system is biased at ξ_2. The time constant clearly increases in panel (c) compared to panel (b), in agreement with Eq. (4.9b). Panel (d) shows the case when $\tau_s^{-1} \approx 0$ s^{-1} and, as a result, the coupled system stabilizes into an oscillatory regime. Such oscillations in ψ indicate that the STOs are continuously adjusting their frequencies while never attaining a steady state. Such dynamics can be related to the pulling regime [105] where oscillators are only locked for a fraction of time. When β is further increased into the unstable regime, panel (e) shows that the dynamics are still oscillatory as expected from the saturation effect of non-linear systems.

4.1.5 Sample variation effect

The versatility of macrospin simulation allows one to study the dynamics of nominally different STOs, where the approximation $c_1 \approx c_2$ used in the analytical derivation does not strictly hold. However, an important prediction can be made from Eq. (4.9). In particular, as the frequency mismatch increases due to device variability, Eq. (4.9a) approaches $\Delta\omega \leq 2\nu f_{ring} \sin\beta \approx \Delta\omega_o$ and only non-Adlerian synchronization takes place.

This situation is indeed observed in Fig. 4.4(a) for several values of the frequency mismatch obtained from nominally different STO cross sections biased at ξ_1. In this case, the pulling regime is clearly observed when $\Delta\omega/2\pi = 115$ MHz. Similarly, instability is observed when the oscillators are biased at ξ_2 and $\beta = 150$ deg, as illustrated in Fig. 4.4(b). Notably, the different intrinsic frequencies of the STOs lead to what seems to be a period doubling, as illustrated by the different periods $T_1 \approx 50$ ns and $T_2 \approx 41$ ns in the same figure.

4.2 Modulation

We now turn our attention to the interaction between a STO and an external source of a very low frequency, on the order of MHz. As shown in the pioneering paper of Pufall *et al.* [101], the current tunability of STOs provides a unique scenario in which the external source directly causes an instantaneous frequency variation. Such a frequency variation is known as frequency modulation (FM) [24] and is widely used for analog communication technologies. From this perspective, the STO offers the immediate advantage of a much

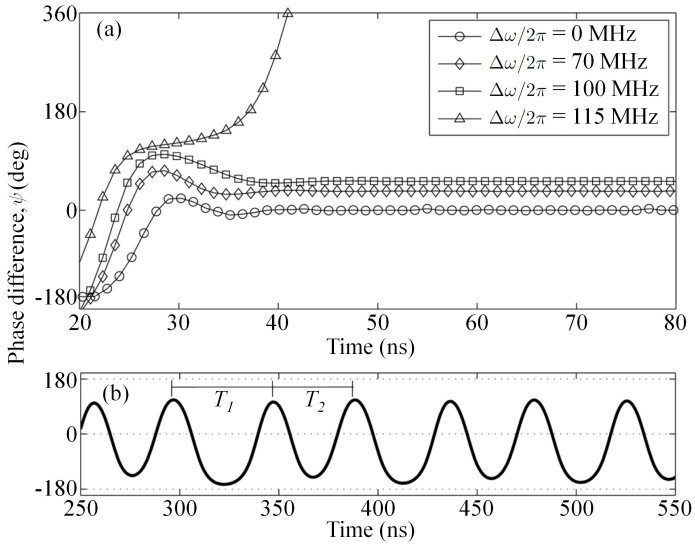

Figure 4.4: (a) Phase difference between STOs with several frequency mismatches. When $\Delta\omega = 115$ MHz, the STOs enter a pulling regime. (b) The finite value of $\Delta\omega$ leads to a period doubling in the phase difference with two clear periods: T_1 and T_2.

simpler circuit for generation and detection of frequency modulated spectra, in contrast to more complex super-heterodyne detection circuits.

The current tunability leading to the simple FM in STOs is a direct consequence of their nonlinearity. From the same argument, one would expect a similar power or amplitude modulation (AM). The combined action of the AM and FM was mathematically approached by Consolo *et al.* [30] and termed non-linear frequency and amplitude modulation (NFAM). Such a model was applied in the experimental NC-STO measurements performed by Muduli *et al.* [90] to fit intriguing observations such as the STO (carrier) frequency shift and asymmetric sideband power. However, the NFAM model was not related to the intrinsic STO parameters, for which reason it was not possible to understand the underlying physics.

4.2.1 Non-linear frequency and amplitude modulation

In order to physically understand the non-linear modulation of STOs, we analytically solve the auto-oscillator equation in the presence of a slow modulation current. The different time scales, on the order of 10^3 s, suggests that the modulation current can be accounted for in the bias component of the auto-oscillator framework, $\Gamma_-(I(t), |c|^2)$, reading

$$I(t) = I_{dc}\,(1 + \mu_m \cos \omega_m t)\,, \tag{4.10}$$

where μ_m is the modulation strength, and ω_m is the modulation frequency. Again linearizing the auto-oscillator equation according to the power fluctua-

tion approximation, the power and phase equations take the form

$$\frac{d\delta p}{dt} = \mu_m C_1 \cos\omega_m t + (\mu_m C_2 \cos\omega_m t - \Gamma_p)\, 2\delta p, \tag{4.11a}$$

$$\frac{d\phi}{dt} = \omega + 2\nu\Gamma_p \delta p, \tag{4.11b}$$

where we define the constants

$$C_1 = \Gamma_-(p_0), \tag{4.12a}$$

$$C_2 = \left(\Gamma_-(p_0) + \frac{d\Gamma_-(p)}{dp}\Big|_{p_0} p_0\right). \tag{4.12b}$$

The system of Eq. (4.11) is a coupled ODE with variable coefficients with the additional difficulty that such coefficients are not linear. Since we expect a periodic solution consistent with modulation, we propose a Fourier series with coefficients A_n and B_n as a trial solution:

$$\delta p = A_0 + \sum_{n=1}^{\infty} A_n \sin n\omega_m t + B_n \cos n\omega_m t. \tag{4.13}$$

Introducing Eq. (4.13) into Eq. (4.11) leads to an infinite system of equations. It can be shown [appendix A.1] that it is possible to truncate the series and obtain a recursive solution for the coefficients with good accuracy. After some algebraic manipulation, we obtain

$$\delta p = A_0 + \sum_{n=1}^{\infty} \sqrt{B_n^2 + A_n^2}\cos(n\omega_m t - \psi_n), \tag{4.14a}$$

$$\phi = (\omega + 2\nu\Gam_p A_0)t + \sum_{n=1}^{\infty} \frac{2\nu\Gamma_p}{n\omega_m}\sqrt{B_n^2 + A_n^2}\sin(n\omega_m t - \psi_n), \tag{4.14b}$$

The notation of Eq. (4.14) explicitly shows a harmonic-dependent phase $\psi_n = \arctan(A_n/B_n) = \arg(X_n)$, where X_n is a complex variable. To relate Eq. (4.14) to experimental observables, we compute its power spectral density (PSD). By Taylor expansion [appendix A.2], the PSD can be expressed as a series of convolutions

$$\begin{aligned} PSD = {} & p_0\delta_K(\omega + 2\nu\Gamma_p A_0) * \Big|\Big[(1+A_0)\delta_K(0) \\ & + \sum_{n=1}^{\infty}\frac{\bar{X}_n}{2}\delta_K(n\omega_m) + \frac{X_n}{2}\delta_K(-n\omega_m)\Big] \\ & * \prod_{n=1}^{\infty} J_0(\beta_n)\delta_K(0) + \sum_{j=1}^{\infty}\frac{J_j(\beta_n)}{|X_n|^j}(\bar{X}_n^j\delta_K(nj\omega_m) \\ & + (-1)^j X_n^j \delta_K(-nj\omega_m))\Big|, \end{aligned} \tag{4.15}$$

where the bar denotes complex conjugates, β_n (defined below) is the harmonic-dependent modulation index, and the notation $\delta_K(x_0) = \delta_K(x - x_0)$ is used for brevity where $\delta_K(x)$ is the Kronecker delta function.

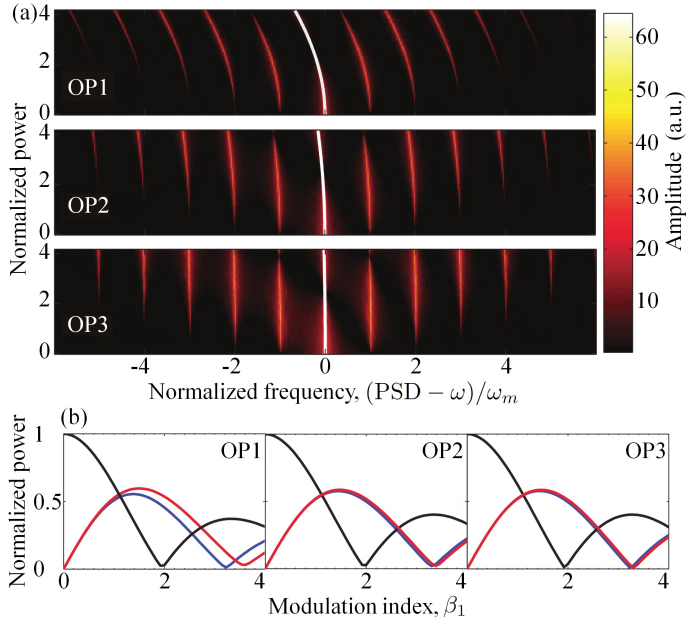

Figure 4.5: (a) Carrier frequency shift as a function of the normalized frequency. The white line is obtained from Eq. (4.16). The different curvatures of each OP result in a different magnitude of C_2. (b) Asymmetric sidebands as a function of the first-order modulation index β_1 and at $\omega_m/2\pi = 100$ MHz. The asymmetry is more pronounced for the OP where the curvature is higher.

4.2.2 Numerical evaluation

The derived PSD uncovers the main features of NFAM in STOs and relates them to intrinsic variables. Consequently, it is possible to numerically evaluate the PSD in order to verify the experimental observations. We choose material parameters consistent with NiFe: $\mu_o M_s = 0.8$ T and $\alpha_G = 0.01$. The external field $\mu_o \vec{H}_a = 1$ T is applied out-of-plane. We choose three operating points (OP1, OP2, OP3) at different supercriticalities so that $\Gamma_p/2\pi = 11.2$, 44.8, and 156.8 MHz. As will be shown below, Γ_p is the most relevant parameter in relation to the modulation characteristics of STOs.

Analyzing the PSD of Eq. (4.15), the following characteristics can be described:

1. The PSD in Eq. (4.15) consists of a carrier frequency convoluting with an AM term and a series of generally asymmetric FM terms (first to third terms in the RHS).

2. The carrier frequency is shifted by the quantity $2\nu\Gamma_p A_0$, which can be also expressed as

$$2\pi f_s = -\frac{\mu_m \nu C_2 B_1}{2}. \tag{4.16}$$

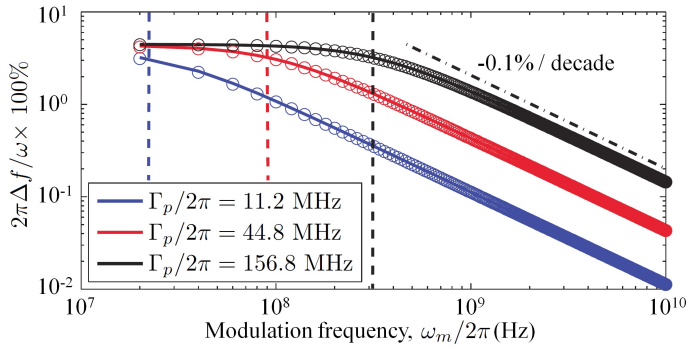

Figure 4.6: Normalized peak frequency deviation Δf as a function of the modulation frequency. The solid lines are calculated using only β_1 while the circles are calculated numerically. The vertical dashed lines represent the cut-off frequency $2\Gamma_p$ for each OP. The dot-dashed line is a guide for the eye.

proportional to the modulation strength and the STO nonlinearity constant C_2. This is in complete agreement with the experimental observations and the numerical evaluation of the simple auto-oscillator framework where C_2 has a well-defined sign [Fig. 4.5(a)].

3. Generally asymmetric sidebands are obtained from the convolution between the AM and FM terms. Although a meaningful analytical expression cannot be found, it is clear that the asymmetry arises from the influence of higher order harmonics and the imaginary component of complex variable X_n. In particular, $X_1 = B_1(1 + i\omega_m/2\Gamma_p)$ so that the increase of the modulation frequency should lead to an increased asymmetry. Such asymmetries are shown from the Bessel-like carrier and sideband amplitudes in Fig. 4.5(b) at $\omega_m/2\pi = 100$ MHz. Again, this is in qualitative agreement with the experimental observations.

The NFAM obtained from the auto-oscillator framework further uncovers the form of the modulation index, defined as

$$\beta_n = \frac{2\nu\Gamma_p|X_n|}{n\omega_m} \propto \frac{2\nu\Gamma_p}{n\omega_m}\frac{1}{\sqrt{(n\omega_m)^2 + (2\Gamma_p)^2}} = \frac{2\pi\Delta f}{\omega_m}. \tag{4.17}$$

From the modulation index, it is possible to define the modulation bandwidth (MBW). This figure-of-merit gives a measure of the frequency range in which an oscillator has optimal modulation properties. A common criterion is to find the linearity degradation of the modulation index, defined as the 3 dB power attenuation of an expected carrier or sideband power. In our framework, such estimation can be performed analytically by considering a vanishing modulation frequency and an arbitrary μ_m, so that the first-harmonic modulation index is β_i. By maintaining the ratio μ_m/ω_m constant while looking for $\beta_f = \beta_i/\sqrt{2}$, the MBW of an STO is found to be $2\Gamma_p$. This result

implies that the MBW depends on the operation point of the STO. It is possible to represent such a deviation from linearity with the factor Δf normalized to the STO frequency shown numerically and analytically in Fig. 4.6. One can understand this figure as a transfer function for STOs under modulation where a characteristic low-pass filter behavior is observed, with a linear rolloff after the cutoff frequency $2\Gamma_p$ (dashed vertical lines).

4.3 Modulation of phase-locked STOs

The previous two sections demonstrated that the STO nonlinearities are responsible for the non-Adlerian synchronization and the NFAM. In this section, we are interested in the combined action of synchronization and modulation. There are two main motivations behind this study:

1. It is technologically relevant to study the modulation of mutually synchronized STOs where power is enhanced to the level required for commercial applications. An experimental study performed by Pogoryelov *et al.* [98] showed the possibility of modulating synchronized STOs, however their study left unanswered questions regarding the combined dynamics.

2. The transient ringing frequency in the non-Adlerian synchronization was shown to manifest as sidebands [147, 33], similar to those observed by AM. However, such sidebands are not observed in the PSD due to their transient character. From this perspective, modulation is an alternative to continuously excite this intrinsic resonance under synchronization and bring such features above the experimental noise floor.

From a qualitative point of view, synchronization and modulation have opposite effects on the STO instantaneous phase. The effect of synchronization is to maintain the phase fixed while the effect of modulation is to continuously vary the phase. These different regimes suggest a rich phase space and it is difficult to predict the dynamical outcome *a priori*. In the following, we demonstrate that there are two main outcomes as a function of μ_m, where the synchronization regime is either perturbed or destroyed. We consider the case of injection locking for the sake of clarity. However, the analytical results can be extended to a mutual synchronization regime.

4.3.1 Dynamical equations

As in the previous sections, we start by setting the auto-oscillator equation, in this case combining the modulating term with an external source of injection power $f = \xi\alpha_G\omega_o \tan\gamma_o\mu_{inj}/2\sqrt{2}$ and frequency ω_e

$$\frac{dc}{dt} + i\omega(|c^2|)c + (\Gamma_+(|c^2|) - \Gamma_-(I(t), |c^2|))c = fe^{i\omega_e - i\phi}. \tag{4.18}$$

Assuming a phase-locked initial state, the linearization of Eq. (4.18) leads to a coupled set of equations as a function of δp and ϕ given by

$$\frac{\delta p}{dt} = K_1 \cos\omega_m t - K_2\phi - [K_3 + K_4 \cos\omega_m t]\,\delta p, \tag{4.19a}$$

$$\frac{\delta \phi}{dt} = K_5 \delta p + K_6 \phi, \tag{4.19b}$$

where the coefficients are given by

$$K_1 = \xi\Gamma_G(1-p_o)\mu_m, \tag{4.20a}$$

$$K_2 = f\sin\phi_o/\sqrt{p_o}, \tag{4.20b}$$

$$K_3 = 2\Gamma_p - f\cos\phi_o/\sqrt{p_o}, \tag{4.20c}$$

$$K_4 = 2\xi\Gamma_G(2p_o-1)\mu_m, \tag{4.20d}$$

$$K_5 = 2\nu\Gamma_p - f\sin\phi_o/\sqrt{p_o}, \tag{4.20e}$$

$$K_6 = -f\cos\phi_o/\sqrt{p_o}. \tag{4.20f}$$

Clearly, the set of Eq. (4.19) are similar the modulated set of Eq. (4.11). Consequently, we seek a Fourier series solution that can be truncated in order to find a recursive generation of the coefficients as in appendix A.1.

4.3.2 Ringing frequency excitation

An analytical solution of Eq. (4.19) can be obtained in the low modulation regime, where the condition $K_4 \ll \Gamma_p$ is fulfilled. In other words, this regime implies that the modulation-induced fluctuations are strongly damped by the STO restoration rate. Further assuming a vanishing frequency mismatch ($\Delta\omega \to 0$), it is possible to obtain a closed relation for the first-harmonic maximum power

$$\delta p_{max} = \frac{K_1\omega_m}{\sqrt{\left(\omega_m^2 - K_2K_5\right)^2 + K_3^2\omega_m^2}}. \tag{4.21}$$

The form of Eq. (4.21) is resonant *only* as a function of ω_m. The maximum power is thus excited at a frequency ω_{max}, given by

$$\omega_{max} = \Gamma_p\sqrt{\frac{\mu}{\mu_{cr}}}, \tag{4.22}$$

where $\mu_{cr} = 2F_{cr}\sqrt{2p_o}(\xi-1)/\Gamma_p\tan\gamma_o$ is the critical strength for non-Adlerian dynamics and $F_{cr} = \Gamma_p/(2\nu\sin\phi_o)$ as derived in Ref. [147]. Equation (4.22) is the asymptotic approximation to the ringing frequency (section 4.1.2).

In order to test this analytical solution, we perform macrospin simulations with the same parameters as in section 4.1.4. Since a synchronized STO was assumed as the starting point, the simulations are performed according to the following protocol:

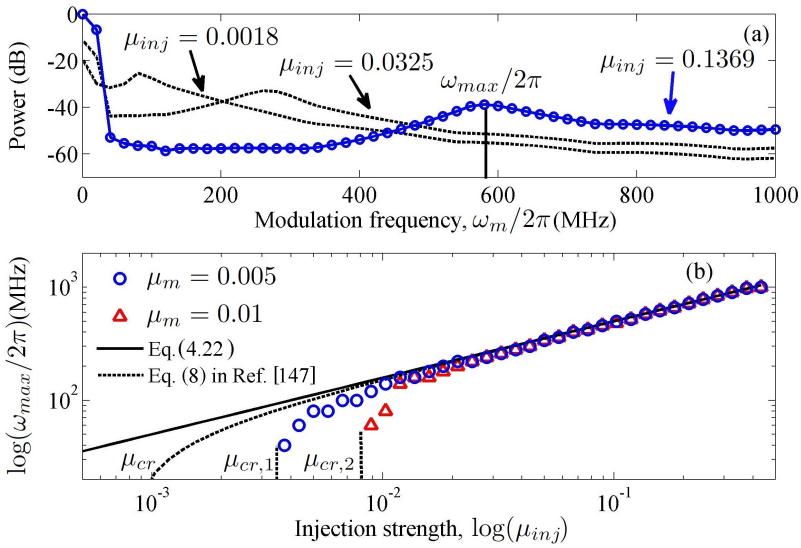

Figure 4.7: (a) Maximum sideband power as a function of the modulation frequency μ_m for several values of μ_{inj}. Resonance is observed as the maximum ω_{max} of the sideband power. Collecting ω_{max} as a function of μ_{inj} allows us to construct (b), showing good agreement with the analytical estimates. However, it is shown that μ_{cr} depends on μ_m, indicating non-linear effects that are neglected in the analytical approximation.

1. The STO is driven to stable oscillations by biasing it at $I_{dc} = 3.5$ mA ($\xi = 1.23$) for 20 ns. For this choice of parameters, the STO oscillates at $\omega/2\pi = 24.27$ GHz.

2. An injection current, $I_{ac} = \mu_{inj} I_{dc} \cos \omega_e t$ is added to the dc bias at the same STO free-running frequency, i.e., $\omega_e = \omega$. This regime is sustained for 100 ns to ensure proper convergence to a phase-locked state.

3. The modulation current is added to the bias and injection currents. The modulation frequency, $\omega_m/2\pi$, is swept between 20 and 1000 MHz in steps of 20 MHz. For each $\omega_m/2\pi$ value, the simulation is run for 100 ns.

4. The resulting time trace is transformed to a series of spectra by performing fast Fourier transforms (FFT) using a Hann window and zero padding to achieve a frequency resolution of 9.5 MHz.

From the various FFTs, it is possible to extract the power of the modulation sidebands as a function of $\omega_m/2\pi$, as shown by the blue line in Fig. 4.7(a), in the case where $\mu_m = 0.005$. As expected from Eq. (4.21), the power exhibits resonance and ω_{max} can be extracted.

Repeating the simulation protocol and the above procedure for different values of μ_{inj}, we obtain ω_{max} as a function of μ_{inj}, as represented by empty

symbols in Fig. 4.7(b). Comparison with the analytical estimate of Eq. (4.22) (solid line) corroborates that we obtain an asymptotic approximation to the ringing frequency. In addition, comparison with the ringing frequency obtained in Ref. [147], shows that μ_{cr} is not recovered from the modulation excitation. On the contrary, it appears to exhibit a dependence on μ_m. This is an indication of the strongly non-linear dynamics occurring in this system. However, the same results prove that the ringing frequency is indeed resonantly excited by the modulation source in the limit of low μ_m.

4.3.3 Non-linear resonance and unlocking

The asymptotic approximation derived in the previous section breaks down as μ_m increases. A quantitative limit for the maximum modulation, μ'_m, can be estimated from the condition $\delta p_{max} \approx p_o$ at the maximum frequency

$$\delta p_{max}(\omega = \omega_{max}) \approx p_o = \frac{\xi}{\xi - 1}(1 - p_o)\frac{\mu'_m}{2}. \tag{4.23}$$

There are two important observations that can be made from the condition Eq. (4.23):

1. The low modulation condition monotonically increases as a function of the supercriticality. However, the auto-oscillator frequency, conceived as a small amplitude perturbation, does not strictly work at high supercriticalities.

2. The breakdown of the low-modulation condition precludes an accurate resonant excitation of the ringing frequency.

Due the above observations, and the lack of a large amplitude magnetization precession theory including modulation, we perform macrospin simulation to study the effects of high modulation strengths.

A similar simulation protocol as described in section 4.3.2 is performed with the difference that we now sweep μ_m while maintaining a fixed μ_{inj}. Notably, the frequency is swept back and forth, however, no signs of hysteresis were found. In order to unambiguously study the non-linear dynamics, in this section we determine the maximum phase deviation between the STO and the injection source, parameterized by $\Delta\psi = |\max(\psi(t)) - \min(\psi(t))|$, where $\psi(t)$ is the instantaneous phase difference. This method is sensitive to the sampling time used in the simulation, here set to 2 ps, which introduces a maximum error of ~ 10 deg. The use of $\Delta\psi$ is justified by the strong power and phase coupling in STO. Additionally, this quantity is convenient to describe both the resonant features of the power and the state of the STO. In particular, we define that the STO is unlocked if $\Delta\psi$ is not bounded between 0 and 360 deg.

The first indication of the non-linear dynamics induced by μ_m can be observed in Fig. 4.8(a). Indeed, the modulation induced resonance at about 840 MHz for $\mu_{inj} = 0.2812$ (blue line) acquires the aspect of non-linear resonance as μ_m increases. Such asymmetric resonances, or foldover, is well known

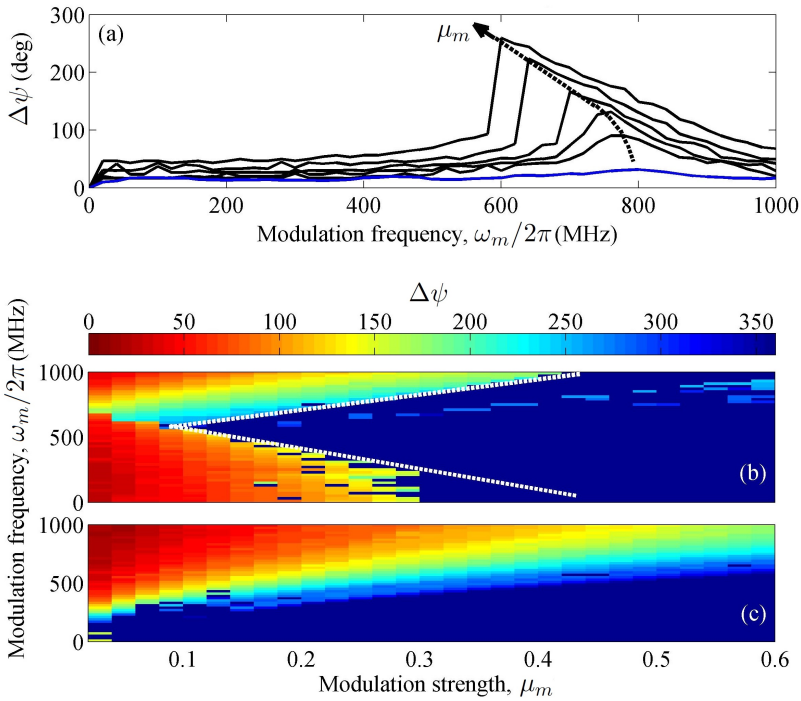

Figure 4.8: (a) Non-linear resonance excited by the modulation source observed by the phase deviation $\Delta\psi$. This mechanism leads to the resonant unlocking indicated by white dashed lines in the $\Delta\psi$ colormap as a function of ω_m and μ_m at $\mu_{inj} = 0.2812$ (b). When the injection strength is reduced down to $\mu_{inj} = 0.01$, (c) the modulation is strong enough to non-resonantly unlock the STOs as shown for $\mu_m > 0.3$ in (b) and dominating the colormap in (c).

for non-linear processes such as spin-wave excitations in thin films [124] and the carrier frequency shift discussed in section 4.2.3. Further increasing μ_m leads to an unbounded increase of $\Delta\psi$ suggesting that modulation can break the phase-locking regime.

It is instructive to explore the μ_m vs ω_m space, shown as a color map in Fig. 4.8(b). From this figure, we can identify two different mechanisms for modulation-mediated unlocking:

1. **Resonant unlocking:** In the region spanning $0.1 < \mu_m < 0.3$, unlocking occurs when the resonance peak of $\Delta\psi$ surpasses the bounded condition, while it is otherwise locked. In other words, the injection source provides an intrinsic frequency that resonates strongly with the modulation source so that phase slips occur. This regime is highlighted with white dashed lines.

2. **Nonresonant unlocking:** In the region $\mu_m > 0.3$, the STO is always

unlocked at low frequencies. This can be understood from the fact that modulation dominates the dynamics and the injection source does not have the time or the bandwidth to fix the phase. This observation is in agreement with the NFAM bandwidth (section 4.2.3), which predicts an ideal STO modulation at low frequencies.

The above mechanisms are also observed at lower injection strengths [Fig. 4.8(c)]. In particular, it is observed that the nonresonant unlocking regime dominates for low μ_{inj}, in agreement with the qualitative description provided above.

Finally, we stress that the dynamics described in this section are also observed when temperature is taken into account, suggesting the use of combined injection and modulation as a plausible means to study the effect of the non-linear transient dynamics in STOs.

5

Multi-mode generation dynamics

The Hamiltonian formalism reviewed in section 2.4.7 makes it possible to map the LLGS equation into an approximated complex ODE. In order to derive the auto-oscillator equation, single-mode and small-amplitude magnetization dynamics are assumed. Despite this arguably limiting assumption, the auto-oscillator equation has been successful in explaining experimental results reasonably far from its validity range.

However, some experiments have shown multi-mode generation in a variety of geometries [70, 113, 143], revealing unambiguous evidence of mode-hopping [74, 88, 89] and periodic mode transitions [13, 12]. The origin of mode transitions in nanopillar STOs can be attributed to physical confinement. However, in NC-STOs, the origin of mode transitions is not well understood and is generally attributed to structural defects and roughness of the magnetic layer.

Regardless of the physical origin, multi-mode generation is routinely observed accompanied by a linewidth broadening. This can be simply understood from the fact that mode transitions lead to shorter correlation lengths. However, this effect has not been included in a theoretical framework. In the following, we show that it is possible to derive a multi-mode theory from a similar Hamiltonian formalism. Such a multi-mode theory makes it possible to model a wide range of dynamical scenarios including the recently observed mode coexistence. In particular, coexistence provides unequivocal proof that STOs are generally multi-mode generators. Finally, we perform experiments in a modified NC-STO geometry in order to test both the analytical predictions and the physical mechanism governing the dynamics.

5.1 Multi-mode Hamiltonian formalism

The multi-mode Hamiltonian formalism was recently proposed as an extension of the auto-oscillator equation, in light of the dramatic linewidth broadening close to a mode transition observed in MTJs [88] and NC-STOs [89]. Recently, a rigorous derivation was presented by Heinonen *et al.* [57] by mapping the

micromagnetic LLGS equations into an approximate Hamiltonian system. The main idea behind the derivation is to consider an orthonormal set of magnon states supported by their Bose-Einstein distribution [section 2.2.4]. Considering two main generation modes, it can be shown that the thermally populated states act as coupling channels between the modes. Such interactions are both conservative and non-conservative, and lead to a generalization of the auto-oscillator equation including off-diagonal damping and STT terms as well as a linear coupling coefficient. Notably, due to the average balance between damping and STT, the total power of the main modes remains constant.

In terms of the auto-oscillator framework, it is possible to write the coupled equations for the two-mode oscillator as

$$\begin{aligned} \frac{dc_1}{dt} &+ i\omega(|c_1|^2,|c_2|^2)c_1 + \left[\Gamma_+(|c_1|^2,|c_2|^2) - \Gamma_-(|c_1|^2,|c_2|^2)\right] c_1 \\ &= K_{1,2}e^{i\phi_{c(1,2)}}c_2 + \tilde{f}_1, \qquad (5.1a) \\ \frac{dc_2}{dt} &+ i\omega(|c_2|^2,|c_1|^2)c_2 + \left[\Gamma_+(|c_2|^2,|c_1|^2) - \Gamma_-(|c_2|^2,|c_1|^2)\right] c_2 \\ &= K_{2,1}e^{i\phi_{c(2,1)}}c_1 + \tilde{f}_2. \qquad (5.1b) \end{aligned}$$

In Eq. (5.1), the off-diagonal terms are included in the non-linear frequency and damping terms while the linear coupling terms are written in a phasor form with strength K and phase ϕ_c. The set of Eq. (5.1) is general [57], so that the explicit form of each term will be provided below for the particular cases studied in this thesis. Furthermore, the thermal fluctuations for each mode, $\tilde{f}$, are also explicitly considered.

5.2 Multi-mode dynamics

In this chapter, we aim to describe a NC-STO with the multi-mode equations. In particular we assume two modes of generally different frequencies, ω_1 and ω_2, and we express the coefficients as:

- $\omega(|c_1|^2) = \omega_o + N|c_1|^2$, where the different frequencies are enforced only by the different complex amplitudes.
- $\Gamma_+(|c_1|^2,|c_2|^2) = \Gamma_G(1+\bar{Q}_1|c_1|^2+\bar{Q}_0|c_2|^2)$, where $\bar{Q}_1$ and $\bar{Q}_0$ are general diagonal and off-diagonal damping coefficients.
- $\Gamma_-(|c_1|^2,|c_2|^2) = \xi\Gamma_G(1-\bar{P}_1|c_1|^2-\bar{P}_0|c_2|^2)$, where $\bar{P}_1$ and $\bar{P}_0$ are general diagonal and off-diagonal STT coefficients.

Enforcing total power conservation, it is convenient to express Eq. (5.1) as a function of the phase difference ψ and the modal energy mapped by the variable $-\pi/2 < \theta < \pi/2$ satisfying $p = p_1\cos^2(\theta/2+\pi/4) + p_2\sin^2(\theta/2+\pi/4)$. Performing some algebra, the differential equations can be written as [ap-

pendix B.1]

$$
\begin{aligned}
\dot{\theta} &= \cos\theta\Gamma_G p\frac{1-\sin\theta}{2\omega_1}\left[\bar{Q_1}-\bar{Q_0}+\xi(\bar{P_1}-\bar{P_0})\right] \\
&\quad -\cos\theta\Gamma_G p\frac{1+\sin\theta}{2\omega_2}\left[\bar{Q_2}-\bar{Q_0}+\xi(\bar{P_2}-\bar{P_0})\right] \\
&\quad +K(1-\sin\theta)\sqrt{\frac{\omega_2}{\omega_1}}\cos\left(\phi_c-\psi\right) \\
&\quad -K(1+\sin\theta)\sqrt{\frac{\omega_1}{\omega_2}}\cos\left(\phi_c+\psi\right) \\
&\quad +\sqrt{\frac{2}{p}}\left[\cos\frac{\theta}{2}(f_2^R-f_1^R)-\sin\frac{\theta}{2}(f_2^R+f_1^R)\right], \qquad (5.2a) \\
\dot{\psi} &= \frac{pN_0}{2}\left[\frac{1-\sin\theta}{\omega_1}-\frac{1+\sin\theta}{\omega_2}\right] \\
&\quad +K\frac{1-\sin\theta}{\cos\theta}\sqrt{\frac{\omega_2}{\omega_1}}\sin\left(\phi_c-\psi\right) \\
&\quad -K\frac{1+\sin\theta}{\cos\theta}\sqrt{\frac{\omega_1}{\omega_2}}\sin\left(\phi_c+\psi\right) \\
&\quad +\sqrt{\frac{2}{p}}\left[\frac{\cos\frac{\theta}{2}(f_2^I-f_1^I)-\sin\frac{\theta}{2}(f_2^I+f_1^I)}{\cos\theta}\right], \qquad (5.2b)
\end{aligned}
$$

where the Gaussian thermal fluctuation term is separated in complex parts $\tilde{f}=\tilde{f}^R+i\tilde{f}^I$ and its second moment $\langle\tilde{f}(t),\tilde{f}(t')\rangle=p\Delta\omega_l\delta(t-t')$ is given in terms of the linear oscillator linewidth $\Delta\omega_l$ derived from the auto-oscillator framework [67, 69, 68, 129, 118].

The set of Eq. (5.2) describe a two-dimensional phase space supporting different dynamical scenarios. The richness of the possible outcomes stems from the nonlinearity of the equations. Neglecting the thermal fluctuations, linear stability can be used in order to study limiting cases [appendix B.2]. Two main dynamical states are found:

1. **Single mode:** In the limit $K\rightarrow 0$, a stable solution is obtained for $\theta=\pm\pi/2$ so that all the available energy is taken by a single mode. Clearly, Eq. (5.2b) diverges in this regime i.e., a phase difference cannot be established, and the phase space is described by vertical lines [Fig. 5.1(a)]. The linear stability analysis demonstrates that the modes can be independently stable by satisfying the condition $\bar{Q}_i+\xi\bar{P}_i<\hat{Q}_0+\xi\hat{P}_0$.

2. **Coexistence and periodic energy transfer:** In the limit of large coupling, linear stability analysis shows that the determinant of the Jacobian matrix allows real (fixed points) and imaginary (limit cycles) solutions as a function of the coupling phase ϕ_c [Fig. 5.1(c)]. Fixed points occur at $\theta=0$ so that both modes coexist and equally share the power. Limit cycles denote a periodic energy transfer between near-single modes.

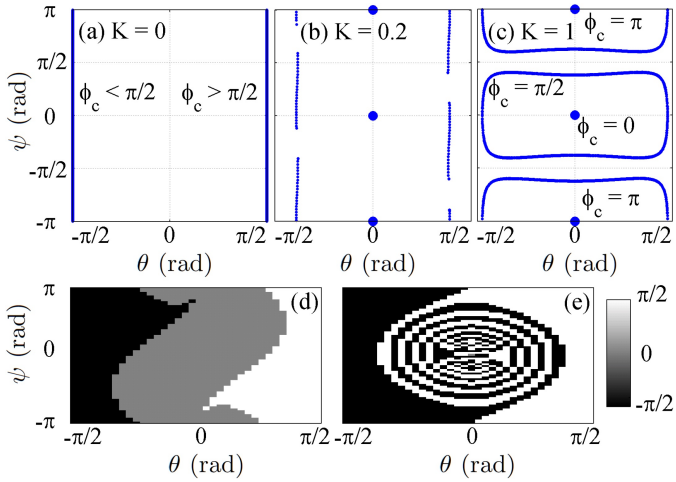

Figure 5.1: Phase spaces spanned by θ and ψ for (a) $K = 0$: single mode; (b) $K = 0.2$: near-single modes and coexistence; and (c) $K = 1$: coexistence and periodic energy transfer. For the case $K = 0.2$, the basins of attraction are shown for (d) $\phi_c = 0$ and (e) $\phi_c = \pi/2$. In the latter, the spiral feature is reminiscent of a particle with friction in a double potential well.

Between both limiting cases, an analytical solution can be found by Taylor expansion. However, the large coefficients limit the usefulness and insight obtained by such an expression. Instead, it is possible to numerically integrate Eq. (5.2) to obtain an intermediate solution. It has been found that the generation dynamics are generally coexistent or exhibit *near-single modes* [Fig. 5.1(b)]. The stable state selection process has also been found to depend on ϕ_c and the initial conditions in ψ and θ, mapped as basins of attraction in Fig. 5.1(d-e).

The near-single modes and their equivalent basin of attraction [Fig. 5.1(e)], suggest that the energy landscape is similar to a particle with friction in a double potential well [93]. From an experimental perspective, this suggests that the model equations can describe the observed mode-hopping in STOs [74, 88, 89]. Furthermore, a periodic energy transfer was argued to describe the dynamics in NC-STOs exhibiting both a propagating and a bullet spin wave mode [12, 13]. Consequently, the multi-mode model equations contain, in principle, the necessary physics to describe such complicated dynamics in relatively simple terms.

5.3 Generation linewidth of NC-STOs

The multi-mode dynamical equations of section 5.1.2 offer the possibility of exploring a large phase space of possible generation dynamics. In the following, we restrict ourselves to the study of the generation linewidths of experimentally relevant modes in NC-STOs. Analytically, this is achieved by deriving

the auto-correlation function, $\mathcal{K}$, for two modes

$$\mathcal{K} = \langle [c_1(t) + c_2(t)]\,[c_1^*(t') + c_2^*(t')] \rangle. \tag{5.3}$$

As shown below and suggested in Ref. [118], such an autocorrelation is generally related to power and phase fluctuations. In particular, the autocorrelation of the two-mode system is always proportional to the phase fluctuation's second moment [appendix B.3]. Consequently, it is sufficient to study the phase fluctuations via linearization of Eq. (5.2)

$$\dot{\delta p} = C_{pp}\delta p + C_{p\psi}\delta\psi + f_p, \tag{5.4a}$$

$$\dot{\delta\psi} = C_{\psi p}\delta p + C_{\psi\psi}\delta\psi + f_\psi, \tag{5.4b}$$

where the coefficients are given in appendix B.4.

5.3.1 Continuous mode transitions

Current-dependent experiments on the spin wave propagating mode (section 2.5.2) usually exhibit a stairway-like behavior for the frequency tunability, in contrast to the auto-oscillator theory prediction. The behavior close to the "steps" has been attributed to mode transitions between propagating modes with similar frequencies. From this point of view, the linewidth broadening can be attributed to the reduction of the correlation length when mode-hopping events occur. However, the single-mode theory was also able to reproduce the linewidth broadening by considering a current dependency on the nonlinearity coefficient [89]. These opposing ideas compromise the understanding of the underlying physics behind the linewidth broadening. In order to clarify this matter, we assume that such a broadening is indeed due to mode-hopping between similar modes in the context of the multi-mode framework.

The assumption of similar modes is enforced in the multi-mode framework by symmetrical equations with average energies $\pm\langle\theta_o\rangle$. The existence of two average energies for analytically identical modes is possible by virtue of the independent stability conditions for single modes (section 5.1.2). Further assuming that $\phi_c \to \pi/2$, means that the phase space is characterized by two energy minima separated by an unstable saddle point at $\theta = 0$ [Fig. 5.1(b) and (e)].

The aforementioned phase space can be verified numerically by solving Eq. 5.2. We choose parameters consistent with the NC-STO used in Ref. [89]. Such a device consists of a 4.5 nm thick NiFe free layer with saturation magnetization $\mu_o M_s \approx 0.88$ T, exchange length $\lambda_{ex} = 5$ nm, and $\alpha_G = 0.01$. An external field $\mu_o\vec{H}_a = 1$ T is applied at 80 deg with respect to the NiFe film plane. Whereas the NC in Ref. [89] was a 50 nm $\times$ 150 nm ellipse, we assume here, for simplicity, a circular NC of radius $R_c \approx 40$ nm that has a similar effective current-carrying area and an assumed supercriticality $\xi \approx 1.1$. In the two-mode oscillator framework, such parameters are mapped to $\omega_o/2\pi = 11.94$ GHz, $p \approx 0.017$, $\bar{Q} \approx 4.6\omega$, $\bar{P} \approx \omega$, $\Gamma_G/2\pi \approx 120$ MHz, $N/2\pi\omega \approx 68$ GHz, $\omega/2\pi \approx 13.13$ GHz, and $\Delta\omega/2\pi = 0.6$ MHz. These parameters agree fairly well with the near-threshold generation of the real device.

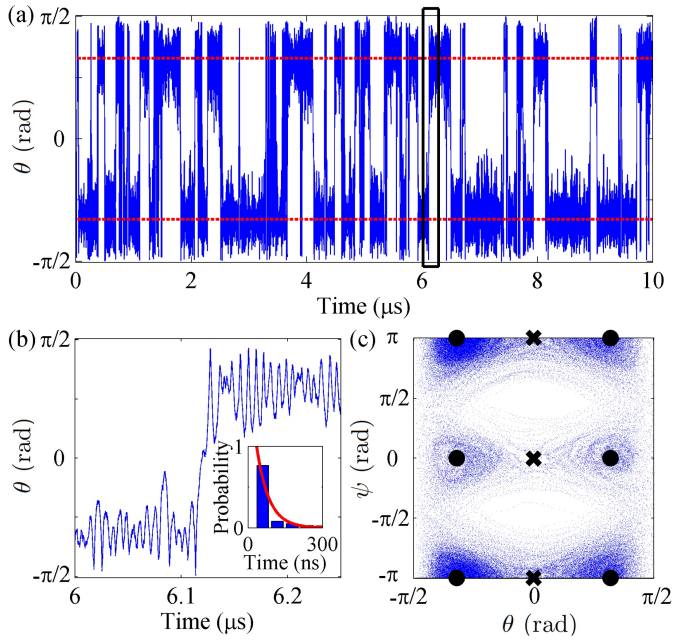

Figure 5.2: (a) Time trace of θ exhibiting mode-hopping events between $\pm\langle\theta_o\rangle$ (red dashed lines). The section in the black box is detailed in (b), where the underlying relaxation frequency is observed. The inset shows the exponential distribution of the time difference between mode-hopping events, in agreement with a Poisson process. (c) Phase space of the time trace (a) showing that the stable modes (fixed points indicated by black circles) are thermally driven to mode-hop via saddle points (black crosses).

In order to complete the analytical description, we assume parameters for the off-diagonal terms $\bar{Q}_0 = 2\bar{Q}$ and $\bar{P}_0 = 2\bar{P}$, providing stability for both modes. For $K = 0.3$, the numerical integration of Eq. 5.2 returns the expected mode-hopping time trace [blue lines Fig. 5.2(a)] between the stable states $\pm\langle\theta_o\rangle$ (red dashed lines). A zoom of a particular mode-hopping transition (black box) is shown in Fig. 5.2(b), where the intrinsic relaxation frequency is apparent, and related to the strong nonlinearity coefficient N. The mode-hopping time-trace can be also visualized in its phase space, where the maxima and saddle points are indicated, respectively, by black circles and crosses. A similar behavior is observed for ring lasers [7, 41] where the master equations resembles Eq. 5.2.

The generation linewidth in this mode-hopping regime arises from two vastly different time-scales:

1. The perturbation introduced by thermal fluctuations has a short time-scale and, assuming the the perturbation is small, it can be related to the phase difference second moment obtained from the linearized Eq. (5.4) by the method of variation of parameters [appendix B.5]. Performing Taylor expansion to second order and expressing $|\tau_l| = |t' - t|$, the self-

and cross-correlated second moments are given by

$$\langle \psi_i(t)\psi_i(t')\rangle = \gamma_{L,ii}|\tau_l| + \gamma_{G,ii}|\tau_l|^2, \tag{5.5a}$$

$$\frac{\langle \psi_i(t)\psi_j(t')\rangle}{\cos\langle\theta_o\rangle} = \gamma_{L,ij}|\tau_l| + \gamma_{G,ij}|\tau_l|^2, \tag{5.5b}$$

where the coefficients γ_L and γ_G are mode dependent and are generally functions of the coefficients of Eq. (5.4) [appendix B.5].

2. Mode-hopping events occur as sharp phase jumps on a longer time-scale [Fig. 5.2(a)] and cannot be analytically obtained from Eq. (5.2). Consequently, we incorporate such events as an additional phase parametrized by a series of sudden jumps, separated by random, long time intervals. This description is proper for a Poisson process [116] which is only described by its rate, λ_P. Indeed, the distribution of the relative time between mode-hopping events is numerically found to agree with an exponential distribution, as shown in the inset of Fig. 5.2(b). Finally, it is known that the second moment of such a process is simply λ_P, so the phase difference is enhanced by a factor $-\lambda_P|\tau_l|$.

With these ingredients, the autocorrelation of mode-hopping dynamics take the approximate yet insightful form

$$\begin{aligned} 2\mathcal{K} \propto\ & (1-\sin\langle\theta_o\rangle)e^{-\gamma_{L,ii}|\tau_l|}e^{-\gamma_{G,ii}|\tau_l|^2}e^{-\lambda_P|\tau_l|} \\ & +(1-\sin\langle\theta_o\rangle)e^{-\gamma_{L,jj}|\tau_l|}e^{-\gamma_{G,jj}|\tau_l|^2}e^{-\lambda_P|\tau_l|} \\ & +\cos\langle\theta_o\rangle(e^{-\gamma_{L,ij}|\tau_l|}e^{-\gamma_{G,ij}|\tau_l|^2})^{\cos\langle\theta_o\rangle}e^{-\lambda_P|\tau_l|} \\ & +\cos\langle\theta_o\rangle(e^{-\gamma_{L,ji}|\tau|}e^{-\gamma_{G,ji}|\tau|^2})^{\cos\langle\theta_o\rangle}e^{-\lambda_P|\tau|}. \end{aligned} \tag{5.6}$$

From Eq. (5.6), it is observed that a cross-over to the temporal decay of the correlation dominated by decoherence occurs as λ_P increases. The resulting lineshape is obtained by the Fourier transform of the autocorrelation Eq. (5.6), from which the linewidth can be extracted. Each term of the RHS has a similar form which, after performing the Fourier transform, leads to a Lorentzian lineshape with a linewidth given by $\gamma_{L,ij} + \lambda_P$, convoluted by a Gaussian lineshape with a linewidth given by $4\sqrt{\gamma_{G,ij}\ln 2}$. Such a convolution is defined as a Voigt lineshape. Consequently, the general lineshape obtained from the Fourier transform of Eq. (5.6) is expected to be a sum of Voigt functions. A noteworthy point is that λ_P enhances the linewidth of the Lorentzian components, contributing to spectral broadening as observed experimentally [89]. The Gaussian contribution here arises from the response of Eq. (5.4) which is found to relax to zero [appendix B.5], i.e., the autocorrelation is lost after a finite time, leading to statistically independent modes and thus uncorrelated mode-hopping events. This mechanism has a different physical origin than the Gaussian lineshape that arises from a high temperature limit [118] or $1/f$ noise [66].

Numerically, the lineshape predicted from Eq. (5.6) can be obtained from the autocorrelation of $\delta\psi(t)$ multiplied by the Poisson factor with a mode-hopping rate λ_P estimated from the time trace of Eq. (5.2a). Such a lineshape

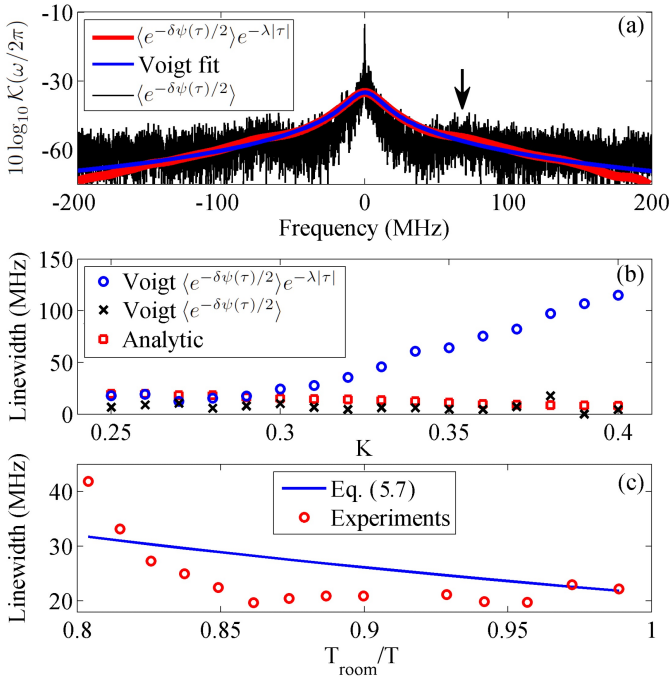

Figure 5.3: (a) Fourier transform of the autocorrelation calculated from the numerical integration of Eq. (5.4) (black). Mode-hopping events are included as a Poisson process with a mode-hopping rate calculated from the numerical solution of Eq. (5.2) (red). The best Voigt fit is shown in blue. (b) Voigt linewidth as a function of the coupling strength K, obtained from the best fit of the autocorrelation (black) and including mode-hopping events (blue). The analytical estimate is shown by red squares. The mode-hopping events dominate the linewidth when $K > 0.3$. (c) Experimentally measured linewidth (red circles) and linewidth obtained from Eq. (5.7) (blue line) with $\Delta E = 52$ meV extracted from a single experimental data point at 303 K. This simple fit shows a remarkably good agreement with the experimental data trend as well as its magnitude.

is shown in Fig. 5.3(a) by the red line for the parameters given earlier. We find the best Voigt fit following the approach of Ref. [77], as shown in the same figure by the blue line. For the chosen STO parameters, a single Voigt fit provides a good estimate of Eq. (5.6). The fitting procedure can be repeated as a function of K from which we obtain the Voigt linewidths, shown in Fig. 5.3(b) by blue circles. These numerical results can be quantitatively compared with the analytical estimates from Eq. (5.6) and Eq. (5.5). For the chosen parameters, we obtain $\gamma_{G,ii} \to 0$ so that $\gamma_{L,ii}$ provides a good estimate for the linewidth, shown in Fig. 5.3(b) by red squares. Clearly, the Voigt fit agrees well with the Lorentzian estimates when $K < 0.3$ suggesting that the linewidth is otherwise dominated by mode-hopping, i.e., the linewidth tends

to λ_P. We find that these linewidths *quantitatively* agree with the reference experiment [88] without any fitting parameters, suggesting that mode-hopping is the physical mechanism behind the observed linewidth broadening.

To further test the analytical estimates, we fit the spectrum of the phase difference autocorrelation shown by black lines in Fig. 5.3(a). Multiple Voigt functions can be identified in this case, in agreement with Eq. (5.6). In particular, there is a narrow peak consistent with $\gamma_{L,21} \approx \gamma_{G,21} \to 0$. The sidebands corresponding to the oscillatory relaxation of the system are observed at about ± 80 MHz (indicated by an arrow) which, together with the large fluctuations, allows us to reliably fit only two Voigt functions. In spite of these difficulties, the wider Voigt linewidth [black marks in Fig. 5.3(b)] is observed to follow the analytical trend, further confirming that the linewidth enhancement is due to mode-hopping events.

The fact that the dynamics are dominated by mode-hopping events indicates that the linewidth provides a direct measure of λ_P. Assuming an Arrhenius distribution for the mode-hopping rate, as it is a thermally-induced process, allows us to relate the linewidth to temperature in the form

$$\Delta E = k_B T \log \frac{f_a}{\lambda}, \tag{5.7}$$

where we assume that the attempt frequency $f_a = 160$ MHz corresponds to twice the intrinsic relaxation frequency since the phase-space is $\pi/2$-periodic in θ. Equation (5.7) reveals that an exponential linewidth broadening is expected as a function of T^{-1} near a mode-transition, in contrast to single-mode predictions [118]. Indeed, such a broadening was also observed in the reference experiment and a simple analytical estimate is found to agree fairly well [Fig. 5.3] by estimating $\Delta E = 52$ meV from a single experimental data point at 303 K [appendix B.6].

5.3.2 Spin-wave mode transitions

Field angle-dependent experiments on NC-STOs have shown the existence of both a spin wave propagating mode and a solitonic bullet mode (sections 2.5.2 and 2.5.3). In particular, the experiments performed by Bonetti *et al.* [13] showed that the modes would hop leading to an enhanced linewidth that could not be explained by single-mode theory alone. On the contrary, those results were compatible with the energy transfer regime identified in Fig. 5.1(c).

Additionally, measurements in NC-STOs with larger NCs exhibited evidence of mode coexistence [43] in strong contrast to previous observations. These novel results could be confirmed by micromagnetic simulations where the mechanism behind coexistence was attributed to the spatial localization of both modes. In other words, the propagating mode acquires a localized character below the field angle θ_L. As expected, this occurs exactly when the generation frequency is below the FMR, as shown in the experimental and simulated spectra of Fig. 5.4(a-b).

The experimental and simulation results obtained by Dumas, Iacocca, *et al.* [43] were performed with a rotatable applied field of fixed magnitude

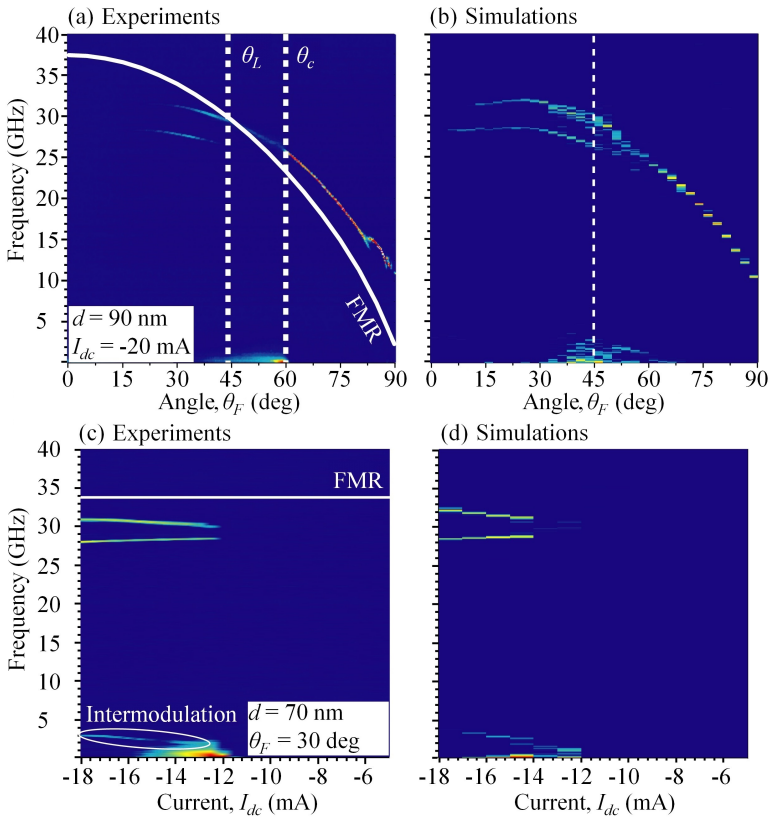

Figure 5.4: Experiments and simulations of angle dependent (a-b) and current dependent (c-d) scans. The angle scans exhibit coexistence, mode-hopping, and single mode generation as θ_F increases from 0 to 90 deg. The coexistence is further demonstrated in the current scans at $\theta_F = 30$ deg as a clear intermodulation peak. Both experiments and simulations agree remarkably.

$\mu_o \vec{H}_a = 0.965$ T (as described in section 3.3) and assuming standard parameters for NiFe thin films, namely $\mu_o M_s = 0.88$ T, $\alpha_G = 0.01$, and $\lambda_{ex} = 5$ nm. The results exhibit, in a single device, most of the possible dynamical regimes predicted in section 5.2.

1. Single mode oscillation is observed at field angles $\theta_F > \theta_c$ in Fig. 5.4(a-b), where θ_F is the field angle with respect to the film's plane and θ_c is a critical angle at which two modes start to be observed.

2. Mode-hopping is observed in the range $\theta_L < \theta_F < \theta_c$ as evidenced by the low frequency components in Fig. 5.4(a-b) identified as telegraphic hopping between the modes. As predicted in section 5.3.1, the linewidth in this regime is greatly enhanced.

3. Coexistence between the bullet and a high-frequency localized mode is

observed when $\theta_F < \theta_L$. Furthermore,the current-dependent experimental and simulated results at $\theta_F = 30$ deg [Fig. 5.4(c-d)] exhibit a well defined intermodulation peak both indicating that the modes are generating with a significant power and are strongly coupled.

In order to derive an analytical prediction for the generation linewidth of these cases, the results of sections 5.3.1 must be generalized for different frequencies. In the case of coexistence, Galilean invariance can be invoked to derive [appendix B.3] the autocorrelation function as

$$\begin{aligned} \mathcal{K} &= pe^{i\omega_1 t}\left(\cos^2\langle\chi\rangle + \frac{\sin(2\langle\chi\rangle)}{2}\right)e^{-\langle\psi(t)\psi(t')\rangle/2} \\ &+ pe^{i\omega_2 t}\left(\sin^2\langle\chi\rangle + \frac{\sin(2\langle\chi\rangle)}{2}\right)e^{-\langle\psi(t)\psi(t')\rangle/2}. \end{aligned} \tag{5.8}$$

Interestingly, the autocorrelation for both modes depends *only* on the phase difference (under Galilean invariance) leading to the prediction that both modes should exhibit identical linewidths. However, this result is only valid for strict coexistence i.e., $\langle\theta\rangle = 0$ and deviations from this trend are expected from experiments.

The solution of the phase difference second moments leads to the closed-form relation

$$\langle\psi(t)\psi(t')\rangle = -\frac{2p_o^2\Delta\omega_l}{C_{\psi\psi}}\left(\frac{C_{\psi p}^2}{C_{pp}^2 - C_{\psi\psi}^2} + 1\right)e^{C_{\psi\psi}|\tau_l|}, \tag{5.9}$$

which also leads to Lorentzian and Gaussian components under Taylor expansion, as in Eq. (5.5). Evaluating the coefficients [appendix B.4] indicates that the linewidth asymptotically decreases to $p_o^2\Delta\omega_l/4$ as a function of K. Of course, this trend is valid only when coexistence is established. Another interesting limit is found for very strong K, in which case the linewidth further depends on the factor $\sqrt{\omega_1\omega_2}/(\omega_1+\omega_2)$ which tends to zero as $\omega_1 \neq \omega_2$. Consequently, the minimum value $p_o^2\Delta\omega_l/4$ is approached as the frequencies are further apart.

5.4 Fine-tuning the generation dynamics

The generation dynamics discussed in the last two sections are intimately dependent on the linear coupling strength K. In particular, K determines the relative energy of the excited modes which, when similar enough, leads to ideally identical linewidths for modes with generally different frequencies.

In the context of NC-STOs and the excited modes discussed in section 5.3.2, the analytical predictions are limited since the auto-oscillator equations are strictly derived for the propagating mode. Consequently, a quantitative agreement is not expected without adjusting the expressions for the power-dependent frequency and positive and negative damping terms. However, due to the generality of the multi-mode model equations, we expect a qualitative agreement with experimental observations.

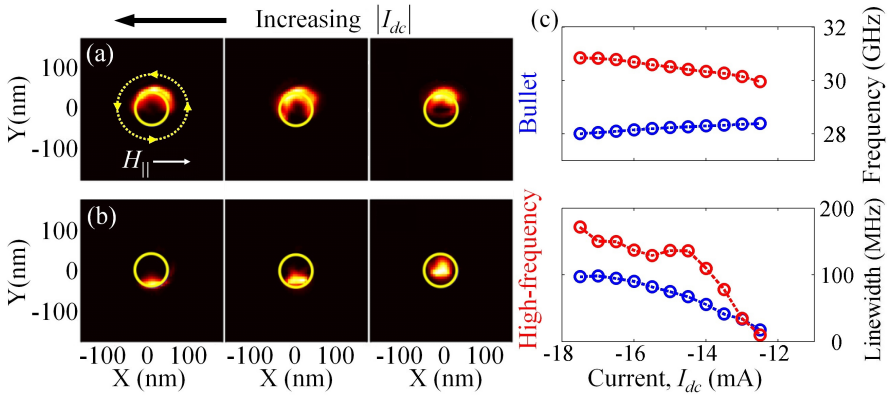

Figure 5.5: Mode energy distribution for the bullet (a) and high-frequency (b) modes in a NC-STO as a function of current. The current-induced Oersted field (dashed yellow line) localizes the bullet (high-frequency) mode at the local field minimum (maximum), where the in-plane external field component, $H_{\parallel}$, is indicated in white. (c) Fitting the experiment shown in Fig. 5.4(c), returns the frequency and linewidth for the bullet (blue) and high-frequency (red) modes. The linewidth increases with inter-mode spatial separation due to the reduced mode coupling.

The physical origin of the coupling strength K is of particular relevance in the following sections. From the analytical considerations of sections 5.3.1 and 5.3.2, we expect K to be closely related to the bias current by means of the creation of spin wave coupling channels in the thermal bath [57]. This mechanism leads to the linewidth reduction as a function of K, and thus bias current, discussed in section 5.3.2. However, recent measurements in circular NC-STOs [43] uncovered that the bias current induces an inter-mode spatial separation due to the Oersted-induced energy landscape, as shown by the micromagnetic mode energy distributions of both the high-frequency and bullet modes [Fig. 5.5(a-b)]. Such an inter-mode separation reduces the coupling between these modes, hence leading to a linewidth enhancement, as shown in Fig. 5.5(c) for the same spectra shown in Fig. 5.4(c).

To test the validity of these mode coupling mechanisms, NC-STOs with elliptical NCs were fabricated, where the ellipses had an aspect ratio of 1.5 and were tilted by an angle θ_{NC} with respect to the in-plane applied field component. The elliptical NCs provide means to tune the coupling strength K both by inter-mode spatial separation and bias-current magnitude.

5.4.1 Mode localization and coupling

The magnetization dynamics excited by elliptical NC are similar to those excited by circular NC. In fact, it is difficult to define a perfect circle both lithographically and in FD simulations, where the cells are perfect cubes. This assumption is verified by micromagnetic simulations of elliptical NC of minor

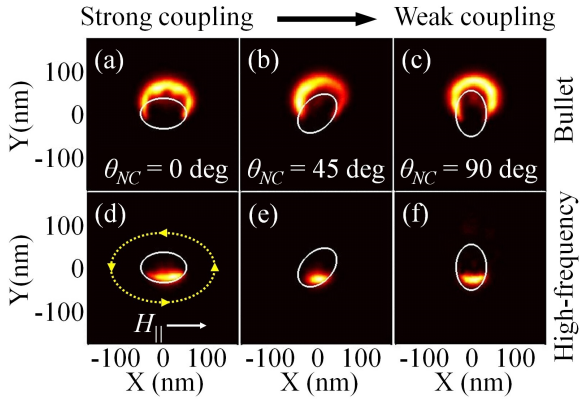

Figure 5.6: Mode energy distribution for the bullet (a-c) and high-frequency (d-f) modes for NC-STO with elliptical NC tilted $\theta_{NC} = 0$, 45, and 90 deg. In panel (d), the relative orientations of the current-induced Oersted (yellow) and in-plane field component (white) are indicated.

axis $d_m = 70$ nm.

Of particular interest is the mode energy distribution. The direction of the current-induced Oersted field is represented in Fig. 5.6(d) by a dashed yellow line, while the in-plane field component, $H_{||}$, is indicated by a white arrow. In agreement with Fig. 5.5, the bullet mode is localized at the local field minimum [Fig. 5.6(a-c)], while the high-frequency mode is localized at the local field maximum [Fig. 5.6(d-f)]. Interestingly, the modes acquire the shape of the NC and are preferentially excited at the boundary.

As for the case of circular NC-STOs, both the high-frequency and bullet mode interact by means of the exchange coupling between spins. However, such an interaction is of an evanescent character since their frequencies lie below FMR. Nonetheless, there exists a finite mode volume for such evanescent modes which, combined with the small dimensions of the NC, provides a physical mechanism for mode coupling. This is exactly the same mechanism proposed by the multi-mode theory.

5.4.2 Experimental measurements

Electrical characterization is performed in the setup described in section 3.3 and section 5.3.2. As we are mainly interested in the linewidth of the coexistent modes, we limit our study by using a $\mu_o \vec{H}_a = 0.9$ T Halbach array rotated in the range $10 < \theta_F < 45$ deg and a frequency scan between 20 and 35 GHz. A low-noise RF amplifier of gain 32 dB and bandwidth $18 - 40$ GHz was used. The obtained spectra were averaged 10 times and the resulting features were fitted in frequency, linewidth, and integrated power by an in-house developed MATLAB fitting and sorting procedure.

As expected from coexistent modes, the powers of both modes were similar for the six measured devices, regardless of the ellipse tilt, field angle, and bias

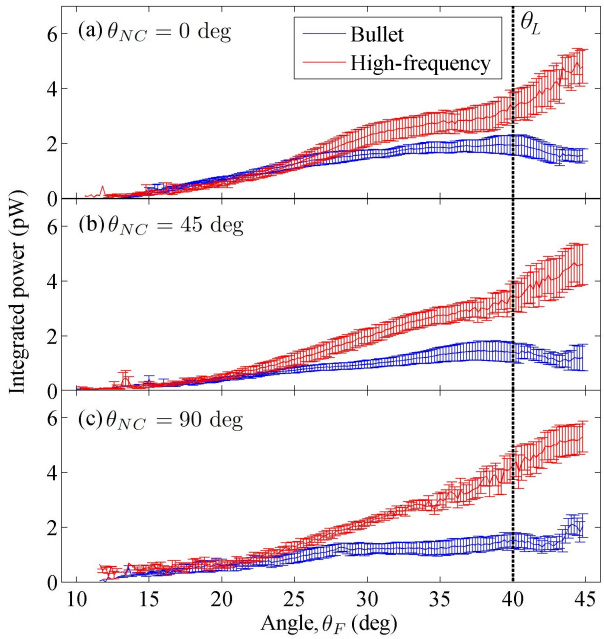

Figure 5.7: Average generated power of NC-STOs as a function of field angle θ_F with elliptical contacts at three tilt angles: $\theta_{NC} = 0$, 45, and 90 deg. The averages are performed in each case for two different devices measured at five bias currents between the range -16 to -26 mA. The critical angle for localization θ_L, is shown by a dashed line.

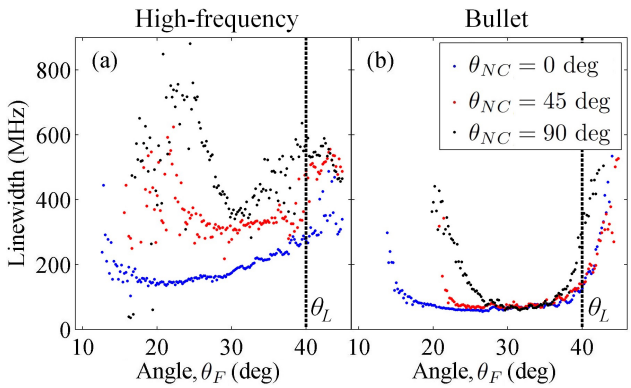

Figure 5.8: Generation linewidth of three devices at NC ellipse tilt angles $\theta_{NC} = 0$, 45, and 90 deg. The linewidth of the high-frequency mode (a) becomes increasingly broader as the modes are spatially more separated. However, for the bullet mode (b) such a dependency is not observed. The critical angle for localization θ_L, is shown by dashed lines.

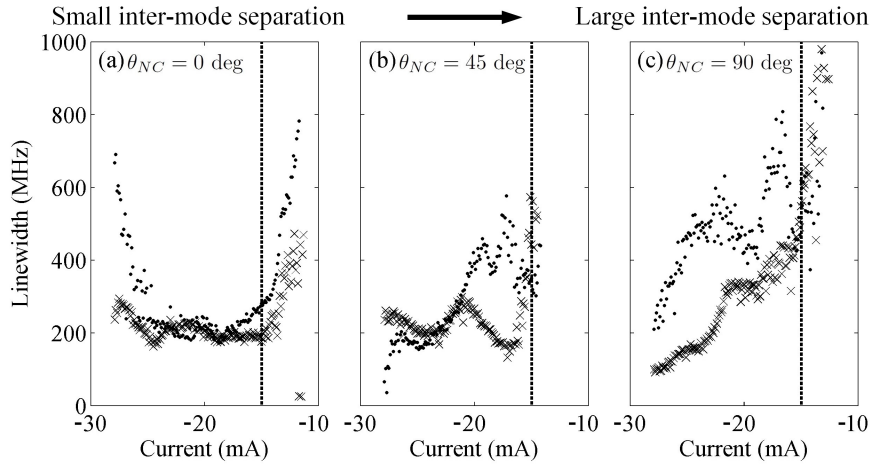

Figure 5.9: High-frequency mode generation linewidth of two devices at NC ellipse tilt angles $\theta_{NC} = 0$, 45, and 90 deg (dots and crosses) as a function of bias current. For all devices, the current threshold is approximately -15 mA (dashed lines), below which the linewidth follows the expected behavior of sub-threshold generation [118]. From the multi-mode theory, it can be interpreted that (a) the current and spatial separation are mostly balanced, (b) the current increases coupling in the range 20 to -25 mA while spatial separation is dominant in the range -20 to -25 mA, and (c) the current increases the coupling while the mode separation is negligible.

current. This is clear from the average generation power shown in Fig. 5.7 for each ellipse tilt. As the field angle increases towards θ_L (black dashed lines), the power of the high-frequency mode generally increases indicating a preferential energy share and the onset of mode-hopping dynamics. This feature is further confirmed by the linewidth, where an exponential divergence is observed in Ref. [43], consistent with the mode-hopping regime discussed in section 5.3.1. However, the different powers indicate that the condition of identical linewidths predicted by Eq. (5.9) is not strictly satisfied.

The linewidth estimation returns a wealth of results that can be interpreted from the analytical considerations of section 5.3.2. The first trend that can be observed is the increase in the high-frequency mode's linewidth for elliptical contacts tilted towards 90 deg, as shown in Fig. 5.8(a) for three devices biased at -20 mA. This is consistent with the expected trend in which spatially close modes ($\theta_{NC} = 0$) couple strongly and favor a minimal linewidth. However, the bullet mode [Fig. 5.8(b)] appears to be rather insensitive to this mechanism, indicating that there are intrinsic effects neglected in the analytical model. Indeed, as briefly stated above, the auto-oscillator framework is not directly applicable to localized modes, and the form of the damping terms must be revisited in order to agree with a more careful numerical solution of the resulting non-linear Schrödinger equation [121].

The experimental results of Fig. 5.8 emphasize that the inter-mode spatial separation [Fig. 5.6] is the main physical mechanism behind the linewidth broadening of the high-frequency mode. However, the analytical framework of section 5.3.2 predicts a significant reduction of such a linewidth as a function of the bias current, both due to the creation of coupling channels and the enhancement of the frequency mismatch between modes. Initial experiments suggest that this is indeed the case, as shown in Fig. 5.9. For the six measured devices (dots and crosses) the current threshold is approximately -15 mA, as indicated by black dashed lines. In all cases, the linewidth decreases as the current approaches the threshold due to the transition from a partially balanced damping scenario to an auto-oscillator regime [118]. For $\theta_{NC} = 0$ deg [Fig. 5.9(a)], where the modes are spatially close, the high-frequency mode linewidth of two devices only slightly increases above threshold (~ 30 MHz), indicating that the opposing actions of the current-induced coupling and spatial separation are mostly balanced. On the contrary, a dramatic decrease in linewidth is observed for $\theta_{NC} = 90$ deg [Fig. 5.9(c)], indicating that the current significantly enhances the inter-mode coupling via creation of coupling channels. The negligible effect of the current-induced inter-mode spatial separation in this regime also confirms their evanescent mode volume. An intermediate state can be observed for $\theta_{NC} = 45$ deg [Fig. 5.9(b)] where the behavior of the linewidth can be understood from a first increase of coupling channels [-20 to -25 mA] and a later inter-mode spatial separation [-25 to -28 mA]. However, more statistics are required to validate these observations.

In summary, the presented measurements are in qualitative agreement with the multi-mode oscillator theory predictions. From this point of view, it is possible to interpret a much wider set of data and predict the overall dynamical scenario. We stress that the presented results are taken from several devices in which sample-to-sample variation is inevitable. However, the consistency of these initial experiments is promising for more detailed studies in experimental setups where the field can be rotated in three dimensions and a larger data set can be acquired.

6

Confined magnetic dissipative droplet

The recent observation of magnetic dissipative droplets (droplets from here on) in NC-STOs [84] has opened up a new branch of research in which magnon condensates and the theory of dynamic magnetic solitons can be experimentally studied. From an applied perspective, such solitons are of particular interest as novel storage units.

Droplets have been theoretically predicted and experimentally observed only in two-dimensional thin films in which the physical boundaries have little impact in the nucleation process and dynamics. In light of the pursuit of nanoscopic excitations, we address in the following section the effect of physical confinement on a droplet, as the thin film is reduced to a nanowire. This problem is approached mainly numerically by micromagnetic simulations, however, asymptotic methods can be also analytically employed under certain approximations.

6.1 Physical confinement

The nucleation of droplets in NC-STO is achieved in free layers with strong PMA, such as Co/Ni multilayers [83, 84]. According to the dissipative droplet theory [58], droplets are successfully stabilized above a critical current where the number of magnons in the condensate increases exponentially. From this perspective, the nucleation of droplets in confined geometries should not be hindered. Additionally, the resulting dynamics are expected to be affected by the increased shape anisotropy in the free layer's plane.

In order to systematically study such effects, we perform micromagnetic simulations of NC-STO nanowires with a fixed length of 1 μm and a variable width between 300 and 50 nm. We choose material parameters consistent with the experiments performed on Co/Ni multilayers in Ref. [83] namely: thickness 5 nm, $\alpha = 0.05$, $K_u = 447$ kJ/m^3, $M_s = 716.2$ kA/m, and $A = 30$ pJ/m – similar to Co –. The Co polarizer is assumed to provide a torque with a full spin polarization $P = 1$ for simplicity, and a spin asymmetry $\lambda = 1.1$. This choice of polarization leads to an underestimation of the current-induced Oersted

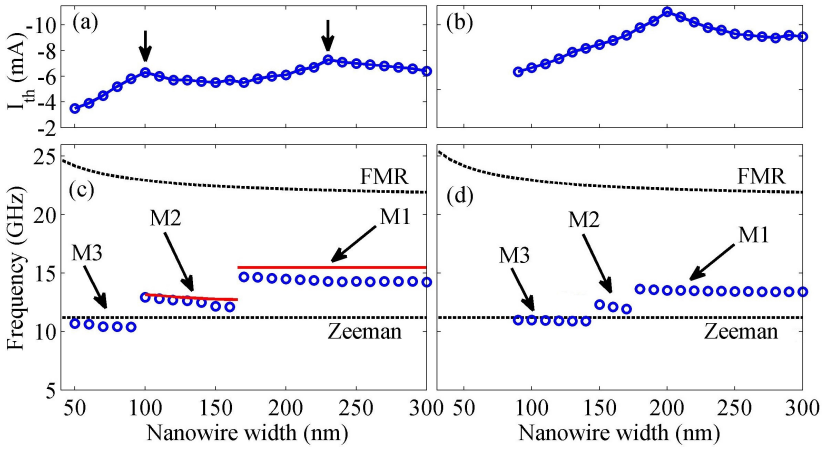

Figure 6.1: Threshold current for droplet nucleation for nanowires of varying width and NC diameter of (a) $d_1 = 50$ nm and (b) $d_2 = 90$ nm. The frequencies obtained at threshold are shown in (c) and (d) for the corresponding NC diameters. Three modes are identified: dissipative (M1), edge (M2), and quasi-1D (M3) droplet. The FMR and Zeeman frequencies are shown in black dashed lines. The analytically calculated frequencies for $d_1 = 50$ nm are shown in solid red lines in (c).

field. However, it can be shown that its effect is negligible [appendix C.1]. In all cases, the NC is placed in the geometrical center of the free layer.

6.1.1 Droplet nucleation

In order to nucleate a droplet, an out-of-plane external field of $\mu_o \vec{H}_a = 0.4$ T is applied. The current-dependent droplet nucleation is determined by sweeping the current in steps of 1 mA while seeking the satisfaction of the numerical condition $\langle m_z(t > 10 \text{ ns})\rangle_{NC} < 0$, where $\langle\cdot\rangle_{NC}$ indicates the average under the NC. This condition is motivated by the fact that 2D droplets always contain a significant portion of the magnetization pointing to the southern hemisphere, as indicated in Ref. [58]. From such simulations, we obtain the threshold currents of Fig. 6.1(a-b) for two NC diameters, namely $d_1 = 50$ nm and $d_2 = 90$ nm. Even though the general trend is an increase of current with nanowire width, current maxima can be observed as indicated by arrows. These features are related to standing spin-waves across the nanowire's perfect geometry, which preclude the onset of the modulational instability that gives rise to droplets [appendix C.2].

The frequency of the stable dynamics are determined from 200 ns time-traces sampled at ~ 10 ps. Three different modes can be identified *a priori* from Fig. 6.1(c-d). The frequencies of M1 and M2 lie between the FMR frequency, $\omega_o/2\pi = \gamma\mu_o(\vec{H}_a + \vec{H}_K - D_z\vec{M}_s)$, and the Zeeman frequency, $\gamma\mu_o\vec{H}_a$, both shown as black dashed lines. These frequency bounds coincide with those

for 2D droplets in extended thin films [58]. Contrarily, M3 exhibits a sub-Zeeman frequency which suggests a change in magnetic texture. This argument is based on the fact that the Zeeman and FMR conditions are defined for homogeneously magnetized textures so that a sub-Zeeman or "negative" frequency indicates that such an assumption is not strictly correct anymore.

In the following sections, we study the characteristics of the three identified modes from a spatial and topological perspective. The NC diameter $d_1 = 50$ nm is chosen as a representative case. However, the results presented here still hold and the dynamical modes still exist even when temperature is included [appendix C.3].

6.1.2 Non-topological droplet and edge modes

The spatial profiles of M1 and M2 are shown in Fig. 6.2(a-d) as contour plots for the m_z component and surface plots for the m_x component for the selected nanowires widths of 300 nm (M1) and 140 nm (M2). Clearly, M1 is the droplet discussed for 2D thin films, including its Oersted-induced asymmetric location with respect to the NC (white lines). Indeed, the simulated frequency agrees very well with the analytical estimate [red line in Fig. 6.1(c)]. In contrast, M2 exhibits a much larger footprint and "sticks" to the side of the nanowire. The in-plane magnetization components, represented by arrows in Fig. 6.2(a) and (c), also show that the magnetic texture of M2 is more complicated than for the droplet.

In order to elucidate the consequences of the different textures, the Skyrmion number is calculated according to Eq. (2.28). The discretization of the micromagnetic simulations introduces a finite error that precludes an integer Skyrmion number. However, by comparing with simulations using a finer mesh, it is verified that the Skyrmion number for both M1 and M2 is $\mathcal{N} = 0$. In other words, these structures are topologically trivial and we can justify an analytical treatment based on the dissipative droplet theory [58].

To analytically describe M2, the symmetry breaking Oersted and long-range demagnetizing fields can be neglected. The task is to solve the LLGS equation by considering free boundary conditions $\partial m/\partial \hat{n} = 0$ where $\hat{n}$ is an outward pointing normal. Starting from the assumption that the droplet is azimuthally symmetric, i.e. $m_{\text{droplet}} = m_{\text{droplet}}(\rho_C)$, we observe that $\partial m_{\text{droplet}}/\partial y|_{y=0} = 0$ along the droplet centerline. In other words, the solution of a half-plane also describes a droplet and, based on the droplet's exponential localization, can describe M2 for sufficiently wide nanowires [appendix C.4]. This is consistent with the picture of half droplets in analogy to previously studied conservative three-dimensional surface droplets. We thus refer to M2 as a droplet *edge mode*.

The asymptotic analysis presented in Ref. [58] can be used to derive the sustaining current, $\sigma(I)$, for which zero total energy loss (gain - loss balance)

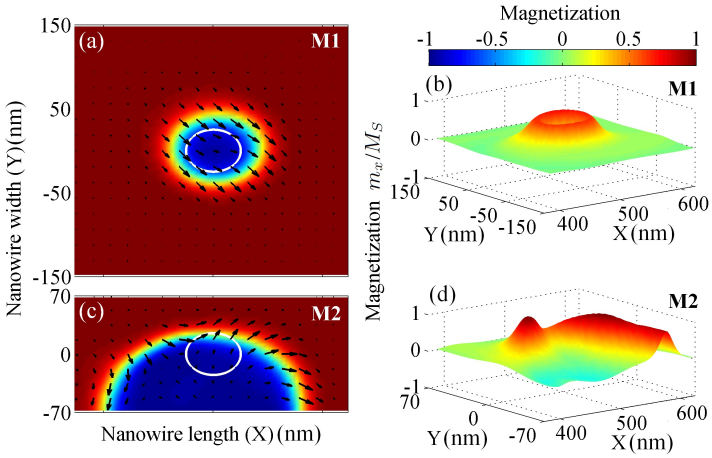

Figure 6.2: Spatial profile of the non-topological M1 (droplet) and M2 (edge mode) in nanowires of 300 nm and 140 nm, respectively. (a) and (c) are contour plots where the color scale represents the m_z component while the in-plane magnetization is represented by black arrows. (b) and (d) are surface plots of the m_x component.

is enforced, as required by all dissipative solitons

$$\frac{\sigma(I)}{\alpha} = -(\vec{H}_K/M_s - 1)[\omega' + \vec{H}_a/(\vec{H}_K - M_s)] \times \frac{\int_{y'>0} \sin^2\Theta(\vec{x}')d\vec{x}'}{\int\limits_{x'^2+(y'-\frac{w'}{2})^2<\frac{d'^2}{4}} \frac{\sin^2\Theta(\vec{x}')}{1+\nu\cos\Theta(\vec{x}')}d\vec{x}'}, \tag{6.1}$$

where it is convenient to use primed, nondimensional coordinates with lengths scaled by $\lambda_{ex}/\sqrt{\vec{H}_K/M_s - 1}$ and frequencies scaled by $\gamma\mu_o M_s^2/(\vec{H}_K - M_s)$. The droplet profile $\Theta = \Theta(\rho'_C)$ and shifted frequency $0 < \omega' < 1$ correspond to the ground state of the conservative 2D droplet equation $\omega' \sin\Theta = -\Theta'' - \Theta'/\rho'_C + \frac{1}{2}\sin 2\Theta$ [73]. Equation (6.1) gives the relationship between the sustaining current and frequency. The key difference between the edge mode and a 2D droplet is the denominator in Eq. (6.1) where the integral of the droplet is taken over the NC that is *offset* from the droplet centerline. Increasing the nanowire width w' while keeping the NC centered corresponds to a shift of the NC further away from the footprint of the edge mode. Therefore, to maintain a fixed sustaining current, a wider nanowire requires a larger droplet footprint, precisely what is observed in Fig. 6.2(b). Furthermore, it is known that wider droplets exhibit lower frequencies [58], explaining the frequency jump at the transition from M1 to the edge mode [Fig. 6.1(c)]. Since the threshold current is not an intrinsic property of the resulting mode, as evidenced by the 3.5% current variation at the M1-M2 transition [Fig. 6.1(a)],

we are justified in evaluating Eq. (6.1) and its 2D droplet counterpart [58] for the fixed current $I_{dc} = -5.7$ mA which provides *quantitative* agreement in frequency with the simulation results [solid red line in Fig. 6.1(c)].

As is the case for to 2D droplets, the existence of the edge mode is limited by a maximum sustaining current (recall that $I < 0$). Assuming negligible confinement effects, we theoretically determine the maximum sustaining current for the edge mode to fall below -5.7 mA for nanowires wider than 166 nm, almost precisely the width at which the M1 - M2 transition occurs [Fig. 6.1(a) and (c)]. However, theory also predicts a higher, width-independent maximum sustaining current for M1 (-3.3 mA) so that mode selection is not completely explained by this argument. Such a limitation suggests that a stability analysis is required to understand the selection condition between M1 and M2.

6.1.3 Topological quasi-one-dimensional mode

The spatial profile of M3 is shown in Fig. 6.3(a-b) for a nanowire of width 50 nm. In contrast to M1 and M2, magnetic boundaries are only established along the nanowire's length. Furthermore, it is observed that the in-plane component of the magnetization has opposite directions at any given time. In other words, the magnetization performs a 360 deg rotation as the texture is traversed longitudinally.

Topologically, it is clear that the Skrymion number of such a texture is zero as the magnetization would cover a unit circle instead of a sphere. This is expected, however, from one-dimensional textures as the definition of the Skyrmion number requires non-zero spatial derivatives in the plane. A fitting topological invariant in this case is the vector chirality [18], defined as

$$\vec{\mathcal{C}} = \frac{1}{\pi} \int_{-\infty}^{\infty} \mathrm{d}x' (\hat{m} \times \partial_{x'} \hat{m}). \tag{6.2}$$

Performing the integration of Eq. (6.2), leads to a time-dependent vector chirality with magnitude $|\vec{\mathcal{C}}| = 2$, indicating that the magnetization indeed covers the unit circle. This topological invariant indicates that M3 is a dynamical version of a soliton-soliton pair, which is a known soliton solution for integrable biaxial ferromagnets i.e., when the damping, STT, and symmetry breaking terms are neglected. Here, the biaxial character of the ferromagnet can be attributed to the in-plane demagnetizing factor arising from the nanowire's low dimensionality. Moreover, it can be understood that its precession below the Zeeman frequency is related to the development of chirality. We refer to this mode as the *quasi-1D* droplet.

To gain further insight into the properties of the quasi-1D droplet, we perform field-dependent simulations at $I_{dc} = -3.5$ mA. First of all, we find that the quasi-1D mode always exhibits a sub-Zeeman frequency with a field tunability of ~ 27 GHz/T [Fig. 6.3(c)]. Below $\mu_0 \vec{H}_a = 0.02$ T, the quasi-1D droplet is nucleated but its oscillation frequency eventually relaxes to zero.

An additional feature is observed as a function of field, namely, the spatial extent of the quasi-1D droplet varies periodically in time at its precessional frequency. As an example, Fig. 6.3(d) shows the averaged-in-y position

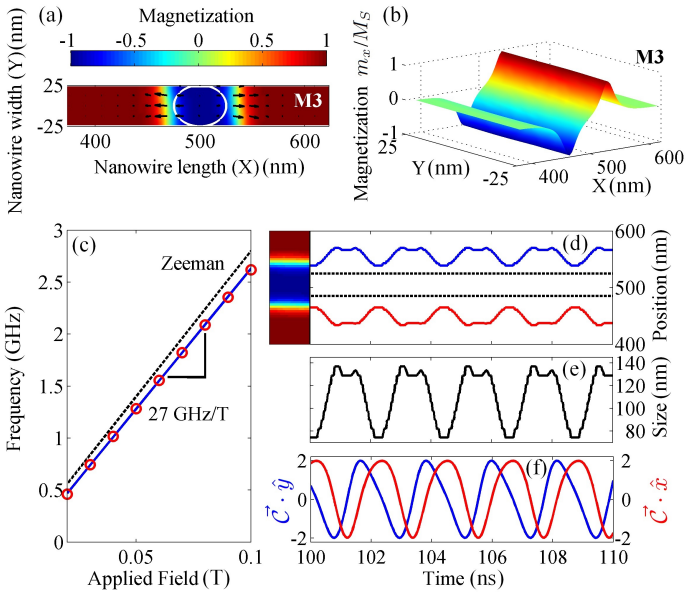

Figure 6.3: (a-b) Spatial profile of the topological M3 (quasi-1D droplet) in a nanowire of 50 nm. The contour plot (a) shows the m_z component in color scale while the in-plane magnetization is represented by black arrows. The surface plot of the m_x component is shown in (b). The quasi-1D droplet is stable down to 0.02 T and its frequency is linearly dependent on $\vec{H}_a$ (c). At 0.02 T, the position of the magnetic boundaries periodically moves in "anti-phase" (d) leading to a variation of its spatial extent or breathing (e). The precessional frequency originating from the magnetic boundaries is consistent with the likewise periodic in-plane chirality vectors (f).

of the domain boundaries in time when $\mu_o \vec{H}_a = 0.02$ T, determined when $\langle m_z(t) \rangle_w = 0$, where $\langle \cdot \rangle_w$ denotes averaging across the nanowire. The boundaries oscillate in "anti-phase", leading to a temporal variation, or breathing, of the quasi-1D droplet size [Fig. 6.3(e)]. Such a breathing solution is consistent with integrable soliton-soliton pairs in the zero field regime [73, 18] where breathing is described in terms of two bounded solitons in a periodic motion. In addition, the quasi-1D droplet exhibits a precessional motion of the magnetic boundaries, which is shown by the periodic form of the vector chirality [Fig. 6.3(f)]. Indeed, the relative phase between the $\hat{x}$ and $\hat{y}$ components denote a periodic transition between Néel- and Bloch-like configurations.

The aforementioned similarities between the quasi-1D droplet and the integrable soliton solution are attributed to the increased in-plane demagnetizing factor, which promotes an effective biaxial anisotropy in the nanowire. For this reason, qualitative agreement such as the observed chirality and breathing is expected. However, the inclusion of STT, damping, and field break the integrability of the LL equation. As a consequence, the breathing solution is

only achieved by including a finite perpendicular field. Furthermore, the exact soliton solution breathes at twice the precessional frequency, in contrast with the simulated results. Consequently, an analytical treatment based on breather modes where damping is compensated by STT and a finite field is taken into account is required to quantitatively reproduce these results.

7

Conclusions

Current-induced magnetodynamics in STOs are strongly non-linear owing to the large precession angles excited. Strictly speaking, such non-linear dynamics are not possible to represent analytically due to the initial assumption of small-amplitude precession, and the research must be performed either by numerical methods or experimentally. However, the analytical framework is able to provide predictions that aid in the understanding and interpretation of the real data. In this thesis, we studied three strongly non-linear magnetodynamics scenarios from an analytical perspective and related them to numerical simulations and experiments.

7.1 External perturbations

In the context of communication applications, STOs must be able both to synchronize in order to achieve enough output power and to be modulated in order to act as nanosized transceivers. The results of chapter 4 uncovered the particular limitations of these phenomena and, additionally, the possibility of modulation-mediated unlocking of phase-locked STOs. Such an unlocking is a consequence of the compromise between the non-Adlerian minimum synchronization time and the modulation bandwidth of the STO. Consequently, the presented results provide design guidelines for synchronized STOs in communication applications.

In the case of mutual synchronization, multiple NC-STOs sharing the same free layer are preferred over the electrically connected nanopillar STOs due to the fact that the delay can be tuned for stable and in-phase synchronization. Indeed, electrical synchronization has not been observed in feedback circuits experimentally due to their intrinsic instability. However, the power generated from such multiple NC-STOs is largely shunted by impedance mismatch as pointed out by Sani *et al.* [112], and such limitations have yet to be overcome experimentally. Apart from these considerations, the analytical theory describing modulation of NC-STO arrays can be simply extended by adding coupled equations. However, the solution rapidly escalates in difficulty and the condition for synchronization for more than two oscillators is not well defined leading to additional regimes of clustering and frustration [53, 26].

From a more fundamental point of view, the results of chapter 4 suggest a possible experimental setting to directly determine the non-Adlerian character of STOs. Recently, Rippard *et al.* [108] proposed an experimental procedure to measure the synchronization time of STOs and found that the non-Adlerian regime was not achieved under the experimental conditions. However, by the mechanism of resonant and non-resonant unlocking it would be possible to quantitatively determine the relevant auto-oscillator parameter Γ_p which is intrinsically related to the modulation bandwidth and minimum synchronization time, and thus provide unambiguous proof of non-Adlerian synchronization in these devices.

7.2 Multi-mode generation

The results of chapter 5 described the dynamical regimes that are possible to excite in STOs. In contrast to single mode theories, it was shown that STOs are generally multi-mode generators and the observation of a single mode is usually related to a dominant power share. From this point of view, it is completely natural to describe the experimentally observed phenomena of mode-hopping, coexistence, and periodic energy transfer.

In order to relate the theory with an experimental observable, the generation linewidth was derived, which is a quantity routinely measured experimentally. Our results quantitatively agree with experiments performed on NC-STOs exhibiting mode-hopping. Furthermore, we analytically revealed that the linewidth is related to temperature by means of the Arrhenius distribution of the mode-hopping events. This is not possible to derive from single mode theories as mode-hopping between energy minima is a required condition to physically explain such an effect.

In the case of coexistence, the multi-mode equations predict novel dependencies on the linewidth of the mostly-localized modes. Experimental measurements were performed on NC-STOs with elliptically shaped NCs in order to shed light onto such analytical predictions. It was found that the general trends follow the analytical predictions, such as the proportionality between current and K and the linewidth decrease as a function of K. However, these observations are indirect and more careful measurements are required in order to uncover the details and establish the limitations of the simplified multi-mode equations.

7.3 Topological droplets

The analytical prediction and experimental observation of dissipative droplets has opened up a new field of research for magnetic solitons and magnon condensates. In chapter 6 we studied the effect of physical confinement on the droplet, uncovering two novel modes: a non-topological edge mode and a topological quasi-1D droplet. The existence of the edge mode could be understood as a half droplet with the same nucleation condition as a regular droplet. Recent results [80] show that the droplet is attracted to free magnetic boundaries

while it is repelled from magnetically fixed boundaries. At the same time, the STT attracts the droplet [15], thus establishing a compromise that defined the transition width at which the edge mode is favored over a droplet. These mechanisms are relevant to control the edge mode and make experimental confirmation feasible.

The quasi-1D droplet demonstrates that the droplet could be a transient state towards a topological structure. This is a possibility because the condition for droplet nucleation involves the exponential increase in magnons thus leading to a nanoscopic increase in energy. Consequently, it is possible to smoothly surpass the energy protection of topological structures and fall into a new potential minimum. Along this line of thought, novel modes are expected also as a function of current for the edge mode. However, we argue that an additional symmetry-breaking field source is required to observe topological structures, such as strong demagnetizing factors in the plane, RKKY interaction, and even DMI [144].

8

Future Work

8.1 External perturbations

Synchronization of STOs is still a subject of active research and, consequently, the determination of intrinsic parameters related to the analytical framework is desirable. Among the interesting experiments that could be performed and related to the analytical results, we can suggest:

- Resonant excitation of phase-locked STOs to determine the possibility of modulation and the prediction of unlocking.
- Synchronization to noisy sources.
- Synchronization and modulation of NC-STOs arrays which must be developed in order to achieve enough generation power for any realistic application.
- Electrical synchronization of nanopillar STOs by a resonant feedback circuit, which has remained experimentally elusive in the last decade.

8.2 Multi-mode generation

Multi-mode generation offers a new perspective from which it is possible to study and interpret STOs. These ideas were recently introduced, leading to multiple improvements and research, such as:

- Improving the analytical framework to treat the temperature dependence of the fixed points position and the coupling factors.
- The fitting procedure can also be improved to fit Voigt functions and provide the ratio between the Lorentzian and Gaussian components.
- Uncover the relation between the coupling phase and the intrinsic STO parameters and how they are influenced by the different dynamical modes and STO geometries.
- In the case of coexistence, further measurements are required in order to test the analytical predictions, such as measurements of the low frequency components related to the coupling strength and injection locking experiments, where the linewidths should be identical in the case of strong coupling.

- The localization and shape of the modes must be understood better. This can be done numerically by studying the time dependence of the energy localization and its relation to the NC shape.

8.3 Topological droplets

The numerical prediction of confined topological droplets suggests novel structures that can be useful both for applications and fundamental research. However, the experimental confirmation of such droplets modes is of primary relevance. In particular, some experiments under development include:

- Droplet nucleation as a function of nanowire width in order to observe the numerical mode transitions. Such experiments must be accompanied by numerical simulations including temperature, surface roughness, and imperfections of the fabrication process.
- Control of the edge mode based on the competing attraction exerted by the free boundary conditions and the STT. A numerical study must be performed first to quantify the feasibility of different control methods.
- The nucleation of topological structures mediated by droplets is of high interest and impact. Consequently, the experimental observation of the quasi-1D droplet as well as its topological features is desired.
- The recent development of ultra-thin films on heavy metals exhibiting interfacial DMI suggests the study of STT-induced topological structures. Recent results by Zhou *et al.* [144] indicate that it is possible to nucleate a so-called droplet skyrmion, combining the dynamic properties of the droplet with the topological properties of the skyrmion. A detailed study of such an object is highly relevant for the development of the emerging field of spin-orbitronics [46].

Appendices

A

Manipulation with variable coefficients

A.1 Fourier series truncation

The Fourier series solution proposed in Eq. (4.13) is introduced into Eq. (4.11a). The term with the variable coefficient can be expanded using trigonometric identities:

$$\begin{aligned} \cos(\omega_m t)\delta p &= A_0 \cos(\omega_m t) \\ &+ \sum_{n=1}^{\infty} \frac{A_n}{2}[\sin(\omega_m(1+n)t) - \sin(\omega_m(1-n)t)] \\ &+ \frac{B_n}{2}[\cos(\omega_m(1+n)t) + \cos(\omega_m(1-n)t)]. \end{aligned} \tag{A.1}$$

Expanding the summation and rearranging for equal harmonics yields

$$\begin{aligned} \cos(\omega_m t)\delta p &= (A_0 + \frac{B_1}{2}) \\ &+ \frac{1}{2}[(2B_2 A_0)\cos(\omega_m t) - A_2 \sin(\omega_m t)] \\ &+ \frac{1}{2}\sum_{n=2}^{\infty}(A_{n-1} - A_{n+1})\sin(n\omega_m t) \\ &+ \frac{1}{2}\sum_{n=2}^{\infty}(B_{n-1} + B_{n+1})\sin(n\omega_m t). \end{aligned} \tag{A.2}$$

This expression treats the harmonics separately, so that Eq. (4.11a) can be solved by collecting harmonic terms. The resulting system of equations for

the harmonic dependent coefficients is

$$
\begin{aligned}
0 &= \mu\frac{C_2}{2}B_1 + 2\Gamma_p A_0, && \text{(A.3a)}\\
\omega_m A_1 &= \mu(C_1 - C_2 A_0 - \frac{C_2}{2}B_2) - 2\Gamma_p B_1, && \text{(A.3b)}\\
\omega_m B_1 &= 2\Gamma_p A_1 - \mu\frac{C_2}{2}A_2, && \text{(A.3c)}\\
0 &= \sum_{n=2}^{\infty} 2\Gamma_p B_n + n\omega_m A_n && \text{(A.3d)}\\
&\quad +\mu\frac{C_2}{2}(B_{n-1} - B_{n+1}),\\
0 &= \sum_{n=2}^{\infty} 2\Gamma_p A_n - n\omega_m B_n && \text{(A.3e)}\\
&\quad +\mu\frac{C_2}{2}(A_{n-1} - A_{n+1}).
\end{aligned}
$$

This system of equations can be solved by truncating the Fourier series. Numerically, the problem reduces to simple matrix algebra which is easily solved by commercial packages, such as MATLAB. The convergence rate for two modulation frequencies is shown in Fig. A.1(a), where it is assumed that 20 harmonics represent the true solution. It is observed that 5 harmonics return an error below 10^{-5} %.

Based on such a rapid convergence, an analytical solution can be obtained by further assuming that the coefficients decrease rapidly in amplitude. Consequently, it is possible to express the coefficients as a recursive function given by

$$
\begin{aligned}
A_1 &= \mu_m\frac{\Gamma_-(p_o)\omega_m}{\omega_m^2 + (2\Gamma_p)^2}, && \text{(A.4a)}\\
B_1 &= \mu_m\frac{\Gamma_-(p_o)2\Gamma_p}{\omega_m^2 + (2\Gamma_p)^2}, && \text{(A.4b)}\\
A_n &= -\frac{C_2}{2}\left(\frac{2\Gamma_p A_{n-1} + n\omega_m B_{n-1}}{(n\omega_m)^2 + (2\Gamma_p)^2}\right), && \text{(A.4c)}\\
B_n &= \frac{C_2}{2}\left(\frac{n\omega_m A_{n-1} + 2\Gamma_p B_{n-1}}{(n\omega_m)^2 + (2\Gamma_p)^2}\right). && \text{(A.4d)}
\end{aligned}
$$

The evaluation of Eq. (A.4) returns a good convergence for 5 harmonics [Fig. A.1(b-c)]. However, as β_1 is swept, the error increases towards the minimum of the first sideband (indicated by a dashed line). It is noteworthy that the maximum error in Fig. A.1(c) is slightly shifted due to the absence of the higher harmonics in the recursive generation function. In spite of these limitations, this approach is convenient to treat different problems analytically.

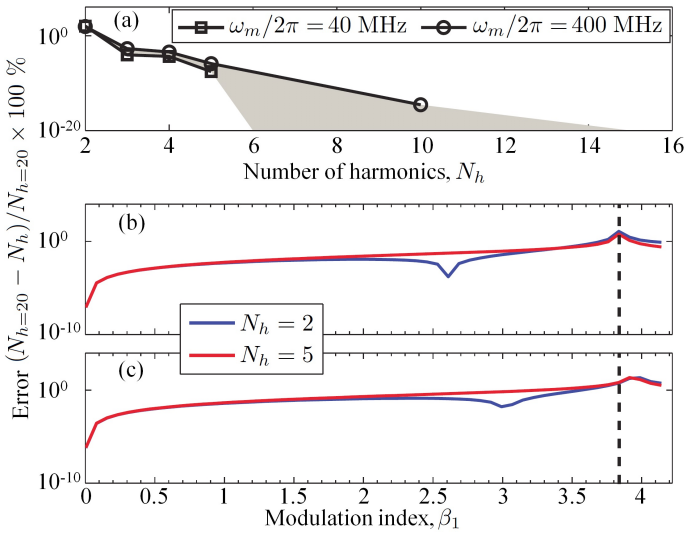

Figure A.1: (a) Total error as a function of the number of harmonics N_h in the series, calculated from the linear equations Eq. (A.3). For $N_h \geq 5$, the error is assumed to be negligible. Two modulation frequencies are shown as limiting cases. For intermediate frequencies, the error lies in the shaded area. (b-c) Error between the linear set of equations and the recursive method as a function of the modulation index β_1. The modulation frequencies for each case are 40 and 400 MHz. The error introduced by the recursive method is generally small, but diverges close to the minimum of the sideband, which is indicated by vertical dashed lines.

A.2 NFAM power spectral density

The power spectral density (PSD) of the proposed solution is obtained from Eq. (4.14), which defines both time-dependent power and phase variations. The PSD is defined as

$$PSD = p_0 * \left| \hat{f}(1 + \delta_K p) * \hat{f}(\cos(\phi)) \right|, \tag{A.5}$$

where $\hat{f}$ is the Fourier transform. Below, we perform each Fourier transform separately, and express the result as a convolution. The first term on the RHS has the form of non-linear amplitude modulation. The phase introduced by the sinusoidal functions allows us to define the complex variable $X_n = B_n + iA_n$, so that

$$\begin{aligned} \hat{f}(1 + \delta_K p) \quad &= \quad (1 + A_0)\delta_K(0) \\ &\quad + \sum_{n=1}^{\infty} \frac{\bar{X}_n}{2}\delta_K(n\omega_m) + \frac{X_n}{2}\delta_K(-n\omega_m), \end{aligned} \tag{A.6}$$

where the notation $\delta_K(x_0) = \delta_K(x - x_0)$ is used and δ_K is the Kronecker delta function.

The second term on the RHS of Eq. (A.5) is calculated by using Euler's formulae, and subsequently expanding in Taylor series. We obtain

$$\begin{aligned}\cos(\phi) &= \frac{e^{-i\omega}}{2}\prod_{n=1}^{\infty}\Big(\sum_{k=0}^{\infty}\frac{(b_n-ia_n)^k}{k!2^k}e^{ink\omega_m t} \\ &\cdot \sum_{k=0}^{\infty}(-1)^k\frac{(b_n+ia_n)^k}{k!2^k}e^{ink\omega_m t}\Big)+c.c, \end{aligned} \tag{A.7}$$

where $a_n = 2\nu\Gamma_p A_n/(n\omega_m)$, $b_n = 2\nu\Gamma_p B_n/(n\omega_m)$, and $c.c$ is the complex conjugate. The two summations can be multiplied by expanding and rearranging the terms. Defining $2x_n = b_n + ia_n$, it is possible to rewrite the product terms as

$$\begin{aligned}\prod_{n=1}^{\infty}(\cdot) &= \sum_{k=0}^{\infty}(-1)^k\frac{x_n\bar{x_n}}{k!k!} \\ &+ \sum_{k=0}^{\infty}\sum_{j=1}^{\infty}(-1)^k\frac{x_n\bar{x_n}}{k!(k+j)!}\left[(\bar{x_n}e)^j+(-x_ne^{-1})^j\right]. \end{aligned} \tag{A.8}$$

From this expression, we can identify the summations on k as Bessel functions of order j and argument $\beta_n = 2\sqrt{x_n\bar{x_n}}$ (upon renormalization of the coefficients by $\beta_n/2$). The product takes the form

$$\begin{aligned}\prod_{n=1}^{\infty}(\cdot) &= J_0(\beta_n) \\ &+ \sum_{j=1}^{\infty}\frac{2J_j(\beta_n)}{\beta_n}\left[(\bar{x_n}e)^j+(-x_ne^{-1})^j\right]. \end{aligned} \tag{A.9}$$

The Fourier transform of Eq. (A.9) is easily performed by expressing the result as a product of convolutions Eq. (4.15).

B

Multi-mode theory and generation linewidth

B.1 Derivation of the coupled equations from auto-oscillator theory

The auto-oscillator equation [118] taking into account thermal fluctuations and a coupling term to another oscillator, can be written as

$$\dot{c_i} + i\omega_i(|c_i|^2)c_i + \left[\Gamma_+(|c_i|^2) - \Gamma_-(|c_i|^2)\right] c_i = \tilde{f}(t) + c_j K e^{i\phi_c}, \tag{B.1}$$

where the subscripts i and j identify each oscillator, c is the mode's complex amplitude, and ϕ the mode's phase. The perturbation term $\tilde{f}(t)$ represents thermal fluctuations while the coupling term to the j-th mode is parameterized by a strength K and phase ϕ_c. For the multi-modal model equations the transformation $\bar{Q}_i^2 = \omega_i |c_i|^2$ is performed under the assumption of conserved total power $p = p_1 + p_2$ [88]. Separating real and imaginary parts of Eq. (B.1), four coupled equations are obtained

$$\begin{aligned}
\dot{Q}_i &= Q_i \Gamma_G (\xi - 1) \\
&\quad - Q_i \Gamma_G \left[\frac{(\bar{Q}_i + \xi \bar{P}_i)}{\omega_i} Q_i^2 + \frac{(\bar{Q}_0 + \xi \bar{P}_0)}{\omega_j} Q_j^2 \right] \\
&\quad + Q_j K \sqrt{\frac{\omega_i}{\omega_j}} \cos\left(\phi_c + \phi_j - \phi_i\right) + f_i^R, \qquad \text{(B.2a)} \\
\dot{\phi}_i &= \omega_o + \frac{N Q_i}{\omega_i} \\
&\quad + K \frac{Q_j}{Q_i} \sqrt{\frac{\omega_i}{\omega_j}} \sin\left(\phi_c + \phi_j - \phi_i\right) + f_i^I. \qquad \text{(B.2b)}
\end{aligned}$$

Furthermore, energy can be mapped into the variable $|\theta| \leq \pi/2$ by performing the mode-dependent transformations $\bar{Q}_1 = \sqrt{p}\cos(\theta/2 + \pi/4)$ and $\bar{Q}_2 = \sqrt{p}\sin(\theta/2 + \pi/4)$. Scaling Eq. (B.2a) by $\sin\theta$ and $\cos\theta$ for each mode, we add Eq. (B.2a) to obtain a differential equation for θ, whereas we subtract Eq. (B.2b) to obtain a differential equation for the phase difference, $\psi = \phi_2 - \phi_1$.

B.2 Linear stability analysis

For the linear stability analysis, the Jacobian of the model equations Eq. (5.2) is calculated. Consequently, the fixed point's stability is provided by $s < 1$, where the determinant is

$$\begin{aligned} s &= \frac{J_\theta(\theta) + J_\psi(\psi)}{2} \\ &\pm \left[\left(\frac{J_\theta(\theta) - J_\psi(\psi)}{2} \right)^2 + J_\psi(\theta) J_\theta(\psi) \right]^{1/2}. \end{aligned} \tag{B.3}$$

For the limit $K \to 0$, Eq. (B.3) simply reduces to the mode-independent stability conditions $\bar{Q}_i + \xi \bar{P}_i < \bar{Q}_0 + \xi \bar{P}_0$. On the other hand, when $K > 0$ the fixed points are given by $\theta = n\pi$ and $\psi = m\pi$ for $n, m = 0, 1, 2, ...$ The determinant for this case can be written as

$$\begin{aligned} s &= \frac{Y_1 - (-1)^{n+m} 2K\beta_1}{2} \\ &\pm \sqrt{\frac{Y_1^2}{4} - K^2\beta_2^2 - (-1)^{n+m} Y_2 K \beta_2}, \end{aligned} \tag{B.4}$$

where we use $Y_1 = \Gamma_G p/2 \left[X_1 \omega_1^{-1} - X_2 \omega_2^{-1} \right]$, $X_i = \bar{Q}_i - \bar{Q}_0 + \xi(\bar{P}_i - \bar{P}_0)$, $Y_2 = pN_0/2 \left[\omega_1^{-1} + \omega_2^{-1} \right]$, $\beta_1 = \left(a^{-1} + a \right) \cos \phi_c$, $\beta_2 = \left(a^{-1} + a \right) \sin \phi_c$, and $a = \sqrt{\omega_1/\omega_2}$. In general, the stable state is observed to be closely related to the coupling phase, ϕ_c. We can further look into two limiting cases. If $\phi_c = \pi/2$, $\beta_1 = 0$, and $\beta_2 \neq 0$, the determinant of Eq. (B.4) can be both imaginary or real for even or odd values of $n+m$. Consequently, this case demonstrates the possibility of limit cycles. On the other hand, if $\phi_c = l\pi$ (where $l = 0, 1, 2, ...$), $\beta_1 = (-1)^l \left(a^{-1} + a \right)$, and $\beta_2 = 0$, the solutions are always real. Consequently, coexistent states are stable (unstable) if $n + m + l$ is even (odd).

B.3 Derivation of the autocorrelation function

The autocorrelation function $\mathcal{K} = \langle [c_1(t) + c_2(t)] [c_1^*(t') + c_2^*(t')] \rangle$ can be expanded by mapping the complex amplitudes into the variables θ and ψ. Noting that $c_i = \sqrt{p_i} e^{i\psi_i}$ and introducing the variables $\Psi = \phi_1 + \phi_2$ and $\chi = \theta/2 + \pi/4$, we can expand the complex amplitudes to $c_1 = \sqrt{p} \cos [\chi(t)] e^{i[\Psi(t) - \psi(t)]/2}$ and $c_2 = \sqrt{p} \sin [\chi(t)] e^{i[\Psi(t) + \psi(t)]/2}$. Here, we explicitly write the time dependencies of the variables. It is assumed that the average energy of each mode can be parametrized by $\pm\langle\theta_o\rangle$ so that $\langle \cos [\chi(t)] \rangle = \cos \langle \chi \rangle$ and $\langle \sin [\chi(t)] \rangle = \sin \langle \chi \rangle$. Consequently, the autocorrelation can be expressed as

$$\begin{aligned} \mathcal{K} &= p \cos^2 \langle \chi \rangle e^{i\Psi/2} \langle e^{-i[\psi(t) - \psi(t')]/2} \rangle \\ & \quad p \sin^2 \langle \chi \rangle e^{i\Psi/2} \langle e^{i[\psi(t) - \psi(t')]/2} \rangle \\ & \quad \frac{p}{2} \sin 2\langle \chi \rangle e^{i\Psi/2} \langle e^{-i[\psi(t) + \psi(t')]/2} \rangle \\ & \quad \frac{p}{2} \sin 2\langle \chi \rangle e^{i\Psi/2} \langle e^{i[\psi(t) + \psi(t')]/2} \rangle. \end{aligned} \tag{B.5}$$

Expanding the exponential functions then leads to the known property for stochastic functions

$$\langle e^{i\psi(t)} \rangle = e^{-\langle \psi(t)^2 \rangle / 2}. \tag{B.6}$$

Without loss of generality, one can assume $t' = 0$ so that $\langle \psi(t')^2 \rangle = \langle \psi(t') \rangle^2$. Consequently, the averages contribute as an additional proportionality constant whereas the lineshape originates from the form of the second moment $\langle \psi(t)^2 \rangle$. The latter provides the relevant information on the lineshape and linewidth and we neglect the proportionality factors for the analytical discussion of chapter 5.

For the case of generally different frequencies, we apply Galilean invariance, so that $\Psi = 2\Omega t + \Psi_o$ and $\psi = \Delta\omega + \psi_o$, where $\Omega = (\phi_2 + \phi_1)/2$ is the average frequency. With the assumption that $\Psi \to \Omega t$ is large, we can write $\psi = \Delta\omega + \psi_o + \delta\psi$ for the phase fluctuations. Consequently, the frequencies in the autocorrelation remain separated and we obtain Eq. (5.8), restated here for clarity

$$\begin{aligned} \mathcal{K} &= p e^{i\omega_1 t} \left(\cos^2 \langle \chi \rangle + \frac{\sin(2\langle \chi \rangle)}{2} \right) e^{-\langle \psi(t)\psi(t') \rangle / 2} \\ &+ p e^{i\omega_2 t} \left(\sin^2 \langle \chi \rangle + \frac{\sin(2\langle \chi \rangle)}{2} \right) e^{-\langle \psi(t)\psi(t') \rangle / 2}. \end{aligned} \tag{B.7}$$

B.4 Derivation of the coupled perturbed model equations

The short time-scale fluctuations can be obtained by linearizing Eq. (5.2). This can be achieved directly from Eq. (B.2) by expanding the power and phase as $p = p_o + \delta p$ and $\psi = \psi_o + \delta\psi$, where p_o and ψ_o are average operating points. Keeping only the perturbation terms leads to

$$\dot{\delta p} = C_{pp}\delta p + C_{p\psi}\delta\psi + f_p, \tag{B.8a}$$

$$\dot{\delta\psi} = C_{\psi p}\delta p + C_{\psi\psi}\delta\psi + f_\psi. \tag{B.8b}$$

where the coefficients are given by

$$
\begin{aligned}
C_{pp} &= 2\Gamma_G(\xi-1) - \frac{p_o}{2}\Gamma_G\frac{\left(\bar{Q}_1+\xi\bar{P}_1\right)}{\omega_1}\left(1-\sin\langle\theta_o\rangle\right)^2 && \text{(B.9a)}\\
&\quad -\frac{p_o}{2}\Gamma_G\frac{\left(\bar{Q}_2+\xi\bar{P}_2\right)}{\omega_2}\left(1+\sin\langle\theta_o\rangle\right)^2\\
&\quad -\frac{p_o}{2}\Gamma_G\left(\bar{Q}_0+\xi\bar{P}_0\right)\left(\frac{1}{\omega_1}+\frac{1}{\omega_2}\right)\left(1-\sin^2\langle\theta_o\rangle\right)\\
&\quad +K\cos\langle\theta_o\rangle\left[a\cos\left(\phi_c+\psi\right)+\frac{1}{a}\cos\left(\phi_c-\psi\right)\right],\\
C_{p\psi} &= p_oK\cos\langle\theta_o\rangle\left[a\sin\left(\phi_c+\psi\right)-\frac{1}{a}\sin\left(\phi_c-\psi\right)\right], && \text{(B.9b)}\\
f_p &= \sqrt{2p_o}\left[\cos\langle\frac{\theta_o}{2}\rangle(f_2^R+f_1^R)+\sin\langle\frac{\theta_o}{2}\rangle(f_2^R-f_1^R)\right], && \text{(B.9c)}\\
C_{\psi p} &= -\frac{N_0}{2}\left[\frac{1+\sin\langle\theta_o\rangle}{\omega_2}-\frac{1-\sin\langle\theta_o\rangle}{\omega_1}\right], && \text{(B.9d)}\\
C_{\psi\psi} &= -\frac{K}{\cos\langle\theta_o\rangle}\left[\left(1-\sin\langle\theta_o\rangle\right)\frac{1}{a}\cos\left(\phi_c-\langle\psi\rangle\right)\right] && \text{(B.9e)}\\
&\quad -\frac{K}{\cos\langle\theta_o\rangle}\left[\left(1+\sin\langle\theta_o\rangle\right)a\cos\left(\phi_c+\langle\psi\rangle\right)\right],\\
f_\psi &= \sqrt{\frac{2}{p_o}}\left[\frac{\cos\langle\frac{\theta_o}{2}\rangle(f_2^I-f_1^I)-\sin\langle\frac{\theta_o}{2}\rangle(f_2^I+f_1^I)}{\cos\langle\theta_o\rangle}\right]. && \text{(B.9f)}
\end{aligned}
$$

Note that Eq. (B.9e) and Eq. (B.9f) diverge if $\cos\langle\theta_o\rangle = \pi/2$. Such a divergence is understandable due to the fact that a purely single mode oscillation leads to an ill-defined phase difference.

B.5 General solution of the coupled perturbed model equations

The coupled set of Eq. (5.4) can be generally solved by the method of variation of parameters. By matrix algebra, one can find the eigenvalues $\lambda_{\pm,i}$ and the eigenvector matrix elements η_i with inverse matrix components η_i' for each mode and solution. Consequently, we can write the temporal solution for $\psi(t)$ as

$$
\begin{aligned}
\psi_i(t) &= \psi_o && \text{(B.10)}\\
&+ \eta_{12,i}e^{\lambda_{+,i}t}\int_0^t \eta'_{11,i}e^{-\lambda_{+,i}t'}f_p(t')+\eta'_{21,i}e^{-\lambda_{+,i}t'}f_\psi(t')dt'\\
&+ \eta_{22,i}e^{\lambda_{-,i}t}\int_0^t \eta'_{12,i}e^{-\lambda_{-,i}t'}f_p(t')+\eta'_{22,i}e^{-\lambda_{-,i}t'}f_\psi(t')dt'.
\end{aligned}
$$

From Eq. (5.4) it is possible to obtain the self- and cross-correlation phase difference second moments by simple integration. Noting that

$$\langle f_p(t) f_p(t') \rangle = 4p^2 \Delta\omega \delta(t-t'), \tag{B.11a}$$

$$\langle f_\psi(t) f_\psi(t') \rangle = \frac{4\Delta\omega}{\cos^2\langle\theta_o\rangle} \delta(t-t'), \tag{B.11b}$$

$$\tag{B.11c}$$

we obtain the second moments as a function of $|\tau| = |t'-t|$

$$\begin{aligned} \langle \psi_i(t)\psi_i(t') \rangle &= \frac{A_{ii}}{2\lambda_{+,i}} e^{-\lambda_{+,i}|\tau|} + \frac{B_{ii}}{2\lambda_{-,i}} e^{-\lambda_{-,i}|\tau|} \\ &\quad + C_{ii} \frac{e^{-\lambda_{-,i}|\tau|} + e^{-\lambda_{+,i}|\tau|}}{\lambda_{+,i} + \lambda_{-,i}}, \end{aligned} \tag{B.12a}$$

$$\begin{aligned} \frac{\langle \psi_i(t)\psi_j(t') \rangle}{\cos\langle\theta_o\rangle} &= \frac{A_{ij}}{\lambda_{+,i} + \lambda_{+,j}} e^{-\lambda_{+,j}|\tau|} + \frac{B_{ij}}{\lambda_{-,i} + \lambda_{-,j}} e^{-\lambda_{-,j}|\tau|} \\ &\quad + \frac{C_{ij} e^{-\lambda_{-,j}|\tau|} + C_{ji} e^{-\lambda_{+,i}|\tau|}}{\lambda_{+,i} + \lambda_{-,j}}, \end{aligned} \tag{B.12b}$$

where the coefficients are given by

$$A_{ij} = 4\Delta\omega \eta_{12,i}\eta_{12,j} \left[\eta'_{11,i}\eta'_{11,j} p^2 + \frac{\eta'_{21,i}\eta'_{21,j}}{\cos^2\langle\theta_o\rangle} \right], \tag{B.13a}$$

$$B_{ij} = 4\Delta\omega \eta_{22,i}\eta_{22,j} \left[\eta'_{12,i}\eta'_{12,j} p^2 + \frac{\eta'_{22,i}\eta'_{22,j}}{\cos^2\langle\theta_o\rangle} \right], \tag{B.13b}$$

$$C_{ij} = 4\Delta\omega \eta_{12,i}\eta_{22,j} \left[\eta'_{11,i}\eta'_{12,j} p^2 + \frac{\eta'_{21,i}\eta'_{12,j}}{\cos^2\langle\theta_o\rangle} \right]. \tag{B.13c}$$

The exponential function of Eq. (B.12) can be further expanded to second order in $|\tau|$, from which we obtain the Lorentzian and Gaussian coefficients

$$\begin{aligned} 2\gamma_{L,ij} &= \frac{A_{ij}\lambda_{+,j}}{\lambda_{+,i} + \lambda_{+,j}} + \frac{B_{ij}\lambda_{-,j}}{\lambda_{-,i} + \lambda_{-,j}} \\ &\quad + \frac{C_{ij}\lambda_{-,j} + C_{ji}\lambda_{+,i}}{\lambda_{+,i} + \lambda_{-,j}}, \end{aligned} \tag{B.14a}$$

$$\begin{aligned} -4\gamma_{G,ij} &= \frac{A_{ij}\lambda_{+,j}^2}{\lambda_{+,i} + \lambda_{+,j}} + \frac{B_{ij}\lambda_{-,j}^2}{\lambda_{-,i} + \lambda_{-,j}} \\ &\quad + \frac{C_{ij}\lambda_{-,j}^2 + C_{ji}\lambda_{+,i}^2}{\lambda_{+,i} + \lambda_{-,j}}. \end{aligned} \tag{B.14b}$$

B.6 Estimate of the energy barrier from experimental data

In this section we refer to the experimental results obtained in Ref. [89] for a nanocontact STO. The same reference experiment was used throughout

section 5.3.1 for the analytical and numerical calculations. For our analytical estimate, we assume that the linewidth close to a mode transition can be fully described by the mode-hopping rate. Such an assumption implies that the linewidth "floor" obtained from a single-mode autocorrelation [black marks in Fig. 5.3(b)] is negligible in the temperature range of the fit [Fig. 5.3(c)].

In the reference experiment, the linewidth was determined as a function of temperature at a bias current, close to a mode transition, of 28.4 mA. For this particular bias current, a linewidth of 22.2 MHz was experimentally measured at 303 K. From this single data point, we attempt to estimate the temperature dependence of the linewidth. Assuming the numerically obtained attempt frequency, $f_a = 160$ MHz, it is possible to estimate the energy barrier $\Delta E \approx 52$ meV at 303 K, using Eq. (5.7). The same equation can be used to estimate the temperature dependence of the linewidth, shown in Fig. 5.3(c).

The performed estimate describes semi-quantitatively the experimental results and the agreement is remarkably good for such a simple estimation. We stress that the estimate described above implicitly assumes that the energy barrier is constant as a function of temperature, which can be an oversimplification. Indeed, we observe from experiments that the energy barrier deviates by up to 30% as a function of temperature. Consequently, careful measurements are needed in order to reliably extract ΔE and λ.

C

Droplet confinement

C.1 Effect of the current-induced Oersted field

The Oersted field has a negligible impact on droplet nucleation and dynamics in confined geometries. Since the existence of the quasi-1D droplet is one of the main results in this geometry, we perform simulations that include (blue) and neglect (red) the Oersted field in such a regime. The effect of the Oersted field for 2D droplets has been already studied in detail by Hoefer *et al.* [58].

First, we perform simulations at the threshold current and out-of-plane applied field $\mu_o \vec{H}_a = 0.4$ T. In this case, the quasi-1D droplet nucleates and the Oersted field slightly shifts the frequency by $\Delta f_d = 10$ MHz, as observed in the spectra of Fig. C.1(a). A similar simulation is performed at an applied field of $\mu_o \vec{H}_a = 0.02$ T. The results also show a frequency shift induced by the Oersted field, $\Delta f_d = 40$ MHz [Fig. C.1(b)]. One can also observe a reduction of the linewidth, as expected for a symmetric excitation. However, the most interesting result is that the quasi-1D droplet nucleates regardless of the inhomogeneity introduced by the Oersted field, even when its peak value (~ 0.028 T at the NC boundary) is higher than the applied field.

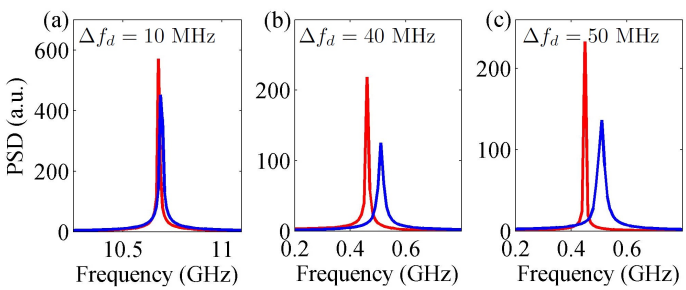

Figure C.1: Spectra of the quasi-1D droplets at (a) threshold and 0.4 T, (b) threshold and 0.02 T, and (c) well above threshold (-5 mA) and 0.02 T. Each panel shows the results with (blue) and without (red) the current-induced Oersted field. In all cases, the Oersted field is found to produce a frequency shift, Δf_d.

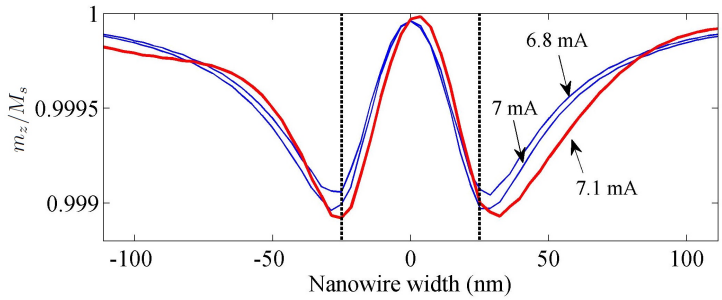

Figure C.2: Standing waves on a 230 nm wide nanowire as a function of current, parameterized by $\langle m_z(t)\rangle_c/M_s$, where $\langle\cdot\rangle_c$ is the time average on each cell of the centerline. The black dashed lines indicate the edges of the NC.

Lastly, we compare simulations including and neglecting the Oersted field when the applied field is $\mu_o\vec{H}_a = 0.02$ T and the current is above threshold (-5 mA). In this case, the Oersted field is significantly stronger (~ 0.04 T) than the applied field. However, the induced frequency shift is similar to the case at threshold as shown in Fig. C.1(c), $\Delta f_d = 50$ MHz. Again, the quasi-1D droplet nucleation is not hindered by the Oersted field, showing that its impact is negligible on the observed results discussed in the main text.

C.2 Resonant spin-waves

A dissipative droplet is nucleated when the condition of modulational instability is achieved, i.e., when the growth of the spin wave amplitude is unbounded [58]. In the case of nanowires, the lateral confinement introduces reflections across its width, effectively leading to standing waves that prevent its unbounded growth. This can be clearly observed by the average $\langle m_z(t)\rangle_c/M_s$ across the nanowire as a function of current, where $\langle\cdot\rangle_c$ is time average on each cell of the centerline. We select a nanowire of width 230 nm and a NC diameter $d = 50$ nm, where a current threshold maximum was observed [Fig. 6.1(a)].

Below threshold ($I_{dc} > -7.3$), standing waves are established across the nanowire [Fig. C.2]. By increasing the current, the wavelength of the spin waves changes due to the dispersion relation of the media until the standing wave condition breaks at threshold. In Fig. C.2 the blue lines are obtained for $I_{dc} = -6.8$ and -7 mA. The standing wave is centered with respect to the nanowire width and the NC (black dashed lines). For $I_{dc} = -7.1$ mA the standing wave starts to distort as shown by the red curve. These standing wave conditions are expected to be smoothed out or simply vanish in real samples, where both temperature and roughness play important roles.

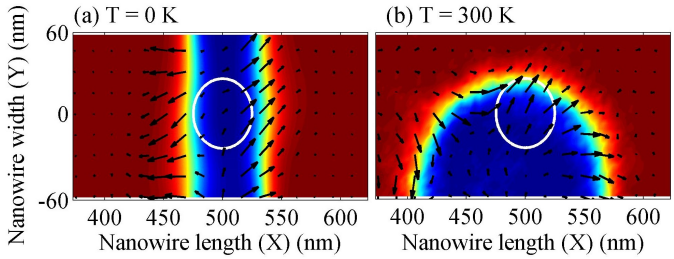

Figure C.3: (a) Resonant M3 observed for a nanowire width of 120 nm and NC diameter of 50 nm when no thermal fluctuations are taken into account. (b) Including thermal fluctuations stabilizes the expected edge mode indicating that the resonant M3 mode is a numerical artifact.

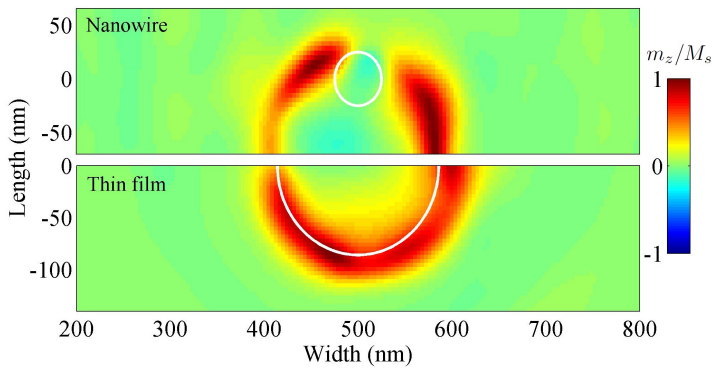

Figure C.4: Contour plots of the m_y component of the edge mode on a 140 nm wide nanowire and a 2D droplet on an extended thin film. The NC circumference for each case are shown by white lines. The lower panel only shows half of the simulation area for comparison. Clearly, both independent simulations are complementary, confirming that the edge mode can be pictured as half a 2D droplet.

C.3 Effect of temperature

The fluctuations caused by temperature must be taken into account when striving to obtain a realistic representation from a numerical framework. In the case of droplets, however, temperature has only a limited influence due to the strongly non-linear character of these structures and the strong anisotropies required to support them. However, we emphasize that a resonant type of the quasi-1D droplet was obtained for a nanowire width of 120 nm and a NC diameter of 50 nm in the absence of temperature. The contour plot of such a mode is shown in Fig. C.3(a) where a clear similitude with the quasi-1D droplet in Fig. 6.3(a) is observed. By including a random thermal field [19] equivalent to 300 K, the expected edge mode is observed [Fig. C.3(b)]. We argue that roughness along the nanowire edge would also nucleate an edge

mode. Consequently, only the modes discussed in chapter 6 are expected to be experimentally observable.

C.4 Half-droplet solution

The edge mode is considered to be half a 2D droplet, based on previous studies on conservative three-dimensional surface droplets [10]. Here, we show such a comparison based on the edge mode shown in Fig. 6.2(c) for a nanowire of thickness 140 nm and a NC of diameter 50 nm. The magnetic boundary of such edge mode is approximately a semicircle of diameter 172 nm. Consequently, we perform a simulation of a 2D droplet with diameter 172 nm and a simulation area of 1000×1000 nm. A first sign of agreement is found between the oscillation frequency of the 2D droplet $\sim$ 12.24 GHz and the oscillation frequency of the edge mode 12.47 GHz. Additionally, contour plots of the m_y component are shown in Fig. C.4, where the upper panel is the nanowire of thickness 140 nm while the lower panel shows half of the simulated 2D droplet. Clearly, both panels complement each other, confirming the half droplet picture of Ref. [10]. Note however, that due to the frequency difference and the fact that we simulate a perturbed droplet, the magnetic boundary exhibits phase slips that are not expected from the conservative droplet perspective.

Bibliography

[1] Johan Åkerman, *Toward a universal memory*, Science **308** (2005), no. 5721, 508–510.

[2] R. Adler, *A study of locking phenomena in oscillators*, Proceedings of the IRE **34** (1946), no. 6, 351 – 357.

[3] M. N. Baibich, J. M. Broto, A. Fert, F. Nguyen Van Dau, F. Petroff, P. Etienne, G. Creuzet, A. Friederich, and J. Chazelas, *Giant magnetoresistance of (001)fe/(001)cr magnetic superlattices*, Phys. Rev. Lett. **61** (1988), no. 21, 2472–2475.

[4] M. Balkanski and R.F. Wallis, *Semiconductor physics and applications*, Oxford University Press, 2000.

[5] Gerrit E. W. Bauer, Yaroslav Tserkovnyak, Daniel Huertas-Hernando, and Arne Brataas, *Universal angular magnetoresistance and spin torque in ferromagnetic/normal metal hybrids*, Phys. Rev. B **67** (2003), 094421.

[6] L. Berger, *Emission of spin waves by a magnetic multilayer traversed by a current*, Phys. Rev. B **54** (1996), no. 13, 9353–9358.

[7] S. Beri, L. Gelens, M. Mestre, G. Van der Sande, G. Verschaffelt, A. Scirè, G. Mezosi, M. Sorel, and J. Danckaert, *Topological insight into the non-arrhenius mode hopping of semiconductor ring lasers*, Phys. Rev. Lett. **101** (2008), 093903.

[8] D. V. Berkov and N. L. Gorn, *Micromagnetic simulations of the magnetization precession induced by a spin-polarized current in a point-contact geometry (invited)*, Journal of Applied Physics **99** (2006), no. 8, –.

[9] D.V. Berkov and J. Miltat, *Spin-torque driven magnetization dynamics: Micromagnetic modeling*, Journal of Magnetism and Magnetic Materials **320** (2008), no. 7, 1238 – 1259.

[10] Yu.I. Bespyatykh, I.E. Dikshtein, and S.A. Nikitov, *3d surface precession solitons (surface magnetic drops) in uniaxial magnets*, Physics Letters A **184** (1994), no. 2, 198 – 203.

[11] Stefano Bonetti and Johan Åkerman, *Nano-contact spin-torque oscillators as magnonic building blocks*, Magnonics (Sergej O. Demokritov and Andrei N. Slavin, eds.), Topics in Applied Physics, vol. 125, Springer Berlin Heidelberg, 2013, pp. 177–187 (English).

[12] Stefano Bonetti, Vito Puliafito, Giancarlo Consolo, Vasyl S. Tiberkevich, Andrei N. Slavin, and Johan Åkerman, *Power and linewidth of propagating and localized modes in nanocontact spin-torque oscillators*, Phys. Rev. B **85** (2012), 174427.

[13] Stefano Bonetti, Vasil Tiberkevich, Giancarlo Consolo, Giovanni Finocchio, Pranaba Muduli, Fred Mancoff, Andrei Slavin, and Johan Åkerman, *Experimental evidence of self-localized and propagating spin wave modes in obliquely magnetized current-driven nanocontacts*, Phys. Rev. Lett. **105** (2010), no. 21, 217204.

[14] R. Bonin, G. Bertotti, C. Serpico, I. D. Mayergoyz, and M. d'Aquino, *Analytical treatment of synchronization of spin-torque oscillators by microwave magnetic fields*, The European Physical Journal B - Condensed Matter and Complex Systems **68** (2009), 221–231, 10.1140/epjb/e2009-00091-9.

[15] L. D. Bookman and M. A. Hoefer, *Analytical theory of modulated magnetic solitons*, Phys. Rev. B **88** (2013), 184401.

[16] Simone Borlenghi, Valentin Rychkov, Cyril Petitjean, and Xavier Waintal, *Multiscale approach to spin transport in magnetic multilayers*, Phys. Rev. B **84** (2011), 035412.

[17] O. Boulle, G. Malinowski, and M. Kläui, *Current-induced domain wall motion in nanoscale ferromagnetic elements*, Materials Science and Engineering: R: Reports **72** (2011), no. 9, 159 – 187.

[18] Hans-Benjamin Braun, *Topological effects in nanomagnetism: from superparamagnetism to chiral quantum solitons*, Advances in Physics **61** (2012), no. 1, 1–116.

[19] William Fuller Brown, *Thermal fluctuations of a single-domain particle*, Phys. Rev. **130** (1963), no. 5, 1677–1686.

[20] P. Bruno and J. P. Renard, *Magnetic surface anisotropy of transition metal ultrathin films*, Applied Physics A: Materials Science & Processing **49** (1989), 499–506, 10.1007/BF00617016.

[21] M. Büttiker, Y. Imry, R. Landauer, and S. Pinhas, *Generalized many-channel conductance formula with application to small rings*, Phys. Rev. B **31** (1985), 6207–6215.

[22] A.O. Caldeira and A.J. Leggett, *Path integral approach to quantum brownian motion*, Physica A: Statistical Mechanics and its Applications **121** (1983), no. 3, 587 – 616.

[23] P. F. Carcia, A. D. Meinhaldt, and A. Suna, *Perpendicular magnetic anisotropy in pd/co thin film layered structures*, Applied Physics Letters **47** (1985), no. 2, 178–180.

[24] A.B. Carlson, P.B. Crilly, and J.C. Rutledge, *Communication systems: an introduction to signals and noise in electrical communication*, McGraw-Hill series in electrical and computer engineering, McGraw-Hill, 2002.

[25] Claude Chappert, Albert Fert, and Frédéric Nguyen Van Dau, *The emergence of spin electronics in data storage*, Nature Materials **6** (2007), no. 11, 813–823.

[26] Chol-Ung Choe, Thomas Dahms, Philipp Hövel, and Eckehard Schöll, *Controlling synchrony by delay coupling in networks: From in-phase to splay and cluster states*, Phys. Rev. E **81** (2010), no. 2, 025205.

[27] J.M.D Coey, *Magnetism and magnetic materials*, Cambridge University Press, 2010.

[28] G. Consolo, B. Azzerboni, G. Finocchio, L. Lopez-Diaz, and L. Torres, *Influence of the oersted field in the dynamics of spin-transfer microwave oscillators*, Journal of Applied Physics **101** (2007), no. 9, 09C108.

[29] G. Consolo, L. Lopez-Diaz, L. Torres, and B. Azzerboni, *Boundary conditions for spin-wave absorption based on different site-dependent damping functions*, Magnetics, IEEE Transactions on **43** (2007), no. 6, 2974 –2976.

[30] G. Consolo, V. Puliafito, G. Finocchio, L. Lopez-Diaz, R. Zivieri, L. Giovannini, F. Nizzoli, G. Valenti, and B. Azzerboni, *Combined frequency-amplitude nonlinear modulation: Theory and applications*, Magnetics, IEEE Transactions on **46** (2010), no. 9, 3629 –3634.

[31] Giancarlo Consolo, Bruno Azzerboni, Grant Gerhart, Gennady A. Melkov, Vasil Tiberkevich, and Andrei N. Slavin, *Excitation of self-localized spin-wave bullets by spin-polarized current in in-plane magnetized magnetic nanocontacts: A micromagnetic study*, Phys. Rev. B **76** (2007), no. 14, 144410.

[32] G. H. O. Daalderop, P. J. Kelly, and F. J. A. den Broeder, *Prediction and confirmation of perpendicular magnetic anisotropy in co/ni multilayers*, Phys. Rev. Lett. **68** (1992), no. 5, 682–685.

[33] M. d'Aquino, C. Serpico, R. Bonin, G. Bertotti, and I. D. Mayergoyz, *Micromagnetic analysis of injection locking in spin-transfer nano-oscillators*, Phys. Rev. B **82** (2010), no. 6, 064415.

[34] M. d'Aquino, C. Serpico, R. Bonin, G. Bertotti, and I.D. Mayergoyz, *Analysis of synchronized regimes for injection-locked spin-transfer nano-oscillators*, Physica B: Condensed Matter (2011), no. 0, –.

[35] M. d'Aquino, C. Serpico, G. Coppola, I. D. Mayergoyz, and G. Bertotti, *Midpoint numerical technique for stochastic landau-lifshitz-gilbert dynamics*, Journal of Applied Physics **99** (2006), no. 8, 08B905.

[36] John Davies, *The physics of low dimensional semiconductors*, Cambridge University Press, 2005.

[37] Alina M Deac, Akio Fukushima, Hitoshi Kubota, Hiroki Maehara, Yoshishige Suzuki, Shinji Yuasa, Yoshinori Nagamine, Koji Tsunekawa, David D Djayaprawira, and Naoki Watanabe, *Bias-driven high-power microwave emission from mgo-based tunnel magnetoresistance devices*, Nature Physics **4** (2008), no. 10, 803–809.

[38] V.E. Demidov, H. Ulrichs, S.V. Gurevich, S.O. Demokritov, V.S. Tiberkevich, A N. Slavin, A. Zholud, and S. Urazhdin, *Synchronization of spin hall nano-oscillators to external microwave signals*, Nature Communications **5** (2013), 3179.

[39] Vladislav Demidov, Sergei Urazhdin, Henning Ulrichs, Vasyl Tiberkevich, Andrei Slavin, Dietmar Baither, Guido Schmitz, and Sergej Demokritov, *Magnetic nano-oscillator driven by pure spin current*, Nature Materials **11** (2012), 1028–1031.

[40] Vladislav E Demidov, Sergei Urazhdin, and Sergej O Demokritov, *Direct observation and mapping of spin waves emitted by spin-torque nano-oscillators.*, Nature Materials **9** (2010), no. 12, 984–988.

[41] G Van der Sande, L Gelens, P Tassin, A Scirè, and J Danckaert, *Two-dimensional phase-space analysis and bifurcation study of the dynamical behaviour of a semiconductor ring laser*, Journal of Physics B: Atomic, Molecular and Optical Physics **41** (2008), no. 9, 095402.

[42] T. Devolder, Joo-Von Kim, M. Manfrini, W. van Roy, L. Lagae, and C. Chappert, *Vortex nucleation in spin-torque nanocontact oscillators*, Applied Physics Letters **97** (2010), no. 7, 072512.

[43] Randy K. Dumas, E. Iacocca, S. Bonetti, S. R. Sani, S. M. Mohseni, A. Eklund, J. Persson, O. Heinonen, and Johan Åkerman, *Spin-wave-mode coexistence on the nanoscale: A consequence of the oersted-field-induced asymmetric energy landscape*, Phys. Rev. Lett. **110** (2013), 257202.

[44] A. Dussaux, A. V. Khvalkovskiy, J. Grollier, V. Cros, A. Fukushima, M. Konoto, H. Kubota, K. Yakushiji, S. Yuasa, K. Ando, and A. Fert, *Phase locking of vortex based spin transfer oscillators to a microwave current*, Applied Physics Letters **98** (2011), no. 13, 132506.

[45] I. Dzyaloshinsky, *A thermodynamic theory of "weak" ferromagnetism of antiferromagnetics*, Journal of Physics and Chemistry of Solids **4** (1958), no. 4, 241 – 255.

[46] A. Fert, V. Cros, and J. Sampaio, *Skyrmions on the track*, Nature Nanotechnology **8** (2013), 152 – 156.

[47] Leslie L. Foldy and Siegfried A. Wouthuysen, *On the dirac theory of spin 1/2 particles and its non-relativistic limit*, Phys. Rev. **78** (1950), 29–36.

[48] B. Georges, J. Grollier, V. Cros, and A. Fert, *Impact of the electrical connection of spin transfer nano-oscillators on their synchronization: an analytical study*, Applied Physics Letters **92** (2008), no. 23, 232504.

[49] B. Georges, J. Grollier, M. Darques, V. Cros, C. Deranlot, B. Marcilhac, G. Faini, and A. Fert, *Coupling efficiency for phase locking of a spin transfer nano-oscillator to a microwave current*, Phys. Rev. Lett. **101** (2008), no. 1, 017201.

[50] G. Gerhart, E. Bankowski, G. A. Melkov, V. S. Tiberkevich, and A. N. Slavin, *Angular dependence of the microwave-generation threshold in a nanoscale spin-torque oscillator*, Phys. Rev. B **76** (2007), no. 2, 024437.

[51] Mathias Getzlaff, *Fundamental of magnetism*, Springer, 2008.

[52] T.L. Gilbert, *A phenomenological theory of damping in ferromagnetic materials*, Magnetics, IEEE Transactions on **40** (2004), no. 6, 3443 – 3449.

[53] D. Golomb, D. Hansel, B. Shraiman, and H. Sompolinsky, *Clustering in globally coupled phase oscillators*, Phys. Rev. A **45** (1992), no. 6, 3516–3530.

[54] David Griffiths, *Introduction to quantum mechanics*, Prentice Hall, 1995.

[55] J. Grollier, V. Cros, and A. Fert, *Synchronization of spin-transfer oscillators driven by stimulated microwave currents*, Phys. Rev. B **73** (2006), no. 6, 060409.

[56] P.M. Haney, R.A. Duine, A.S. Núñez, and A.H. MacDonald, *Current-induced torques in magnetic metals: Beyond spin-transfer*, Journal of Magnetism and Magnetic Materials **320** (2008), no. 7, 1300 – 1311.

[57] O.G. Heinonen, P.K. Muduli, E. Iacocca, and J. Åkerman, *Decoherence, mode hopping, and mode coupling in spin torque oscillators*, Magnetics, IEEE Transactions on **49** (2013), no. 7, 4398–4404.

[58] M. A. Hoefer, T. J. Silva, and Mark W. Keller, *Theory for a dissipative droplet soliton excited by a spin torque nanocontact*, Phys. Rev. B **82** (2010), 054432.

[59] M. A. Hoefer, M. Sommacal, and T. J. Silva, *Propagation and control of nanoscale magnetic-droplet solitons*, Phys. Rev. B **85** (2012), 214433.

[60] Alex Hubert and Rudolf Schäfer, *Magnetic domains: the analysis of magnetic microstructures*, Springer, 2009.

[61] E. Iacocca, *Mutual phase locking of spin torque oscillators*, Master's thesis, Royal Institute of Technology, 2010.

[62] M Julliere, *Tunneling between ferromagnetic films*, Physics Letters A **54** (1975), no. 3, 225–226.

[63] Shehzaad Kaka, Matthew R Pufall, William H Rippard, Thomas J Silva, Stephen E Russek, and Jordan A Katine, *Mutual phase-locking of microwave spin torque nano-oscillators.*, Nature **437** (2005), no. 7057, 389–392.

[64] B.A. Kalinikos and A.N. Slavin, *Theory of dipole-exchange spin wave spectrum for ferromagnetic films with mixed exchange boundary conditions*, Journal of Physics C: Solid State Physics **19** (1986), no. 35, 7013.

[65] V. Kambersky and C. E. Patton, *Spin-wave relaxation and phenomenological damping in ferromagnetic resonance*, Phys. Rev. B **11** (1975), no. 7, 2668–2672.

[66] Mark W. Keller, M. R. Pufall, W. H. Rippard, and T. J. Silva, *Non-white frequency noise in spin torque oscillators and its effect on spectral linewidth*, Phys. Rev. B **82** (2010), no. 5, 054416.

[67] Joo-Von Kim, *Stochastic theory of spin-transfer oscillator linewidths*, Phys. Rev. B **73** (2006), no. 17, 174412.

[68] Joo-Von Kim, Q. Mistral, C. Chappert, V. S. Tiberkevich, and A. N. Slavin, *Line shape distortion in a nonlinear auto-oscillator near generation threshold: Application to spin-torque nano-oscillators*, Phys. Rev. Lett. **100** (2008), no. 16, 167201.

[69] Joo-Von Kim, Vasil Tiberkevich, and Andrei N. Slavin, *Generation linewidth of an auto-oscillator with a nonlinear frequency shift: Spin-torque nano-oscillator*, Phys. Rev. Lett. **100** (2008), no. 1, 017207.

[70] S. I. Kiselev, J. C. Sankey, I. N. Krivorotov, N. C. Emley, M. Rinkoski, C. Perez, R. A. Buhrman, and D. C. Ralph, *Current-induced nanomagnet dynamics for magnetic fields perpendicular to the sample plane*, Phys. Rev. Lett. **93** (2004), 036601.

[71] S I Kiselev, J C Sankey, I N Krivorotov, N C Emley, R J Schoelkopf, R A Buhrman, and D C Ralph, *Microwave oscillations of a nanomagnet driven by a spin-polarized current.*, Nature **425** (2003), no. 6956, 380–383.

[72] A. Kosevich, V. Gann, A. Zhukov, and V. Voronov, *Magnetic soliton motion in a nonuniform magnetic field*, Journal of Experimental and Theoretical Physics **87** (1998), 401–407, 10.1134/1.558674.

[73] A.M. Kosevich, B.A. Ivanov, and A.S. Kovalev, *Magnetic solitons*, Physics Reports **194** (1990), no. 3–4, 117 – 238.

[74] I. N. Krivorotov, N. C. Emley, R. A. Buhrman, and D. C. Ralph, *Time-domain studies of very-large-angle magnetization dynamics excited by spin transfer torques*, Phys. Rev. B **77** (2008), 054440.

[75] R. Lehndorff, D. E. Bürgler, C. M. Schneider, and Z. Celinski, *Injection locking of the gyrotropic vortex motion in a nanopillar*, Applied Physics Letters **97** (2010), no. 14, –.

[76] R. H. Liu, W. L. Lim, and S. Urazhdin, *Spectral characteristics of the microwave emission by the spin hall nano-oscillator*, Phys. Rev. Lett. **110** (2013), 147601.

[77] Yuyan Liu, Jieli Lin, G Huang, Y Guo, and C Duan, *Simple empirical analytical approximation to the voigt profile*, Journal of the Optical Society of America B **18** (2001), no. 5, 666.

[78] N. Locatelli, V. Cros, and J Grollier, *Spin-torque building blocks*, Nature Materials **13** (2013), 11–20.

[79] M. Madami, S. Bonetti, G. Consolo, S. Tacchi, G. Carlotti, G. Gubbiotti, F. B. Mancoff, M. A. Yar, and J. Åkerman, *Direct observation of a propagating spin wave induced by spin-transfer torque*, Nature Nanotechnology **6** (2011), 635–638.

[80] M.D. Maiden, L. Bookman, and A. Hoefer, *Scattering of nontopological magnetic solitons*, **arXiv:1311.0349** (2013).

[81] F B Mancoff, N D Rizzo, B N Engel, and S Tehrani, *Phase-locking in double-point-contact spin-transfer devices.*, Nature **437** (2005), no. 7057, 393–395.

[82] G N Milshtein, *A method of second-order accuracy integration of stochastic differential equations*, Theory Prob Appl **23** (1978), 396–401.

[83] S. M. Mohseni, S. R. Sani, J. Persson, T. N. Anh Nguyen, S. Chung, Ye. Pogoryelov, and Johan Åkerman, *High frequency operation of a spin-torque oscillator at low field*, Physica Status Solidi RRL **5** (2011), no. 12, 432 – 434.

[84] S. M. Mohseni, S. R. Sani, J. Persson, T. N. Anh Nguyen, S. Chung, Ye. Pogoryelov, P. K. Muduli, E. Iacocca, A. Eklund, R. K. Dumas, S. Bonetti, A. Deac, M. A. Hoefer, and J. Åkerman, *Spin torque–generated magnetic droplet solitons*, Science **339** (2013), no. 6125, 1295–1298.

[85] Tôru Moriya, *Anisotropic superexchange interaction and weak ferromagnetism*, Phys. Rev. **120** (1960), 91–98.

[86] C. Moutafis, S. Komineas, and J. A. C. Bland, *Dynamics and switching processes for magnetic bubbles in nanoelements*, Phys. Rev. B **79** (2009), 224429.

[87] C. Moutafis, S. Komineas, C. A. F. Vaz, J. A. C. Bland, T. Shima, T. Seki, and K. Takanashi, *Magnetic bubbles in fept nanodots with perpendicular anisotropy*, Phys. Rev. B **76** (2007), 104426.

[88] P. K. Muduli, O. G. Heinonen, and Johan Åkerman, *Decoherence and mode hopping in a magnetic tunnel junction based spin torque oscillator*, Phys. Rev. Lett. **108** (2012), 207203.

[89] ———, *Temperature dependence of linewidth in nanocontact based spin torque oscillators: Effect of multiple oscillatory modes*, Phys. Rev. B **86** (2012), 174408.

[90] P. K. Muduli, Ye. Pogoryelov, S. Bonetti, G. Consolo, Fred Mancoff, and Johan Åkerman, *Nonlinear frequency and amplitude modulation of a nanocontact-based spin-torque oscillator*, Phys. Rev. B **81** (2010), no. 14, 140408.

[91] S. Mühlbauer, B. Binz, F. Jonietz, C. Pfleiderer, A. Rosch, A. Neubauer, R. Georgii, and P. Böni, *Skyrmion lattice in a chiral magnet*, Science **323** (2009), no. 5916, 915–919.

[92] J. A. Osborn, *Demagnetizing factors of the general ellipsoid*, Phys. Rev. **67** (1945), no. 11-12, 351–357.

[93] Edward Ott, *Chaos in dynamical systems*, Cambridge University Press, 1994.

[94] J. Persson, Yan Zhou, and Johan Åkerman, *Phase-locked spin torque oscillators: Impact of device variability and time delay*, Journal of Applied Physics **101** (2007), no. 9, 09A503.

[95] S. Petit-Watelot, R. M. Otxoa, and M. Manfrini, *Electrical properties of magnetic nanocontact devices computed using finite-element simulations*, Applied Physics Letters **100** (2012), no. 8, 083507.

[96] Cyril Petitjean, David Luc, and Xavier Waintal, *Unified drift-diffusion theory for transverse spin currents in spin valves, domain walls, and other textured magnets*, Phys. Rev. Lett. **109** (2012), 117204.

[97] Arkady Pikovsky, Michael Rosenblum, and Jürgen Kurths, *Synchronization: A universal concept in nonlinear sciences*, Cambridge University Press, 2001.

[98] Ye. Pogoryelov, P. K. Muduli, S. Bonetti, E. Iacocca, Fred Mancoff, and Johan Åkerman, *Frequency modulation of spin torque oscillator pairs*, Applied Physics Letters **98** (2011), no. 19, 192501.

[99] David Pozar, *Microwave engineering*, 4th ed., Wiley, 2012.

[100] V.S Pribiag, I N Krivorotov, G. D. Fuchs, P M Braganca, O. Ozatay, J C Sankey, D C Ralph, and R A Buhrman, *Magnetic vortex oscillator driven by d.c. spin-polarized current*, Nature Physics **3** (2007), 489 – 503.

[101] M. R. Pufall, W. H. Rippard, S. Kaka, T. J. Silva, and S. E. Russek, *Frequency modulation of spin-transfer oscillators*, Applied Physics Letters **86** (2005), no. 8, 082506.

[102] M. R. Pufall, W. H. Rippard, S. E. Russek, S. Kaka, and J. A. Katine, *Electrical measurement of spin-wave interactions of proximate spin transfer nanooscillators*, Phys. Rev. Lett. **97** (2006), no. 8, 087206.

[103] M. Quinsat, J. F. Sierra, I. Firastrau, V. Tiberkevich, A. Slavin, D. Gusakova, L. D. Buda-Prejbeanu, M. Zarudniev, J.-P. Michel, U. Ebels, B. Dieny, M.-C. Cyrille, J. A. Katine, D. Mauri, and A. Zeltser, *Injection locking of tunnel junction oscillators to a microwave current*, Applied Physics Letters **98** (2011), no. 18, 182503.

[104] D.C. Ralph and M.D. Stiles, *Spin transfer torques*, Journal of Magnetism and Magnetic Materials **320** (2008), no. 7, 1190 – 1216.

[105] Behzad Razavi, *Mutual injection pulling between oscillators*, IEEE Custom Integrated Circuits Conference 2006 **90095** (2006), no. Cicc, 675–678.

[106] S. M. Rezende, F. M. de Aguiar, and A. Azevedo, *Spin-wave theory for the dynamics induced by direct currents in magnetic multilayers*, Phys. Rev. Lett. **94** (2005), 037202.

[107] W. H. Rippard, M. R. Pufall, S. Kaka, T. J. Silva, S. E. Russek, and J. A. Katine, *Injection locking and phase control of spin transfer nano-oscillators*, Phys. Rev. Lett. **95** (2005), no. 6, 067203.

[108] William Rippard, Matthew Pufall, and Anthony Kos, *Time required to injection-lock spin torque nanoscale oscillators*, Applied Physics Letters **103** (2013), no. 18, –.

[109] H. Risken, *The fooker-planck equation: methods of solution and applications*, 3rd ed., Springer, 1996.

[110] Niklas Romming, Christian Hanneken, Matthias Menzel, Jessica E. Bickel, Boris Wolter, Kirsten von Bergmann, André Kubetzka, and Roland Wiesendanger, *Writing and deleting single magnetic skyrmions*, Science **341** (2013), no. 6146, 636–639.

[111] J. Sampaio, V. Cros, S. Rohart, A. Thiaville, and A. Fert, *Nucleation, stability and current-induced motion of isolated magnetic skyrmions in nanostructures*, Nature Nanotechnology **8** (2013), 839–844.

[112] S. Sani, J. Persson, S.M. Mohseni, Ye. Pogoryelov, P K Muduli, A. Eklund, G. Malm, M. Käll, A. Dmitriev, and J. Åkerman, *Mutually synchronized bottom-up multi-nanocontact spin-torque oscillators*, Nature Co **4** (2013), 2731.

[113] J. C. Sankey, I. N. Krivorotov, S. I. Kiselev, P. M. Braganca, N. C. Emley, R. A. Buhrman, and D. C. Ralph, *Mechanisms limiting the coherence time of spontaneous magnetic oscillations driven by dc spin-polarized currents*, Phys. Rev. B **72** (2005), 224427.

[114] Adel Sedra and Kenneth Smith, *Microelectronic circuits*, Oxford University Press, 2004.

[115] C Serpico, R Bonin, G Bertotti, M d'Aquino, and I D Mayergoyz, *Theory of injection locking for large magnetization motion in spin-transfer nano-oscillators*, IEEE Transactions on Magnetics **45** (2009), no. 10, 3441–3444.

[116] T.J. Silva and M.W. Keller, *Theory of thermally induced phase noise in spin torque oscillators for a high-symmetry case*, Magnetics, IEEE Transactions on **46** (2010), no. 9, 3555 –3573.

[117] A. Slavin and V. Tiberkevich, *Excitation of spin waves by spin-polarized current in magnetic nano-structures*, Magnetics, IEEE Transactions on **44** (2008), no. 7, 1916 –1927.

[118] ———, *Nonlinear auto-oscillator theory of microwave generation by spin-polarized current*, Magnetics, IEEE Transactions on **45** (2009), no. 4, 1875 –1918.

[119] A N Slavin and Pavel Kabos, *Approximate theory of microwave generation in a current-driven magnetic nanocontact magnetized in an arbitrary direction*, IEEE Transactions on Magnetics **41** (2005), no. 4, 1264–1273.

[120] A. N. Slavin and V. S. Tiberkevich, *Theory of mutual phase locking of spin-torque nanosized oscillators*, Phys. Rev. B **74** (2006), no. 10, 104401.

[121] Andrei Slavin and Vasil Tiberkevich, *Spin wave mode excited by spin-polarized current in a magnetic nanocontact is a standing self-localized wave bullet*, Phys. Rev. Lett. **95** (2005), no. 23, 237201.

[122] J. C. Slonczewski, *Current-driven excitation of magnetic multilayers*, Journal of Magnetism and Magnetic Materials **159** (1996), no. 1-2, L1 – L7.

[123] ———, *Excitation of spin waves by an electric current*, Journal of Magnetism and Magnetic Materials **195** (1999), no. 2, 261 – 268.

[124] Daniel Stancil and Anil Prabhakar, *Spin waves: Theory and applications*, Springer, 2009.

[125] M. D. Stiles and A. Zangwill, *Noncollinear spin transfer in co/cu/co multilayers (invited)*, Journal of Applied Physics **91** (2002), no. 10, 6812–6817.

[126] Edmund C. Stoner, *Collective electron ferromagnetism*, Proceedings of the Royal Society of London. Series A. Mathematical and Physical Sciences **165** (1938), no. 922, 372–414.

[127] Joachim Stör and Hans Christoph Siegmann, *Magnetism: from fundamentals to nanoscale dynamics*, Springer, 2006.

[128] H. Suhl, *Theory of the magnetic damping constant*, Magnetics, IEEE Transactions on **34** (1998), no. 4, 1834 –1838.

[129] V. S. Tiberkevich, A. N. Slavin, and Joo-Von Kim, *Temperature dependence of nonlinear auto-oscillator linewidths: Application to spin-torque nano-oscillators*, Phys. Rev. B **78** (2008), no. 9, 092401.

[130] Vasil Tiberkevich, Andrei Slavin, Elena Bankowski, and Grant Gerhart, *Phase-locking and frustration in an array of nonlinear spin-torque nano-oscillators*, Applied Physics Letters **95** (2009), no. 26, 262505.

[131] H. Ulrichs, V. E. Demidov, and S. O. Demokritov, *Micromagnetic study of auto-oscillation modes in spin-hall nano-oscillators*, Applied Physics Letters **104** (2014), no. 4, –.

[132] Sergei Urazhdin, Phillip Tabor, Vasil Tiberkevich, and Andrei Slavin, *Fractional synchronization of spin-torque nano-oscillators*, Phys. Rev. Lett. **105** (2010), no. 10, 104101.

[133] T. Valet and A. Fert, *Theory of the perpendicular magnetoresistance in magnetic multilayers*, Phys. Rev. B **48** (1993), no. 10, 7099–7113.

[134] N.G. Van Kampen, *Stochastic processes in physics and chemistry*, 3rd ed., Elsevier, 2007.

[135] P. C. van Son, H. van Kempen, and P. Wyder, *Boundary resistance of the ferromagnetic-nonferromagnetic metal interface*, Phys. Rev. Lett. **58** (1987), no. 21, 2271–2273.

[136] A. Vansteenkiste and B. Van de Wiele, *Mumax: A new high-performance micromagnetic simulation tool*, Journal of Magnetism and Magnetic Materials **323** (2011), no. 21, 2585 – 2591.

[137] Xavier Waintal, Edward B. Myers, Piet W. Brouwer, and D. C. Ralph, *Role of spin-dependent interface scattering in generating current-induced torques in magnetic multilayers*, Phys. Rev. B **62** (2000), 12317–12327.

[138] Robert White, *Quantum theory of magnetism*, Springer, 2007.

[139] Jiang Xiao, A. Zangwill, and M. D. Stiles, *Macrospin models of spin transfer dynamics*, Phys. Rev. B **72** (2005), no. 1, 014446.

[140] X.Z. Yu, N. Kanazawa, Y. Onose, K. Kimoto, W.Z. Zhang, S. Ishiwata, Y. Matsui, and Y. Tokura, *Near room-temperature formation of skyrmion crystal in thin-films of the helimagnet fege*, Nature Materials **10** (2011), 106–109.

[141] X.Z. Yu, Y. Onose, N. Kanazawa, J.H. Park, J.H. Han, Y. Matsui, N. Nagaosa, and Y. Tokura, *Real-space observation of a two-dimensional skyrmion crystal*, Nature **465** (2010), 901 – 904.

[142] S. Yuasa, T. Nagahama, A. Fukushima, Y. Suzuki, and K. Ando, *Giant room-temperature magnetoresistance in single-crystal fe/mgo/fe magnetic tunnel junctions*, Nature Materials **3** (2004), 868 – 871.

[143] Zhongming Zeng, Kwun Hung Cheung, H. W. Jiang, I. N. Krivorotov, J. A. Katine, V. Tiberkevich, and A. Slavin, *Evolution of spin-wave modes in magnetic tunnel junction nanopillars*, Phys. Rev. B **82** (2010), 100410.

[144] Y. Zhou, E. Iacocca, R.K. Dumas, F.C. Zhang, and J. Åkerman, *Magnetic droplet skyrmions*, **arXiv:1404.3281** (2014).

[145] Yan Zhou, *Spin momentum transfer effects for spintronic device applications*, Ph.D. thesis, Royal Institute of Technology, 2009.

[146] Yan Zhou, Johan Persson, and Johan Åkerman, *Intrinsic phase shift between a spin torque oscillator and an alternating current*, Journal of Applied Physics **101** (2007), no. 9, 09A510.

[147] Yan Zhou, Vasil Tiberkevich, Giancarlo Consolo, Ezio Iacocca, Bruno Azzerboni, Andrei Slavin, and Johan Åkerman, *Oscillatory transient regime in the forced dynamics of a nonlinear auto oscillator*, Phys. Rev. B **82** (2010), no. 1, 012408.